Alma Mater Studiorum – Università di Bologna

Department of Electric, Electronic and Information Engineering "Guglielmo Marconi" (DEI)

DOTTORATO DI RICERCA IN

Ingegneria Biomedica, Elettrica e dei Sistemi (IBES)

Ciclo 30

Settore Concorsuale: 09/G1-AUTOMATICA

Settore Scientifico Disciplinare:ING-INF/04-AUTOMATICA

Doubly-Fed Induction Machines: Model, Control and Applications

Presentata da:
Ahmad Hashemi

Coordinatore Dottorato

Prof. Daniele Vigo

Supervisore

Prof. Andrea Tilli

Esame finale anno 2018

Abstract

In our modern world, renewable energy resources far outweigh the classic fossil fuels or nuclear power in several terms of benefits, i.e. environmentally friendly, security, economically, and availability factors. With the current growing rate, it is estimated that they soon overtake fossil fuels in the energy market, as well. Wind Energy Conversion Systems are the fastest grown units among renewables within the recent years. Due to large penetration of wind units in the nowadays power systems, some specific regulations have been issued through modern national grid codes to manage their technical commitments. Low Voltage Ride Through (LVRT), as one of the most important requirements, asks wind units to ride through some predefined grid low voltage conditions in terms of amplitude reduction and time duration, mainly caused by different types of balanced and/or unbalanced power network faults.

Doubly-Fed Induction Generators (DFIGs) as the most popular machines among the current driven wind turbines, are electrically connected to the grid through a three-phase winding placed at the stator, while rotor is electromagnetically connected to the stator. Hence, a sudden reduction of the voltage profile, will trigger large current/flux oscillations in the machine, may hit the physical limits and as a consequence, violate the grid codes.

The main topic of this thesis is modeling and control of a DFIG-based wind turbine system in order to substantiate the LVRT requirements without imposing any additional hardware to the installed components. In order to achieve this objective, system/control theory tools are applied to investigate the effects of grid faults on DFIG dynamics, and design proper control-based countermeasures. More specifically, taking advantage from analyzing the internal dynamics of DFIG, various feedforward-feedback controllers have been designed to deal with line faults having increasing complexity. A crucial role in such approach is played by a suitable state reference trajectory design, based on the feature of the DFIG internal dynamics. Such kind of method has been applied to deal with the mechanical dynamics, as well. Numerical realistic simulations validate the benefits of the proposed controller, in crucially improving the machine response under severe grid faults.

Acknowledgements

When I found my name among the last Ph.D. admission list issued in October 2014, everyone in my family got happy. But, she failed to hide her anxiety. A bitter smile appeared on her face while presenting lovely congratulations. She knew many things may happen within these three years! "I wish this would be your defense congratulations", she said hugging me tightly at the airport in September 2015. It was the last time I blessed the maternal embrace, out of cancer bed... Those three years are now finished, and your aspiration is close to come true. I would offer this work with all my sincerest prayers to your soul. I am sure you will receive it...

I would like to express sincere gratitudes to my father. He pledged himself to kept patience supporting me going ahead. Also, a special thanks goes to my siblings. Within this period, they compensated for me in numerous demanding seconds.

My supervisor, Prof. Andrea Tilli, deserves too many appreciating words. I could not imagine having a better advisor and mentor for my Ph.D study. Along with his precious guidance and motivation in all the time of research, he presented one invaluable lecture to me; the actual meaning of humanity and morality. I will proud to be his student for the rest of my life.

Besides my advisor, I also owe sincere gratitudes to Dr. Christian Conficoni. In addition to his friendship opportunity, I took advantage from his admirable knowledge and experience, generously offered by him in each second of this period.

My appreciation goes to prof. Lina Bertling who hosted me for six months at KTH Loyal Institute of Technology, Stockholm, giving me the possibility to work at timely interesting topics, along with is research team, formed by skilled and kind guys I'd like to thank too.

Many sincere thanks to L.A.R. close friends for making the period more joyful and profitable. Specifically, Dr. Matteo Conficoni and Dr. Mohssen Hosseini helped me a lot during these three years I would like to thank them.

At the end, it would be a great ingratitude if I would not appreciate Italy and Italians in general. You hosted me generously, and taught me a lot of graceful things. Hope to be able to repay a part of this favor, in the future.

Contents

Introduction

Global installed renewable generation capacity has been consistently increasing in the last years, reaching a total of 1,985 GW at the end of 2015 [1]. Among renewables, wind power has been the fastest growing energy source, exponentially going from 6.1 GW in 1996 to 282.6 GW in 2012, and it is predicted to reach 760 GW by 2020 with the current trend [2].
Doubly-Fed Induction Machine (DFIM) is a widely used technology for modern Wind Energy Conversion Systems (WECS), thanks to high efficiency, improved power quality, and low cost properties [3]. Indeed, more than 50% of the currently installed WECSs use this class of electrical machines [4]. In this application framework, it is usually referred to as Doubly-Fed Induction Generator, DFIG connected to variable speed, fixed frequency Wind Turbines (WTs). In the typical scheme for power generation systems with DFIG, the stator windings are directly connected to the grid, while the wound-rotor is fed, by means of slip rings, with voltage provided by a controlled power electronic converter (so-called Rotor Side Converter, RSC). The main advantage of this configuration is that RSC has to manage only a fraction of the generator power (around 30%, but depending on slip value), scaling with the slip percentage [5, 6], thus RSC has about one third of the size, cost and losses of a conventional variable-speed drive. Moreover, four quadrant power operation can be achieved [7, 8] also thanks to the controlled boost converter adopted as Grid Side Converter (GSC), whose main task is to keep the DC-link capacitor voltage within a prescribed range, by exchanging undistorted active power with the line.
The DFIG control algorithm plays a crucial role for wind turbines performance enhancement. While standard techniques, defined for any electric drive with an Active Front End, are available for GSC [9], controlling the rotor side via the RSC, requires more sophisticated strategies. In this respect, several control solutions are available, in order to decouple active and reactive power generation control. In the framework of standard vector control [10], different variants have been proposed, depending on the orientation of the considered synchronously-rotating reference frame, and the control algorithm . In [11, 12], torque and reactive power regulations are achieved by high-gain PI controllers designed to steer the rotor currents. In order to define suitable references, Stator Flux Oriented (SFO) reference frame is considered. In

[13], state feedback linearization has been exploited assuming rotor current-fed machine, and an additional first-order dynamics in the control loop. The controller design is performed in the Rotor Flux Oriented (RFO) frame. Recently, in [14], input-output feedback linearization has been applied considering the rotor voltage-fed machine, and exploiting its differential flatness properties.

According to the mentioned high penetration of renewables in the recent years, making WECSs critical sources of nowadays power networks, specific national Grid Codes have been issued, demanding such systems to comply with strict technical qualifications in order to improve safety, reliability, and stability of the power system network [15, 16, 17, 18, 19]. On of the most challenging specifications in this way, regards the Low Voltage Ride Through (LVRT) feature which is the ability of remain connected to the grid under some predefined classes of voltage dips with providing some ancillary services, such as reactive current support. The magnitude and time duration asked by LVRT regulation depends on the dip structure at the Point of Common Coupling (PCC) and the approximate time taken by the system to recover the pre-fault condition. As instances, German E.ON Netz regulations asks for riding through 85% voltage drop lasting for $625ms$, while American FERC accounts for 100% drop for $150ms$ [16],[17].

Voltage dips are are considered as very critical perturbations for DFIG. Indeed, such events, usually due to distant line short-circuits, decrease the amount of the power which can be transmitted to the line, upsetting the generating and delivering energy balance of the wind turbine (there would exist a surplus of the power generated by DFIG with respect to what can be transferred to the grid). Owing to the current limits, the voltage of the DC-link capacitor C is usually affected by this imbalance, and a sudden reduction in the DFIG torque is needed to prevent overvoltage. Furthermore, since the stator windings are directly connected to the three-phase grid and rotor is electromagnetically coupled to the stator, DFIG is extremely sensitive to grid voltage variations. To explain more, each line voltage variation during the grid fault, as a disturbance, triggers high oscillations in fluxes, and currents of the both stator and rotor windings. Usually, this phenomenon also makes standard controllers give large voltage commands on RSC (in particular for asymmetrical dips [20], [21]), hitting the saturation constraints and possibly leading to converter overcurrents. Finally, all of these electrical transients will affect the torque command and the actual torque of the DFIG, this can trigger mechanical dynamics of the generator and its prime mover, as well, if relevant mechanical resonances characterize the driveline.

Therefore, under the fault condition, as a straightforward solution, RSC should be disconnected to prevent the mentioned damages. This is the most frequent approach, currently adopted at WECSs by means of installed crowbar protections,

which short-circuits the rotor winding through some active resistors within the voltage dips. However, crowbar system not only compels extra cost, but it impairs DFIG's controllability hindering LVRT capabilities. In addition, triggering crowbar intervention makes the generator to absorb large reactive power from the grid. This worsens line voltage degradation, instead of supporting the network by reactive component injection as asked in Grid Codes [22].

Many solutions have been suggested in recent literature to cope with such problems. A popular strategy is based on demagnetizing current reference [23], i.e. rotor currents set points are modified during the dip, to oppose the components arising in the stator flux; in [24], [25], and [26], virtual resistor, variable structure and hysteresis current controller are respectively exploited for such purpose. In [27] the rotor current reference is switched onto the stator current measurements, while in [28] the reference switch is performed on the rotor flux linkage, scaling it down when a fault is detected, in order to limit rotor current oscillations. In [29], a nonlinear controller as a combination of a PI and Lyapunov based auxiliary control is proposed to stabilize the DFIG dynamics and improve post-fault behavior, through rotor control voltage. In [30], [31] feedforward transient compensation terms are proposed to be added during the fault in order to reduce the system sensitivity to the line voltage disturbance. In [32] and [33] the focus is mainly put onto the energy surplus problem (by converting the mentioned imbalanced power into the kinetic energy of WT through the speed increase command), and enhancement of the reactive power support, respectively. In [34], a protection hardware for in-grid DFIG based on superconducting fault current limiter (STCL) connected in series with the DFIG rotor winding, is proposed to absorb the extra energy of the stator to prevent the semiconductor devices from overvoltage. During the grid fault, an Energy Storage Device (ESD) is exploited in [35], for DC-link voltage regulation, while GSC connection is reconfigured to be paralleled with RSC, providing an alternative path for the rotor current. During line faults, in [36], rotor current is controlled to track stator current in a certain scale, in order to achieve LVRT capability and comply with the constraint of converter's maximum output voltage.

Despite the large literature, in my opinion, a clear assessment of the problem is still needed. In particular, most of the attention has been paid to deal with the abovementioned power surplus due to the impossibility to transfer significant active power to the grid, when a voltage dip is taking place. In contrast, no clear analysis (at least form a system theory viewpoint) is given for what concerns the effects of voltage dip on the DFIG electromagnetic dynamics and control solutions to cope with. Moreover, to the best of my knowledge, the control-based methods presented in literature can deal only with mild sags, particularly when comes to asymmetrical voltage dips [37]. Therefore, combination with some auxiliary dedicated hardware is commonly

adopted to prevent system tripping under severe faults (see [34], [38], [39] for recent proposals exploiting innovative auxiliary hardware).
In this context, the main contribution of this thesis is to deeply analyze the dip effects on DFIG dynamics. This is the first step which leads to the controller design. A novel control strategy for DFIG (i.e. acting on RSC) is proposed that is capable of achieving full LVRT features, without additional hardware requirements (with respect to what needed for normal operation), not only for three-phase symmetrical faults but even in case of very harsh unbalanced line voltage dips, usually not covered by the control-based solutions presented in literature (neither in simulation tests, to the best of my knowledge).
To this aim, advanced control theory tools are exploited, first for a clear analysis of the line voltage disturbance effects, then to design a suitable mixed feedforward-feedback solution, based on the analysis results and explicitly accounting for the system's constraints. Control objectives for the considered class of systems are typically specified in terms of torque and reactive power at the stator side, which are suitably mapped into the corresponding (stator or rotor) current references.
In this thesis, first, assuming stator/rotor currents as the output variables to be controlled, the corresponding Brunovsky forms [40] of the system dynamics are derived, in order to clearly analyze the zero dynamics, driven by the line voltage and the stator/rotor current references. Then, for each form, the corresponding zero dynamics is particularly studied to design state trajectories suitably, in order to prevent unpleasant oscillatory behavior of the zero dynamics. In this thesis, a mixed feedforward-feedback control solution is proposed. The state reference trajectories obtained by the analytical solutions of zero dynamics are used to generate feedforward compensations and design a state feedback part to effectively push the real variables toward the reference ones. The feedback part, taking advantage of the results in [41] in combination with saturated control techniques, allows to further tame oscillations, while dealing with rotor voltage limits. More specifically, since to obtain full LVRT capability the first task is avoiding overcurrent in RSC, the saturated feedback controller is designed to minimize transients on rotor currents. On the way of dealing with severe balanced and unbalanced voltage dips, the removal of the effects of natural DFIG dynamics in state reference generation, combined with the properties of Sylvester equations, is a key step in the path to achieve robustness to very harsh dips. Another issue in dealing with line faults concerns the detection and reconstruction of the faulty voltage profile. As it will be clarified later, this is crucial to compute proper oscillation-free zero dynamics trajectories (for which line voltage is an input). To this aim, in this thesis, nonlinear state observers are proposed, which outperform standard delayed-signal cancellation, particularly under unbalanced faults. A particular attention is also put to the WT mechanical

oscillations under the faulty conditions, in this thesis. In order to suppress the mechanical vibration in the drive train, a High Bandwidth Feedback (HBF) controller is conventionally adopted, designed based on the pole placement approach utilizing the linearized model of WT. Since the HBF controller should be turned off within the voltage dip, WT speed will consequently arise. After the dip clearance which may take several hundreds of ms, the swelled WT speed should be brought back to the pre-fault steady-state condition in the minimum time and smooth enough trajectory, without violating the generator torque constraints. As another contribution, in this thesis, an optimization problem is formulated and solved in order to substantiate all above mentioned goals. To avoid large computational burden in the online condition, the optimization problem is solved for several reasonable boundary conditions offline and a lookup table and interpolation among the solutions is exploited online to design the suitable trajectory for the WT speed after-dip recovery. At the final chapter of the thesis, as another important contribution, a precise analytical mapping solution from the mentioned original torque and reactive power at the stator side to the corresponding reference rotor currents, is proposed. This mapping solution is also performed during the fault, tracking the decreasing torque profile and the required reactive power/current to support the grid. Simulation results with and without the proposed mapping solution bolds its effectiveness in improving the system performance under voltage dips i.e. the accurate original reference tracking by the system response.

This thesis is structured as follows. In Ch. 1, DFIG model is elaborated starting from three-phase ABC model. After a brief description of two-axes stationary reference frame, finally synchronously rotating reference frame is selected as the most suitable framework for explaining the dynamics of the machine. In this way, state space equations in the Stator Voltage Oriented reference frame is detailed for two different sets of the output state variables. As regards Wind Turbine, similar to other works in the literature [42], [43], [44] a standard two mass model, conventionally exploited for the WECSs studies, is adopted to capture the WT crucial mechanical behavior. Ch. 2 is allocated to broach the details of LVRT capability for DFIG WT system asked by modern grid codes. In this way, first power system short circuits leading to voltage perturbations are categorized and explained in two main sections of balanced and unbalanced dips. Two well-known national grid codes examples for LVRT regulations are mentioned and the corresponding requirements of ride through and reactive power support under the voltage dips are illustrated in the suitable diagrams. After mentioning the negative effects on the system caused by voltage dips, the basic treatment, conventionally applied in the current installed WECSs and it's consequent side effects are explained.

The details of the DFIG control under harsh balanced voltage dips is discussed in

Ch.3. For this purpose, first general objectives and constraints are reported. Then, the Brunovsky (Normal) forms of the system dynamics are generated assuming two different sets of outputs, namely stator and rotor currents. On the way of trajectory planning, corresponding zero dynamics ODE are solved analytically in two ways: exploiting Sylvester equation and integrating by parts. After that, the effect of the line voltage disturbances are analyzed by considering the zero dynamics with respect to the rotor currents and by studying the system behavior, when a standard feedback linearizing controller is imposed, using the rotor currents as outputs. In the following, first, the previously-designed reference trajectory is employed in an open-loop controller. Then, a feedforward-feedback control strategy is proposed relying on modern saturated control techniques to deal with control voltage limits; in addition, an LMI-constrained convex optimization problem is defined to minimize the oscillations under voltage dips. Simulations are provided in all of the previous Sections in order to show the results provided by the different solutions highlighting the problems of feedback linearizing control and the superior performance of the feedforward-feedback solution.

In Ch.4 which is dedicated to DFIG control under unbalanced dips, after a short introduction, the key ideas for the control strategy is mentioned by recalling the zero dynamics analysis. In the following of this chapter unbalanced voltage dip characterization is carried out, recalling the asymmetric fault effect on the line voltages, which will be exploited to consider a suitable model to be used for control purposes. Then, the proposed control scheme is presented, showing how to design natural-modes-free zero dynamics trajectory under unbalancement, using Sylvester equations, and completing it with LMI-based saturated state feedback design. Line voltage observers and the fault detection method playing vital roles in the unbalanced condition, are explained in details. The approach is validated via detailed simulations. First, comparisons with a recent solution (based solely on control), presented in [28], are discussed. Then, a harsher asymmetric fault case is considered to further motivate and highlight the features of the proposed method. A short conclusion ends the chapter with some final considerations.

Wind turbine control and corresponding mechanical issues are underscored in Ch. 5. In this chapter, WT mechanical and aerodynamics models presented in Ch.1 is exploited for control purposes. The twofold control problem combining the basic HBF objective based on pole placement and the after-dip recovery management is formulated. In the following, first it is shown the system unstable behavior after the line fault, if just standard state feedback configuration is used. Then, the proposed trajectory planning is presented in detail. Finally, simulation results, validating the proposed control strategy, are provided and discussed. Particular attention will be paid to parametric uncertainties, which could affect the model based trajectory

planning. The chapter ends with some final remarks.
Ch.6 is organized to be a framework for the complete benchmark of the studied system under faulty conditions. DFIG and WT models detailed in Ch.1 are utilized again. After considering control objectives and system physical limits, the RSC control proposed in detail in the Ch.3 is briefly recalled and adopted here (starting from known unspecified rotor currents set-points, oscillation-free zero dynamics trajectory are deduced, the corresponding feedforward terms are computed and saturated linear state feedback law, minimizing oscillation under dips is utilized as feedback part). As the main contribution of this chapter, the analytical approach for obtaining rotor current references from original torque and stator reactive current is elaborated, based on the previously obtained oscillation-free zero dynamics trajectories. Numerical simulation results, for a $0.5MW$ DFIG-based WT, to validate the proposed strategy.
The final inspections and remarks are presented in Ch.7 as well as the outlines of the future plans for this study accomplishment.

Chapter 1

Modeling

1.1 Introduction

As we know, the base step of each control process, is to acquire a precise enough dynamic model of the purpose machine with respect to the control objectives. A dynamic model to be considered precise enough must take into account all the important dynamic behaviors of the machine in both steady-state and transient conditions. Moreover, the model should be able to show reasonable reaction to each arbitrary time variation of the control inputs supplying the machine through power electronics converters. In this chapter, such a pre-described models valid for any instantaneous variations under both steady-state and transient operations, will be recalled for DFIG and Wind Turbine machines. Then the so-called Maximum Power Point Tracking algorithm for absorbing the maximum available power from the wind energy is discussed.

1.2 DFIG Model

In this section, after recalling the basic three-phase ABC model of DFIG, in the way of simplification, first the two-axes stationary reference frame called $\alpha - \beta$ model is explained, then the synchronously rotating reference frame conventionally used for the DFIG WT system control is discussed.

1.2.1 ABC Reference Frame

The cross-sectional view of the considered DFIG is shown in Fig. 1.1. A two-pole machine ($n_p = 1$) with symmetrically distributed three-phase windings (equal resistances, magnetizing and leakage inductances for all the three phases) for both stator and rotor is considered. The phases are displaced by 120 electrical degrees

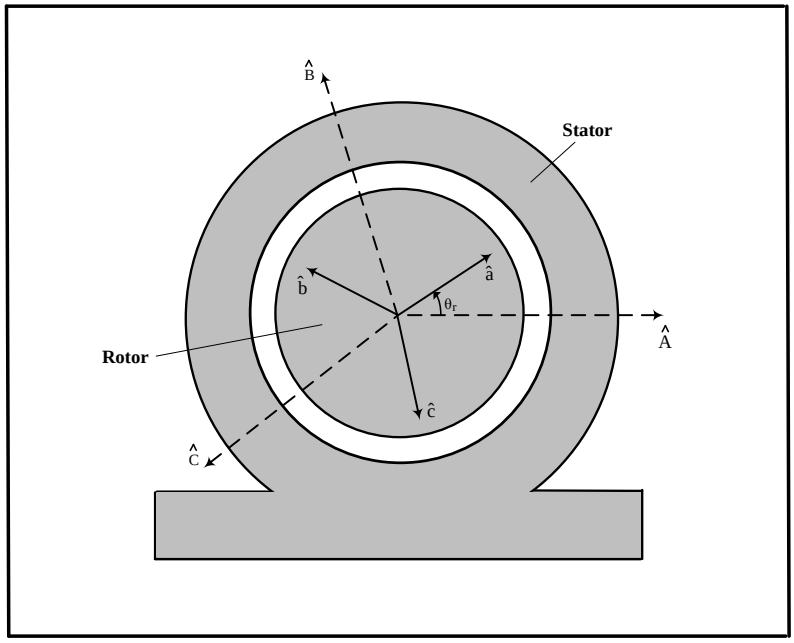

Figure 1.1: A cross-sectional view of the considered DFIG.

from each other in the both three-phase windings, and each rotor phase leads it's corresponding stator phase by phase angle θ_r. Rotor is rotating with the speed $\omega_r = \frac{d\theta_r}{dt}$ in counter-clockwise direction. For sake of simplicity, in developing the ABC model, some other hypotheses are considered as detailed below :

1. Sinusoidal distribution of the electromagnetic force around the stator winding in order to cancel the harmonic components.

2. A constant air-gap is assumed in order to have constant mutual inductances among different phases of stator/rotor windings, and the mutual inductance between stator and rotor depends on the angular position θ_r.

3. $Cross - saturation$ effect and $Skin$ effect are neglected when the former is changing the resistances and leakage inductances due to frequency increase and latter is the coupling between two perpendicular axes.

4. Core iron losses are neglected.

Now applying $Kirchhoff$ and $Faraday$ laws, for the stator phases A, B, and C we can write:

$$\begin{aligned} u_A &= R_S i_A + \frac{d\phi_A}{dt} \\ u_B &= R_S i_B + \frac{d\phi_B}{dt} \\ u_C &= R_S i_C + \frac{d\phi_C}{dt} \end{aligned} \tag{1.1}$$

and in the same way for rotor we have:

$$\begin{aligned} u_a &= R_R i_a + \frac{d\phi_a}{dt} \\ u_b &= R_R i_b + \frac{d\phi_b}{dt} \\ u_c &= R_R i_c + \frac{d\phi_c}{dt} \end{aligned} \tag{1.2}$$

when $u_{A,B,C}/u_{a,b,c}$, $i_{A,B,C}/i_{a,b,c}$, $\phi_{A,B,C}/\phi_{a,b,c}$, and R_S/R_R are respectively stator/rotor voltages, currents, fluxes, and resistances. Taking advantage of the assumptions above, the self inductance of the stator phases are constant and equal, since the flux path for all the three phases are equal. The same reason implies for the mutual inductances among the stator phases (constant and equal). For the rotor windings, the self inductances are constant and equal as well, while the mutual one depend on the rotor position. Therefore, the stator and rotor flux relations can be expressed in the following equations (1.3) and (1.4) [45]:

$$\begin{bmatrix} \phi_A \\ \phi_B \\ \phi_C \end{bmatrix} = L_S \begin{bmatrix} 1 & -\frac{1}{2} & -\frac{1}{2} \\ -\frac{1}{2} & 1 & -\frac{1}{2} \\ -\frac{1}{2} & -\frac{1}{2} & 1 \end{bmatrix} \begin{bmatrix} \imath_A \\ \imath_B \\ \imath_C \end{bmatrix} + L_m \begin{bmatrix} cos(\theta_r) & cos(\theta_r + \frac{2\pi}{3}) & cos(\theta_r - \frac{2\pi}{3}) \\ cos(\theta_r - \frac{2\pi}{3}) & cos(\theta_r) & cos(\theta_r + \frac{2\pi}{3}) \\ cos(\theta_r + \frac{2\pi}{3}) & cos(\theta_r - \frac{2\pi}{3}) & cos(\theta_r) \end{bmatrix} \begin{bmatrix} \imath_a \\ \imath_b \\ \imath_c \end{bmatrix} \tag{1.3}$$

$$\begin{bmatrix} \phi_a \\ \phi_b \\ \phi_c \end{bmatrix} = L_R \begin{bmatrix} 1 & -\frac{1}{2} & -\frac{1}{2} \\ -\frac{1}{2} & 1 & -\frac{1}{2} \\ -\frac{1}{2} & -\frac{1}{2} & 1 \end{bmatrix} \begin{bmatrix} \imath_a \\ \imath_b \\ \imath_c \end{bmatrix} + L_m \begin{bmatrix} cos(\theta_r) & cos(\theta_r + \frac{2\pi}{3}) & cos(\theta_r - \frac{2\pi}{3}) \\ cos(\theta_r - \frac{2\pi}{3}) & cos(\theta_r) & cos(\theta_r + \frac{2\pi}{3}) \\ cos(\theta_r + \frac{2\pi}{3}) & cos(\theta_r - \frac{2\pi}{3}) & cos(\theta_r) \end{bmatrix} \begin{bmatrix} \imath_A \\ \imath_B \\ \imath_C \end{bmatrix} \tag{1.4}$$

1.2.2 Two-axes Stationary Reference Frame

As can be seen from the equations (1.3) and (1.4), the inductance matrix depends on the rotor position, thus it is also time dependent. In order to obtain a dynamic model with constant inductance matrices which imposes less complexity and computation/simulation times, two-axes stationary reference frame commonly called $\alpha - \beta$ is introduced. This frame consists of two stationary orthogonal axes α and β either fixed on the stator or rotor which are indicated respectively by x_α, x_β and x_x, x_y variables. The Fig. 1.2 shows the schematic diagram of the $\alpha - \beta$ and $x - y$ stationary reference frames whose α, and x axes are respectively fixed on the stator

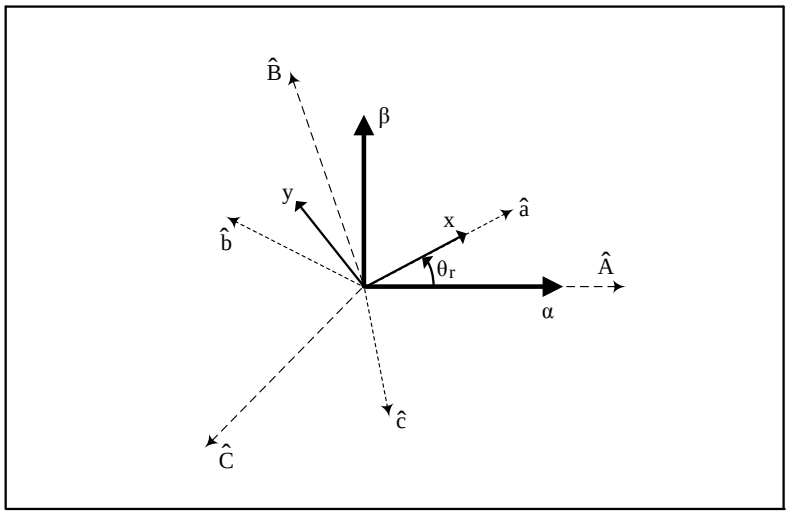

Figure 1.2: Stator $(\alpha - \beta)$ and rotor $(x - y)$ two-axis reference frames.

phase A and rotor phase a of the three-phase systems. By projecting the three-phase quantities onto two stationary axes, the following transformation matrix can be obtained [45]:

$$T_{3\to2} = k \begin{bmatrix} 1 & -\frac{1}{2} & -\frac{1}{2} \\ 0 & \frac{\sqrt{3}}{2} & -\frac{\sqrt{3}}{2} \end{bmatrix} \tag{1.5}$$

inversing the matrix (1.5), we have:

$$T_{2\to3} = \frac{2}{2k} \begin{bmatrix} 1 & 0 \\ -\frac{1}{2} & \frac{\sqrt{3}}{2} \\ -\frac{1}{2} & -\frac{\sqrt{3}}{2} \end{bmatrix} \tag{1.6}$$

Using the transformation matrices in (1.6), and (1.5), we can easily switch from Cartesian three-phase system to it's equivalent $\alpha - \beta$ and $x - y$ stationary reference frames and vice versa as the following equations show:

$$\begin{bmatrix} x_\alpha \\ x_\beta \end{bmatrix} = T_{3\to2} \begin{bmatrix} x_A \\ x_B \\ x_C \end{bmatrix}, \quad \begin{bmatrix} x_A \\ x_B \\ x_C \end{bmatrix} = T_{2\to3} \begin{bmatrix} x_\alpha \\ x_\beta \end{bmatrix} \tag{1.7}$$

$$\begin{bmatrix} x_x \\ x_y \end{bmatrix} = T_{3\to2} \begin{bmatrix} x_a \\ x_b \\ x_c \end{bmatrix}, \quad \begin{bmatrix} x_a \\ x_b \\ x_c \end{bmatrix} = T_{2\to3} \begin{bmatrix} x_x \\ x_y \end{bmatrix} \tag{1.8}$$

So by expressing the general DFIG model in terms of the two-phase $\alpha - \beta$ and $x - y$ stationary reference frames, we will obtain:

$$\begin{aligned} u_\alpha &= R_S i_\alpha + \frac{d\phi_\alpha}{dt} \\ u_\beta &= R_S i_\beta + \frac{d\phi_\beta}{dt} \end{aligned} \tag{1.9}$$

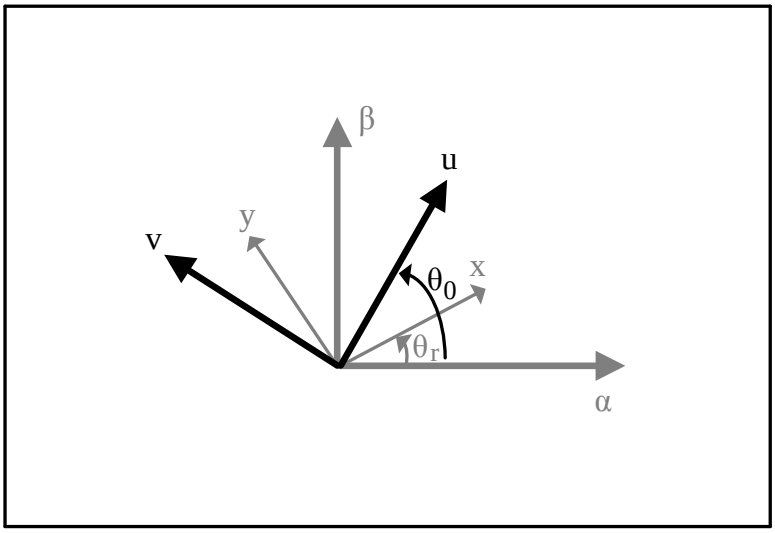

Figure 1.3: $(u - v)$ two-axis reference frame.

and for the rotor:

$$\begin{aligned} u_x &= R_R i_x + \frac{d\phi_x}{dt} \\ u_y &= R_R i_y + \frac{d\phi_y}{dt} \end{aligned} \tag{1.10}$$

Thus, the expression of flows in two-phase references will be:

$$\begin{bmatrix} \phi_\alpha \\ \phi_\beta \end{bmatrix} = L_1 \begin{bmatrix} i_\alpha \\ i_\beta \end{bmatrix} + L_m e^{J\theta_r} \begin{bmatrix} i_x \\ i_y \end{bmatrix} \tag{1.11}$$

,

$$\begin{bmatrix} \phi_x \\ \phi_y \end{bmatrix} = L_2 \begin{bmatrix} i_x \\ i_y \end{bmatrix} + L_m e^{-J\theta_r} \begin{bmatrix} i_\alpha \\ i_\beta \end{bmatrix} \tag{1.12}$$

where $L_1 = \frac{3L_S}{2}$, $L_2 = \frac{3L_R}{2}$, $L_m = \frac{3L_M}{2}$, and $e^{J\theta}$ indicates the rotation matrix for an angle θ on the plane as:

$$e^{J\theta} = \begin{bmatrix} cos(\theta) & -sin(\theta) \\ sin(\theta) & cos(\theta) \end{bmatrix} \tag{1.13}$$

1.2.3 Synchronously Rotating Reference Frame

In the equations (1.9), (1.10) the two-axes stator and rotor quantities were referring to different reference systems. Now the dynamic model of DFIG by expressing stator and rotor windings relative to an unique Cartesian reference system $u - v$ is discussed. This system is rotating by a generic angle θ_0 with respect to stator reference $\alpha - \beta$, see Fig. . By indicating with the script 1 and 2 respectively for stator and rotor windings, we have [45]:

$$\begin{bmatrix} x_{1u} \\ x_{1v} \end{bmatrix} = e^{-J\theta_0} \begin{bmatrix} x_\alpha \\ x_\beta \end{bmatrix}, or \begin{bmatrix} x_\alpha \\ x_\beta \end{bmatrix} = e^{J\theta_0} \begin{bmatrix} x_{1u} \\ x_{1v} \end{bmatrix} \tag{1.14}$$

$$\begin{bmatrix} x_{2u} \\ x_{2v} \end{bmatrix} = e^{-J(\theta_0-\theta_r)} \begin{bmatrix} x_x \\ x_y \end{bmatrix}, or \begin{bmatrix} x_x \\ x_y \end{bmatrix} = e^{J(\theta_0-\theta_r)} \begin{bmatrix} x_{2u} \\ x_{2v} \end{bmatrix} \tag{1.15}$$

Therefore, the model expressed in this frame will be:

$$\begin{bmatrix} u_{1u} \\ u_{1v} \end{bmatrix} = R_s \begin{bmatrix} i_{1u} \\ i_{1v} \end{bmatrix} + \begin{bmatrix} \dot{\phi}_{1u} \\ \dot{\phi}_{1v} \end{bmatrix} + \begin{bmatrix} 0 & -\omega_0 \\ \omega_0 & 0 \end{bmatrix} \begin{bmatrix} \phi_{1u} \\ \phi_{1v} \end{bmatrix} \tag{1.16}$$

$$\begin{bmatrix} u_{2u} \\ u_{2v} \end{bmatrix} = R_R \begin{bmatrix} i_{2u} \\ i_{2v} \end{bmatrix} + \begin{bmatrix} \dot{\phi}_{2u} \\ \dot{\phi}_{2v} \end{bmatrix} + \begin{bmatrix} 0 & -(\omega_0-\omega_r) \\ (\omega_0-\omega_r) & 0 \end{bmatrix} \begin{bmatrix} \phi_{2u} \\ \phi_{2v} \end{bmatrix} \tag{1.17}$$

$$\begin{bmatrix} \phi_{1u} \\ \phi_{1v} \end{bmatrix} = L_1 \begin{bmatrix} i_{1u} \\ i_{1v} \end{bmatrix} + L_m \begin{bmatrix} i_{2u} \\ i_{2v} \end{bmatrix} \tag{1.18}$$

$$\begin{bmatrix} \phi_{2u} \\ \phi_{2v} \end{bmatrix} = L_2 \begin{bmatrix} i_{2u} \\ i_{2v} \end{bmatrix} + L_m \begin{bmatrix} i_{1u} \\ i_{1v} \end{bmatrix} \tag{1.19}$$

also for electromagnetic torque, we can write:

$$T_m = \frac{2n_p}{3k^2} L_m \begin{bmatrix} i_{1u} & i_{1v} \end{bmatrix} J \begin{bmatrix} i_{2u} \\ i_{2v} \end{bmatrix} \tag{1.20}$$

where $\omega_0 = \dot{\theta}_0$.

The electric model of DFIG is a fourth-order system, to be expressed in state space form $\dot{x} = f(x, u)$, four independent state variables should be selected. Generally, a set of stator/rotor currents and fluxes is selected.

Therefore, under above-mentioned standard hypotheses the electromagnetic dynamic model of DFIG in the Stator Voltage Oriented (SVO) $(u-v)$ reference frame can be expressed as the two following representations, which will be respectively referred as $i_1 - \phi_2$ and $i_2 - \phi_1$ models in this thesis. In particular, in SVO $(u-v)$ reference frame, u-axis is aligned to the stator voltage vector which corresponds to the line voltage one, owing to the typical connection of DFIG.

$i_1 - \phi_2$ Model

Choosing the stator currents i_{1u}, i_{1v} and the rotor fluxes ϕ_{2u}, ϕ_{2v} as the state variables, the DFIM dynamics in the previously mentioned SVO reference frame read as:

$$\begin{aligned}
\dot{i}_{1u} &= -\gamma_1 i_{1u} + \omega_0 i_{1v} + \alpha_2\beta_1\phi_{2u} + \beta_1\omega_r\phi_{2v} + \frac{U}{\sigma_1} - \beta_1 u_{2u} \\
\dot{i}_{1v} &= -\omega_0 i_{1u} - \gamma_1 i_{1v} - \beta_1\omega_r\phi_{2u} + \alpha_2\beta_1\phi_{2v} - \beta_1 u_{2v} \\
\dot{\phi}_{2u} &= -\alpha_2\phi_{2u} + (\omega_0-\omega_r)\phi_{2v} + \alpha_2 L_m i_{1u} + u_{2u} \\
\dot{\phi}_{2v} &= -(\omega_0-\omega_r)\phi_{2u} - \alpha_2\phi_{2v} + \alpha_2 L_m i_{1v} + u_{2v} \\
T_m &= \eta_1(\phi_{2u} i_{1v} - \phi_{2v} i_{1u})
\end{aligned} \tag{1.21}$$

where U is the line voltage amplitude (since stator windings are directly connected to the grid), ω_0 is the line angular frequency, and ω_r is the rotor angular speed multiplied by the number of pole pairs n. The system control inputs are the rotor voltages u_{2u}, u_{2v}, while T_m in the last equation is the electromagnetic torque. To compact notation, the following positive parameters have been defined:

$$\begin{aligned} &\sigma_1 = L_1\left(1-\frac{L_m^2}{L_1L_2}\right), \beta_1 = \frac{L_m}{\sigma_1 L_2}, \alpha_2 = -\frac{R_2}{L_2}, \\ &\gamma_1 = \left(\frac{R_1}{\sigma_1}+\alpha_2\beta_1 L_m\right),\ \eta_1 = \frac{3nL_m}{2L_2} \end{aligned} \tag{1.22}$$

the nomenclature of the electrical parameters appearing in the equation above is reported in Tab. A.1, in the Appendix.

$i_2 - \phi_1$ Model

Alternatively, if we select the rotor currents i_{2u}, i_{2v} and stator fluxes ϕ_{1u}, ϕ_{1v} as the state variables, the DFIM dynamic model becomes:

$$\begin{aligned} \dot{i}_{2u} &= -\gamma_2 i_{2u} + (\omega_0-\omega_r)i_{2v} + \beta_2\alpha_1\phi_{1u} - \beta_2\omega_r\phi_{1v} - \beta_2 U + \frac{1}{\sigma_2}u_{2u} \\ \dot{i}_{2v} &= -(\omega_0-\omega_r)i_{2u} - \gamma_2 i_{2v} + \beta_2\omega_r\phi_{1u} + \beta_2\alpha_1\phi_{1v} + \frac{1}{\sigma_2}u_{2v} \\ \dot{\phi}_{1u} &= -\alpha_1\phi_{1u} + \omega_0\phi_{1v} + \alpha_1 L_m i_{2u} + U \\ \dot{\phi}_{1v} &= -\omega_0\phi_{1u} - \alpha_1\phi_{1v} + \alpha_1 L_m i_{2v} \\ T_m &= \eta_2(\phi_{1v}i_{2u} - \phi_{1u}i_{2v}) \end{aligned} \tag{1.23}$$

with the following positive parameters:

$$\begin{aligned} &\sigma_2 = L_2\left(1-\frac{L_m^2}{L_1L_2}\right), \beta_2 = \frac{L_m}{\sigma_2 L_1}, \alpha_1 = -\frac{R_1}{L_1}, \\ &\gamma_2 = \left(\frac{R_2}{\sigma_2}+\alpha_1\beta_2 L_m\right),\ \eta_2 = \frac{3nL_m}{2L_1} \end{aligned} \tag{1.24}$$

and the electrical coefficients of (1.24) reported in Tab. A.1.
Note that representations (1.21)-(1.23) are easily convertible into any another by means of the equations (1.18), and (1.19).

1.3 Wind Turbine Model

In this thesis, a standard two-mass model [46], illustrated in Fig.1.4, is considered in order to analyze and control Wind Turbine (WT) mechanical system. The cor-

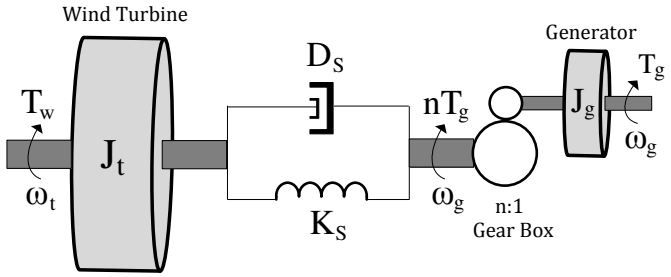

Figure 1.4: Standard two-mass wind turbine model with gearbox.

responding dynamics is represented as:

$$\begin{aligned}\dot{\theta}_d &= \frac{\omega_g}{n} - \omega_t \\ \dot{\omega}_t &= \frac{1}{J_t}\left(T_w(\omega_t, \beta, V_w) + K_s\theta_d + D_s\left(\frac{\omega_g}{n} - \omega_t\right)\right) \\ \dot{\omega}_g &= \frac{1}{J_g}\left(-K_s\frac{\theta_d}{n} - \frac{D_s}{n}\left(\frac{\omega_g}{n} - \omega_t\right) - T_g\right)\end{aligned} \tag{1.25}$$

Where $\theta_d = \theta_t - \frac{\theta_g}{n}$ is the drive-train low speed shaft torsional displacement, ω_t and ω_g are turbine and generator angular speeds, respectively. J_t and J_g are the turbine and generator inertias, while n is the coefficient of the gearbox connecting the high speed shaft (assumed perfectly rigid) and the low speed shaft. Also, D_s and K_s are the low speed shaft damping and stiffness coefficients, respectively.
The generator and aerodynamic torques are denoted with T_g and T_w, where the latter depend on the turbine speed, the wind speed V_w and the blade pitch angle β as [47]:

$$T_w(\omega_t, \beta, V_w) = \frac{1}{2}\frac{\rho\pi R_w^3 V_w^2 C_P(\lambda, \beta)}{\lambda} \tag{1.26}$$

with the blade tip speed ratio λ:

$$\lambda = \frac{\omega_t R_w}{V_w} \tag{1.27}$$

where ρ is the air density, R_w the blades radius and λ is the so-called tip speed ratio. C_P is the power coefficient that, beside depending on the specific blade characteristic, for standard horizontal axis WT, can be approximated as [48]:

$$C_P = 0.22\left(\frac{116}{\lambda_i} - 0.4\beta - 5\right)e^{-\frac{12.5}{\lambda_i}} \tag{1.28}$$

where:

$$\lambda_i = \frac{1}{\frac{1}{\lambda + 0.08\beta} - \frac{0.035}{\beta^3 + 1}} \tag{1.29}$$

As regards the WT control, in the following chapters, Maximum Power Point Tracking (MPPT) and Pitch Control as the two standard methods for optimizing the power extracted from the wind energy, will be shortly discussed. The latter is also utilized for preventing over rated power production in high wind rates.

Chapter 2

Low Voltage Ride Through and Voltage Dips Definition

2.1 Introduction

This chapter explains Low Voltage Ride Through (LVRT) capability for Wind Energy Conversion Systems (WECSs), requested by modern national grid codes. By definition, LVRT asks WECSs to remain connected to the power grid while some classes of faults take place, categorized based on voltage reduction and fault duration. Under voltage dips, another aspect of LVRT must be complied with WECSs is to supply reactive power to the network in order to help sustaining the voltage profile. Voltage dips disturb the generation and transmission power balance of WECSs by reducing dramatically the power can be transmitted to the grid. Moreover, as it will be detailed in the next parts, voltage dips jeopardize the DFIG-based Wind Turbine (WT) system by triggering large electrical (stator/rotor current/flux) and mechanical oscillations beyond the system physical limits. There exists some standard classifications of the power system short-circuits leading to different style voltage drops. In the following, one of these fault classifications will be briefly explained, and the LVRT regulations determined by a few famous national grid codes will be presented. In the last part, voltage dip drawbacks and the classic remedy for the DFIG WT system will be briefly discussed.

2.2 Types of Voltage Dips

A voltage dip is a fleeting decline (from 0.5 to 30 cycles) in the grid voltage profile stemming from different short-circuit faults in the network or due to starting of heavy inductive loads. A typical power system voltage dip consists of three stages where the voltage is falling, stabilizing, and recovering as shown in the Fig. 2.1.

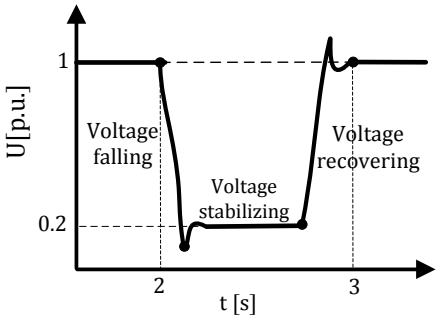

Figure 2.1: A typical voltage dip of the power system.

At the falling stage, the voltage profile drops to a certain level i.e. $0.15p.u.$ in few tens of milliseconds (e.g. $30ms$), conventionally called 85% voltage drop. The fallen profile may stabilize there within a period of several cycles equal to few hundreds of milliseconds (e.g. $200ms$). When the fault's origin is removed, the system starts recovering to it's pre-fault situation within a time dependent on the system structure (specially the control strategy) within a time differing from a few milliseconds to even several thousands od milliseconds.
The most common classification for the mentioned faults is dividing them into two symmetrical (balanced) and asymmetrical (unbalanced) sections. The former is a short-circuit leading to identically equal reductions in all the three phases, while the latter imposes different changes in terms of amplitude or/and phase angle in each phase. When a fault takes place, the magnitude and phase angle jump at a specific location, depends on the several factors including the fault type, the distance from the fault origin, the network impedance, the power system equipments nearby installed (e.g. the transformers type connections delta, wye, etc.). The most common balanced fault in the power system is single-phase to- ground fault (SPGF), where the voltage drops in one phase, while the other two phases remain unchanged. The most conventional reason of SPGF is lightning strike at the power transmission area. Phase-to-phase (PPF) is another frequent unbalanced fault which imposes amplitude reduction and phase angle delay in two faulty phases, while the third phase remains fixed. Although the occurrence rate for balanced faults i.e. three-phase short-circuit is a bit lower, but the resulting drawbacks are much more severe compared with their unbalance counterpart. From power system statistical viewpoints, the three-phase faults happen in results of large induction motors start ups, transformers energizing, and lightning-based short circuits, ice, tree, animal, or wind touches.

Another way for categorizing the mentioned fault is to use ABC classification, including one balance, and six different unbalanced faults as shown in Fig. In this classification, the positive- and negative-source impedances are supposed equal. The

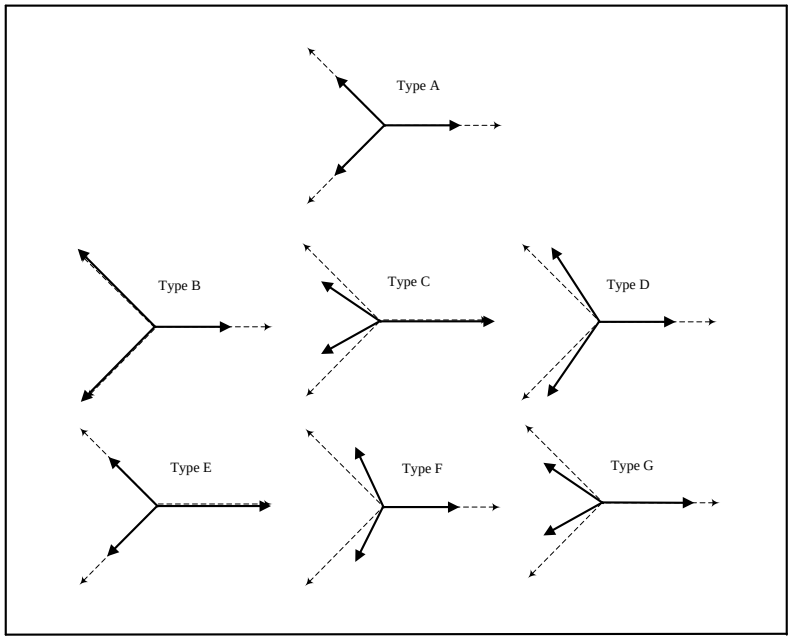

Figure 2.2: ABC classification of the power system's short-circuits.

mentioned balanced three-phase fault is titled type A here, while SPGF and PPF are called type B, and C respectively. As can be seen in Fig.2.2, two out of three phases experience voltage drops with an associated phase-angle-jump. The type D is dedicated to a PPF through a delta-wye transformer, or two SPGFs within two delta-wye transformers. In this type, all the three phases face voltage reduction plus phase-angle-jumps for two faulty ones. The next one, type E stems from a phase-to-phase-to-ground fault (PPGF), in which one phase remains unchanged and the other two phases drop in magnitude only. The type F results from a PPGF happening through a delta-wye transformer, while finally type G is a type F fault occurring through two delta-wye transformers. As depicted in the Fig., in both cases drops for all the three phases, but in term of phase-angle-jump, one phase is safe and the other two phases face respectively lag and lead jumps for F and G.

2.3 LVRT Definitions by National Grid Codes

In several countries, the WECSs' share of total energy capacity has exponentially increased within recent years. The United States has led the world by generating around $140.9TWh$ wind-power electricity in 2012, followed by China, Spain, and Germany by respectively $118.1TWh$, $49.1TWh$, and $46.0TWh$ productions. These large penetration of wind-power units in the national power system, has motivated several countries to establish some national grid codes and regulations for managing the WECSs' commitments. As mentioned before, one of the most vital regulations

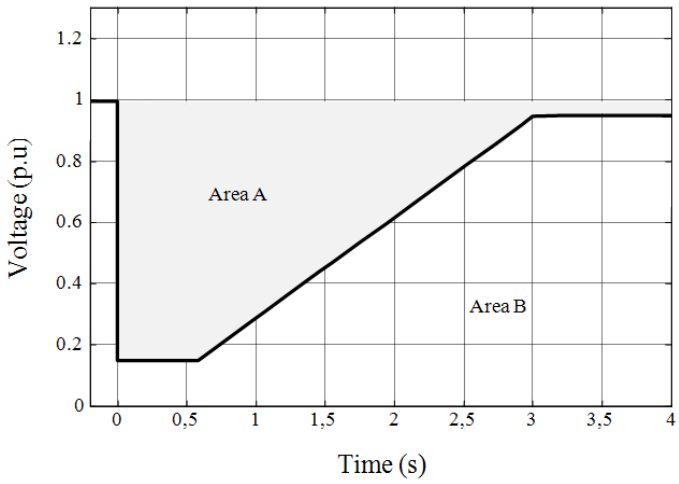

Figure 2.3: The general voltage profile required by LVRT national grid codes.

is LVRT, urging the wind-power units to ride through within voltage dips, whose severity is defined in terms of magnitude drop percentage and fault time duration. Fig. 2.3 shows the general voltage profile presented in the different national grid codes to define LVRT voltage regulation. In this cure, $AreaA$ specifies the ride through zone, where the wind-power unit must stay online supplying the power network by reactive power, while they are allowed to disconnect when the occurred fault is deep or/and long enough as illustrated as $AreaB$.
Fig.2.4 shows four different LVRT national grid codes. German $E.ONNetz$ is a pioneer institution in Europe, requiring LVRT for the minimum voltage $0.15p.u.$ and time duration $625ms$, while the complete recovery time is around $1.5s$. For American $FERC$, as another good instance, WECSs must abide even harsher faults while the voltage profile may drop to identical zero within around $150ms$, and the system rehabilitates the pre-fault condition along almost $3s$. As can be seen in the Fig., in the Italian and Danish grid codes the voltage profile faces around 80% decline and reaches back to $0.75p.u.$ approximately in $700ms$. Another aspect of LVRT regulation, as mentioned before, is reactive power support of the power grid under faulty condition which is commonly presented as the machine's (here DFIG) reactive component of the stator current. As Fig.2.5 depicts, the DFIG's stator current reactive component must remain higher than $0.9p.u.$ along the fault duration. This reactive power injection insures the local power network's reliability under the voltage reduction.

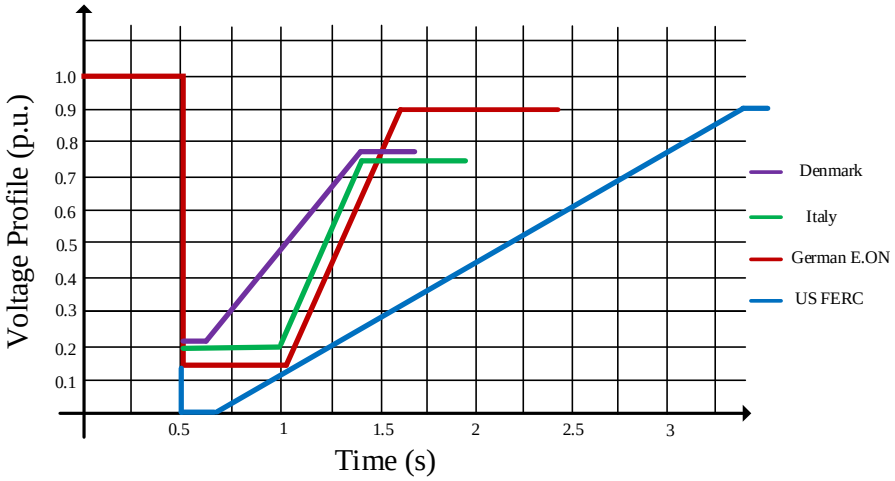

Figure 2.4: National grid code examples for LVRT voltage regulation.

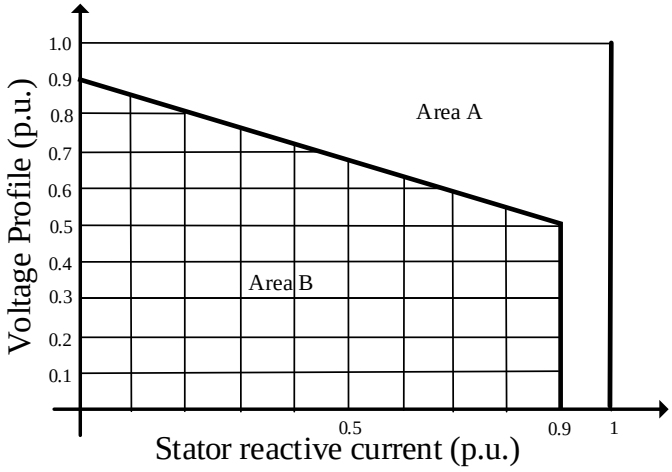

Figure 2.5: The general reactive power required by LVRT national grid codes.

2.4 Voltage Dip Drawbacks and Classic Remedy

Under SVO synchronously rotating reference frame $(u-v)$ and in the steady-state operating condition, the u-component of the DFIG's stator voltage is constant, while the v-component is identically zero. This situation is also preserved under the faulty condition, for some types of voltage dips like SPGF. The equation (2.1) illustrates the active power relation in the afore-mentioned reference frame.

$$P = \frac{3}{2}(U_u i_{iu} + U_v i_{i1v}) \tag{2.1}$$

The active power dependency to the component U_u is clear. Thus, as mentioned before, under the voltage dip, the active power which can be transmitted to the grid is severely constrained. This leads to an active power mismatch, since the production would overtake the consumption under the voltage fault. The power mismatch itself could cause a high over-voltage in the $DC-Link$ due to the converter's current constraints. A straightforward solution for the power mismatch is reducing the generator's torque as well when the voltage dip occurrence is detected by suitable adopted observers. The second important drawback caused by voltage dip is high sensitivity of DFIG to such kind of perturbations. The main reason behind this is that the stator winding of DFIG is directly connected to the power grid. As will be discussed deeply in the following chapters, from the control viewpoints, it can be proved that the stator voltage of DFIG inters its internal dynamic system as an exogenous perturbation. Thus, an abrupt reduction under the voltage dip, leads directly to the stator flux and current oscillations, resulting in corresponding rotor oscillations as well, since it is electromagnetically connected to the stator. These large oscillations if are not smartly controlled, can hit the system's physical limits like power-electronic converters' current constraint. As we know, modern power-electronic components are all equipped with over-current protection units trapping them in the risky conditions. But this trap mode should be prevented to hold the system alive based on the LVRT regulations. The conventional remedy for under-dip oscillations is installing a crowbar protection, as a physical static resistance short-circuiting the rotor winding along with the voltage fault. In this way, the harmful effects of the mentioned oscillations is avoided in the rotor part whose components are more vulnerable compared with the stator's. But, we should pay a big price for the protections in two terms: a) it imposes an additional hardware to the system which is not cheap at all. b) short-circuiting the rotor winding means hindering the LVRT performance since we have actually sacrificed the system controllability function by excluding the Rotor-Side Converter (RSC). Put aside this another negative point that we are dissipating energy in the static resistors by each crowbar connection. These mentioned drawbacks motivated researchers to investigate alternative

cheaper solutions.

Chapter 3

DFIG Control under Balanced Dips

3.1 Introduction

As mentioned before in Introduction, DFIG is a wound-rotor machine, where both stator and rotor windings can be fed independently. The typical connection scheme of power generation systems with DFIG is shown in Fig. 3.1. In the modern wind turbines, control theory plays a vital role to substantiate superior dynamic and steady-state performance of DFIG. As a matter of fact, while the GSC can be controlled by applying standard techniques defined for any electric drive with an Active Front End [9], the control problem related to DFIG, steered through the RSC, is rather peculiar and involved in the electric drives field. Many control solutions have been proposed for such kind of machine, in order to achieve decoupled control of the active and reactive power generated at stator side. As mentioned before, nowadays, in order to be integrated to the power system, wind generation units should comply with Low Voltage Ride Through (LVRT) regulations requested by the grid codes [18], [19]. The main drawbacks of voltage dips as severe disturbances for DFIG, were discussed in the Introduction and previous chapter, which are briefly recalled as the following points:

1. surplus power happened due to reduction of the transmission rate from the wind generation unit to the power grid.

2. each line voltage variation during the grid fault, as a disturbance, triggers high oscillations in fluxes, and currents of the both stator and rotor windings (because the stator is directly connected to the three-phase grid and rotor is electromagnetically coupled to the stator).

3. voltage perturbation also makes standard controllers give large voltage commands on RSC, hitting the saturation constraints and possibly leading to converter overcurrents.

4. all of these electrical transients will affect the torque command and the actual torque of the DFIG, this can trigger mechanical dynamics of the generator and its prime mover, as well, if relevant mechanical resonances characterize the driveline.

Many solutions are suggested in literature in order to solve the mentioned surplus power issue, to face the voltage disturbance on DFIG and to prevent damages to the power converter (both RSC and GSC) during the dip. As mentioned before, using crowbars to short-circuit the rotor winding during the fault is the most widely used remedy in the currently installed wind turbines. But, crowbar solution not only imposes an extra cost to the system, but also hinders the LVRT compliance of DFIM for the temporary uncontrollability of the system caused by short-circuiting the rotor windings. Therefore, other solutions have been proposed. As mentioned in the Introduction, despite the large literature on LVRT and DFIM, they have mostly focused on the above-mentioned power surplus and no enough analysis is given for what concerns the effects of voltage dip on the DFIG electromagnetic dynamics and control solutions to cope with. In this chapter, a control solution for DFIG (i.e. acting on the RSC) is proposed to tame effectively the consequences of symmetrical three-phase voltage dips (as the most severe type of the power system's short-circuits) and achieve full LVRT capability, potentially avoiding the crowbar use. As mentioned, DFIG's general control objectives are usually presented as known reference torque and reactive power at the stator side which should be translated into the corresponding reference stator/rotor currents. In this chapter, stator/rotor currents are assumed as output variables in order to derive

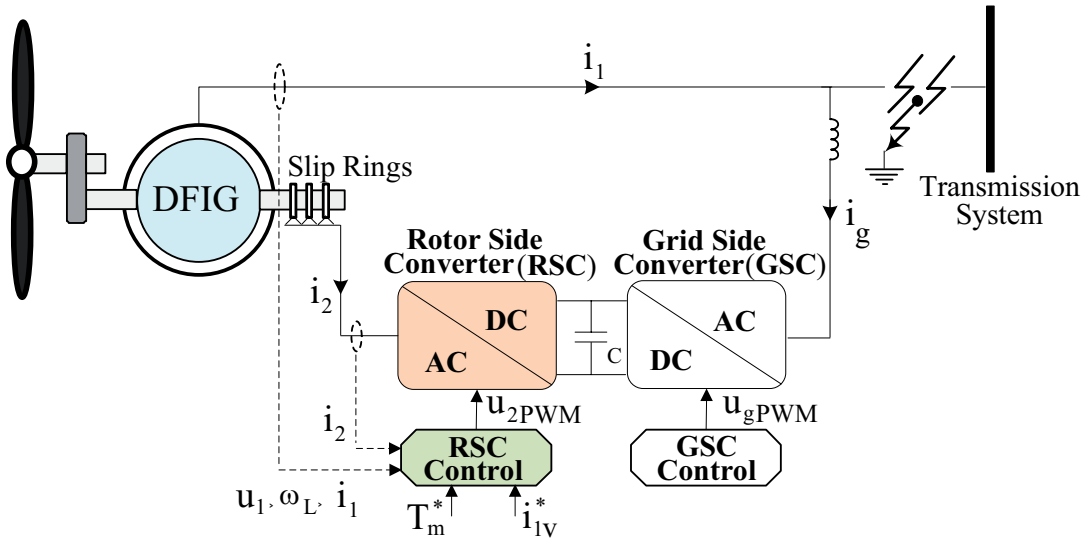

Figure 3.1: Typical connection scheme of power generation system with DFIG.

the corresponding Brunovsky forms of the system dynamics. Then, to avoid unpleasant oscillatory behavior of the internal dynamics, the zero dynamics are deeply analyzed and suitable trajectories are designed. After that, in purpose of having a clear analysis for the effects of the line perturbation on the system, a standard feedback linearizing control is adopted assuming the rotor currents as output variables (since the rotor output form gives an asymptotically stable zero dynamics, versus a marginally stable one for the stator output form). It will be shown in the first set of simulations that system equipped with such kind of controller is not able to damp oscillations neither to solve the control voltage saturation problem. Hence, a mixed feedforward-feedback control solution is proposed. The feedforward part is designed exploiting the above-mentioned oscillation-free rotor-based reference state trajectories. The feedback part is a state feedback taking advantage of the results in [41]. It exploits saturated control techniques to deal with voltage limits and to reduce the rotor current oscillations under symmetrical three-phase voltage dip, as the most significant constraints to deal with, since they could lead to RSC overcurrent. Simulations are provided in order to substantiate the theoretical results, considering a 0.5MW DFIM.

Some preliminary results have been reported in [49]. In that paper, just a partial analysis of the voltage dip effects has been carried out and no modern saturated control techniques have been exploited for dealing with RSC voltage limits. A comprehensive version of this chapter is published in [50]. The reminder of this chapter is organized as follows. In Section 3.2, the general objectives and some physical limits are explained. In Section 3.3, the Brunovsky (Normal) forms of the system dynamics are generated assuming two different sets of outputs, namely stator and rotor currents. Then, on the way of trajectory planning, corresponding zero dynamics ODE are solved analytically in two ways: exploiting Sylvester equation and integrating by parts. In Section 3.4, the effect of the line voltage disturbances are analyzed by considering the zero dynamics with respect to the rotor currents and by studying the system behavior, when a standard feedback linearizing controller is imposed, using the rotor currents as outputs. In Section 3.5, first, the previously-designed reference trajectory is employed in an open-loop controller. Then, a feedforward-feedback control strategy is proposed relying on modern saturated control techniques to deal with control voltage limits; in addition, an LMI-constrained convex optimization problem is defined to minimize the oscillations under voltage dips. Simulations are provided in all of the previous Sections in order to show the results provided by the different solutions highlighting the problems of standard approach of Section 3.4 and the superior performance of the feedforward-feedback solution of Section 3.5. Some final remarks on the presented solution and future developments are drawn in Section 3.6.

3.2 Objectives and Constraints

The stator-side torque and reactive power are a pair of reference values which are commonly used for stating the the control objectives of DFIG. The torque relation is repeated here to remind in the last equations of (1.21), (1.23) in the Chapter.1:

$$T_m = \eta_1(\phi_{2u} i_{1v} - \phi_{2v} i_{1u}) = \eta_2(\phi_{1v} i_{2u} - \phi_{1u} i_{2v}). \tag{3.1}$$

and reactive power Q is given by:

$$Q = -\frac{3}{2} U i_{1v} = -\frac{3}{2} U \left[\frac{\phi_{1v} - L_m i_{2v}}{L_1}\right]. \tag{3.2}$$

From the control viewpoints, these reference values should be translated to the corresponding reference stator/rotor currents or into the reference pairs: stator currents and rotor fluxes or stator fluxes and rotor currents, according to the representations given in the first chapter. Since we have two reference trajectories and four state variables, infinite solutions are available for such translation. But, on the other hand, there are some physical limits should be taken into account in determining the state variables trajectories. The following items are the most important constraints:

1. Rotor current limits, because of the maximum rating of the RSC power electronic switches.

2. Flux saturation limits, addressing the magnetic core saturations.

3. Bounded control inputs, i.e. rotor voltages, again due to the RSC power electronics limitations.

Moreover, as the system has only two control inputs, clearly the evolution of the four state variables cannot be set arbitrarily. In other words, some dependencies will take place according to the system relative degree with respect to control inputs, and the form of the corresponding internal dynamics.
Finally, as mentioned before, to ensure the graceful performance, DFIG must comply with the LVRT modern grid regulations. So, the reference trajectories should be designed in adaption with the grid voltage perturbations. It will be detailed later that the above-mentioned constraints are completely related to the voltage disturbance, hence it is the most importance issue. To clarify more, a good performance under the faulty voltage conditions means to make DFIG remain connected to the grid, preventing boundaries' violations by the machine signals, according to the modern grid codes. Operationally speaking, since we have two reference signals as electromagnetic torque and reactive power at the stator side, versus four state variables, two out of the four states are considered known, and the other two will be

designed. Therefore, instead of the mentioned stator-side references torque (T_m^*) and reactive power (Q^*), a pair of known references for stator or rotor currents (depending on the considered state-space model) will be assumed. Then, the corresponding rotor or stator fluxes trajectories will be designed, taking into account all the above-mentioned issues and constraints. In the next chapters, we will discuss in details an exact translation of the mentioned original reference signals to the DFIG's reference rotor currents, considering assuming reference signals belonging to some classes of functions (e.g. piecewise linear, quadratic and so forth). Hence, from now on, the desired T_m^* and Q^* will be substituted with their equivalent known stator or rotor current references. Moreover, the stator or rotor current references will be assumed arbitrarily smooth and with known derivatives of any order, according to control requests. All in all, according to standard DFIG setups and regarding the available measurements and parameters, the machine parameters are assumed known, ω_r and the corresponding rotor angle are assumed measurable, the stator and rotor currents and the line voltages are assumed available from sensor readings, as well. Moreover, whatever state representation can be retrieved by means of the machine parameters, and stator and rotor current measurements. Therefore, full state measurement can be assumed available for feedback.

3.3 Brunovsky Forms and Trajectory Planning

According to what mentioned in the Section above, known references are assumed for two out of the four state variables of the DFIG model. Here, the stator or rotor currents trajectories are assumed as such known signals. Thus, for the models (1.21), (1.23), with respectively stator or rotor currents outputs, the corresponding Brunovsky forms [40] will be analyzed. This Section is devoted to this purpose which is crucial for planing suitable trajectories for the remainder state components (rotor and stator fluxes in the considered representations), but also to highlight the properties of the corresponding zero dynamics, which will be profitably exploited later on, for designing the proposed control strategy.

3.3.1 Normal Brunowsky form with respect to Output Stator Currents

If stator currents i_{1u}, i_{1v} are considered as the outputs to be controlled for system (1.21), then the respective Brunowsky form can be obtained applying the following change of coordinates:

$$z_{1u} = i_{1u} + \beta_1 \phi_{2u} \ , \ z_{1v} = i_{1v} + \beta_1 \phi_{2v} \tag{3.3}$$

indeed, it can be verified that the dynamics in (1.21), expressed in the new variables (i_{1u}, i_{1v}, z_{2u}, z_{2v}), read as:

$$\begin{aligned}
\dot{i}_{1u} &= -\gamma_1 i_{1u} + (\omega_0 - \omega_r) i_{1v} + \alpha_2 z_{1u} + \omega_r z_{1v} + \frac{U}{\sigma_1} - \beta_1 u_{2u} \\
\dot{i}_{1v} &= -\gamma_1 i_{1v} - (\omega_0 - \omega_r) i_{1u} + \alpha_2 z_{1v} - \omega_r z_{1u} - \beta_1 u_{2v} \\
\dot{z}_{1u} &= -\frac{R_1}{\sigma_1} i_{1u} + \omega_0 z_{1v} + \frac{U}{\sigma_1} \\
\dot{z}_{1v} &= -\frac{R_1}{\sigma_1} i_{1v} - \omega_0 z_{1u}.
\end{aligned} \tag{3.4}$$

Now, defining the current errors $\tilde{i}_{1u} = i_{1u} - i^*_{1u}$, $\tilde{i}_{1v} = i_{1v} - i^*_{1v}$, with respect to known references i^*_{1u}, i^*_{1v}, it is easy to see that, under perfect tracking (null $\tilde{i}_{1u}$, $\tilde{i}_{1v}$), the corresponding zero dynamics are:

$$\begin{aligned}
\dot{z}_{1u} &= -\frac{R_1}{\sigma_1} i^*_{1u} + \omega_0 z_{1v} + \frac{U}{\sigma_1} \\
\dot{z}_{1v} &= -\frac{R_1}{\sigma_1} i^*_{1v} - \omega_0 z_{1u}.
\end{aligned} \tag{3.5}$$

The above-mentioned ODE presents an LTI, second-order, neutrally stable dynamics exhibiting oscillatory behavior with natural pulsation ω_0. Hence, given stator current trajectories, there exists an infinite set of non converging internal dynamics trajectories ensuring perfect output tracking. It is worth noting that the line voltage U enters the dynamics (3.5) as an exogenous input. Therefore, any perturbation such as voltage sags or swells to the grid point the stator is connected to, would excite the system (3.5) un-damped modes causing permanent oscillations in the internal variables, and the control inputs, as well. But the positive news is that, among infinite the solutions of (3.5), it is possible to find at least one "oscillations free" trajectory, even under line voltage variations. This elaboration will be deeply carried out, in the following, adopting two different methods to analytically solve (3.5).

3.3.2 Normal Brunowsky form with respect to Output Rotor Currents

It is easily clear that the system (1.23) is already in the shape of the Brunowsky canonical form with respect to outputs i_{2u}, i_{2v}, when stator fluxes are the internal variables. In order to keep consistent notation to the previous paragraph, we define:

$$z_{2u} = \phi_{1u} \ , \ z_{2v} = \phi_{1v} \tag{3.6}$$

then, by defining the current errors $\tilde{i}_{2u} = i_{2u} - i^*_{2u}$, $\tilde{i}_{2v} = i_{2v} - i^*_{2v}$, with respect to references i^*_{2u}, i^*_{2v}, and assuming perfect tracking (null $\tilde{i}_{2u}$, $\tilde{i}_{2v}$), the corresponding

zero dynamics are:

$$\begin{aligned}\dot{z}_{2u} &= -\alpha_1 z_{2u} + \omega_0 z_{2v} + \alpha_1 L_m i^*_{2u} + U \\ \dot{z}_{2v} &= -\omega_0 z_{2u} - \alpha_1 z_{2v} + \alpha_1 L_m i^*_{2v}\end{aligned} \tag{3.7}$$

denoting a second order LTI system which is asymptotically stable, due to the damping terms $-\alpha_1$. Thus, in the $i_2 - \phi_1$ framework, the system is minimum phase with respect to output i_{2u}, i_{2v}. Consequently, for given rotor current references, z_{2u}, z_{2v} asymptotically converge to the corresponding unique solution of (3.7). Despite its asymptotic stability, also system (3.7) exhibits oscillatory modes at frequency ω_0 which can be triggered by line voltage faults, since U directly affects dynamics (3.7) as well as (3.5). In view of these considerations, also in this case, a thoughtful analysis of the solutions of (3.7) would be beneficial to directly select the steady-state solution, as a desired trajectory for the internal dynamics. In this way, oscillations caused by the transient response of (3.7) would be avoided. Again, this statements and procedures will be clarified in the following paragraphs devoted to the analytical solution of (3.5)-(3.7).

3.3.3 Explicit solutions of the zero dynamics

The zero dynamics (3.5) is marginally stable, while that in (3.7) is asymptotically stable. Despite this important difference, they are both highly oscillatory. As a matter of fact, DFIGs are designed in order to have very low resistances, then α_1 is usually much smaller than ω_0 in (3.7), leading to poorly damped oscillations, similar to the permanent ones of (3.5). Reasonably, both the oscillations in (3.5) and the ones in (3.7), can lead to problems in complying with constraints mentioned in Section 3.2, while stator or rotor currents perfect tracking is pursued. Therefore, it looks profitable to search for oscillation-free trajectories for both of the above-mentioned zero dynamics, depending on the inputs (i^*_{1u},i^*_{1v},U^*) and (i^*_{2u},i^*_{2v},U), respectively. In this respect, two approaches are presented taking advantage of LTI behavior of both of the zero dynamics. In the first one, Sylvester equation is exploited assuming inputs which are generated by finite integrator chains. In the second one, by parts integration is exploited to extend the previous result to any arbitrary $\mathcal{C}^\infty$ input, and to highlight the oscillatory component of the response that needs to be removed, along with the contribution of each input derivative.

Solution based on Sylvester Equation

Equations (3.5) (3.7) show a similar structure which can be compactly represented as:

$$\dot{z}_i(t) = A_i z_i(t) + B_i u_i(t),\ i = 1, 2 \tag{3.8}$$

where index $i = 1$ refers to $i_1 - \phi_2$ representation, then $z_1 = [z_{1u}\ z_{1v}]^T$, and by (3.5), we have

$$A_1 = \begin{bmatrix} 0 & \omega_0 \\ -\omega_0 & 0 \end{bmatrix},\ B_1 = \begin{bmatrix} -\frac{R_1}{\sigma_1} & 0 & \frac{1}{\sigma_1} \\ 0 & -\frac{R_1}{\sigma_1} & 0 \end{bmatrix},\ u_1(t) = \begin{bmatrix} i_{1u}(t) \\ i_{1v}(t) \\ U(t) \end{bmatrix} \tag{3.9}$$

while index $i = 2$ is referred to the $i_2 - \phi_1$ representation, with $z_2 = [z_{2u}\ z_{2v}]^T$ and

$$A_2 = \begin{bmatrix} -\alpha_1 & \omega_0 \\ -\omega_0 & -\alpha_1 \end{bmatrix},\ B_2 = \begin{bmatrix} \alpha_1 L_m & 0 & 1 \\ 0 & \alpha_1 L_m & 0 \end{bmatrix},\ u_2(t) = \begin{bmatrix} i_{2u}(t) \\ i_{2v}(t) \\ U(t) \end{bmatrix}. \tag{3.10}$$

Now, assuming inputs vectors u_i such that $u_i^{(j)} = 0$, for $j > n$, where $x^{(j)}$ denotes the j^{th} time derivative of x, we can think these class of signals to be generated by the ensuing *exosystems*:

$$u_i(t) = \mathbf{\Gamma}\ w_i(t),\ \dot{w}_i(t) = \mathbf{S} w_i(t),\ i = 1, 2 \tag{3.11}$$

where

$$\begin{aligned} w_1(t) &= [i_{1u}(t)\ \ \dot{i}_{1u}(t)\ \ \ldots\ \ i_{1u}^{(n)}(t)\ \ i_{1v}(t)\ \ \dot{i}_{1v}(t)\ \ \ldots\ \ i_{1v}^{(n)}(t)\ \ U(t)\ \ \dot{U}(t)\ \ \ldots\ \ U^{(n)}(t)]^T \\ w_2(t) &= [i_{2u}(t)\ \ \dot{i}_{2u}(t)\ \ \ldots\ \ i_{2u}^{(n)}(t)\ \ i_{2v}(t)\ \ \dot{i}_{2v}(t)\ \ \ldots\ \ i_{2v}^{(n)}(t)\ \ U(t)\ \ \dot{U}(t)\ \ \ldots\ \ U^{(n)}(t)]^T \end{aligned} \tag{3.12}$$

and

$$\mathbf{\Gamma} = blkdiag(\Gamma_j), \text{with } j = 1, 2, 3 \text{ and } \Gamma_j \in \mathbb{R}^{1\times(n+1)} = \begin{bmatrix} 1 & 0 & \ldots & 0 \end{bmatrix} \forall j$$

$$\mathbf{S} = blkdiag(S_j), \text{with } j = 1, 2, 3 \text{ and } S_j \in \mathbb{R}^{(n+1)\times(n+1)} = \begin{bmatrix} 0 & 1 & 0 & \ldots & 0 \\ 0 & 0 & 1 & \ldots & 0 \\ \vdots & \vdots & \vdots & \vdots & \vdots \\ 0 & \ldots & \ldots & 1 & 0 \\ 0 & \ldots & \ldots & \ldots & 0 \end{bmatrix} \forall j. \tag{3.13}$$

As a result of the previous definitions and assumptions, the steady-state forced response of systems (3.5), (3.7), under the class of inputs generated by dynamics in (3.11), can be expressed as $z_i(t) = \Pi_i w_i(t)$, where matrices Π_i are given by the solution of the ensuing Sylvester equations:

$$\Pi_i\ \mathbf{S} = A_i \Pi + B_i\ \mathbf{\Gamma}, i = 1, 2. \tag{3.14}$$

Since matrices A_i and $\mathbf{S}$ have separated spectra[1] for both the considered cases, there exists a unique solution for Π_i, which can be analytically derived applying recently proposed methods in the related literature [51].

[1] also referred as *non-resonance* condition

By Parts Integrating Solution

The solution of the previous Subsection is restricted to input generated by finite integrator chains with known order n. Now, a generic $\mathcal{C}^\infty$ input is considered. Thanks to LTI property of internal dynamics (3.5) and (3.7), the states $z_{iu}(t)$, $z_{iv}(t)$ (again $i = 1$ is used for $i_1 - \phi_2$, and $i = 2$ for $i_2 - \phi_1$ representations) can be explicitly expressed as:

$$\begin{bmatrix} z_{iu}(t) \\ z_{iv}(t) \end{bmatrix} = \begin{bmatrix} z_{iu}(0) \\ z_{iv}(0) \end{bmatrix} e^{A_i t} + \int_0^t e^{A_i(t-\tau)} f_i(\tau) d\tau \tag{3.15}$$

with

$$f_1(t) = \frac{1}{\sigma_1} \begin{bmatrix} -R_1 i_{1u}(t) + U(t) \\ -R_1 i_{1v}(t) \end{bmatrix}, \quad A_1 = \begin{bmatrix} 0 & \omega_0 \\ -\omega_0 & 0 \end{bmatrix} \tag{3.16}$$

$$f_2(t) = \begin{bmatrix} \alpha_1 L_m i_{2u}(t) + U(t) \\ \alpha_1 L_m i_{2v}(t) \end{bmatrix}, \quad A_2 = \begin{bmatrix} -\alpha_1 & \omega_0 \\ -\omega_0 & -\alpha_1 \end{bmatrix}. \tag{3.17}$$

Integrating (3.15) by parts, we obtain:

$$\begin{bmatrix} z_{iu}(t) \\ z_{iv}(t) \end{bmatrix} = \left(\begin{bmatrix} z_{iu}(0) \\ z_{iv}(0) \end{bmatrix} + A_i^{-1} f_i(0) \right) e^{A_i t} - A_i^{-1} f_i(t) + A_i^{-1} \int_0^t e^{A_i(t-\tau)} f_i^{(1)}(\tau) d\tau \tag{3.18}$$

and, integrating by parts again,

$$\begin{bmatrix} z_{iu}(t) \\ z_{iv}(t) \end{bmatrix} = \left(\begin{bmatrix} z_{iu}(0) \\ z_{iv}(0) \end{bmatrix} + A_i^{-1} f_i(0) + A_i^{-2} f_i^{(1)}(0) \right) e^{A_i t} + \left(-A_i^{-1} f_i(t) - A_i^{-2} f_i^{(1)}(t) \right) + \\ + A_i^{-3} \int_0^t e^{A_i(t-\tau)} f_i^{(2)}(\tau) d\tau \tag{3.19}$$

keeping to apply the procedure iteratively yields:

$$\begin{bmatrix} z_{iu}(t) \\ z_{iv}(t) \end{bmatrix} = \left(\begin{bmatrix} z_{iu}(0) \\ z_{iv}(0) \end{bmatrix} + \sum_{k=0}^{\infty} A_i^{-(k+1)} f_i^{(k)}(0) \right) e^{A_i t} - \left(\sum_{k=0}^{\infty} A_i^{-(k+1)} f_i^{(k)}(t) \right). \tag{3.20}$$

Looking at (3.20), it can be noted how the oscillatory part, given by the zero dynamics free response combined with the transient part of the forced response, can be canceled out by means of the following selection of the initial conditions $z_{iu}^*(0)$, $z_{iv}^*(0)$:

$$\begin{bmatrix} z_{iu}^*(0) \\ z_{iv}^*(0) \end{bmatrix} = -\sum_{k=0}^{\infty} A_i^{-(k+1)} f_i^{(k)}(0). \tag{3.21}$$

Equivalently, we can state that an internal dynamics trajectory (z_{iu}^*,z_{iv}^*) avoiding oscillations, is given by the remainder, not oscillatory terms of (3.20) obtained replacing $z_{iu}(0)$, $z_{iv}(0)$ with $z_{iu}^*(0)$, $z_{iv}^*(0)$ as in (3.21), namely:

$$\begin{bmatrix} z_{iu}^*(t) \\ z_{iu}^*(t) \end{bmatrix} = \sum_{k=0}^{\infty} A_i^{-(k+1)} f_i^{(k)}(t) \tag{3.22}$$

If $f_i^{(k)}(t)$ is assumed to be identically null for each $k > n$, the relation (3.22) recovers exactly the result derived in Subsection 3.3.3 by means of Sylvester equations. Therefore, (3.22) can be effectively adopted to represent analytically the oscillation-free trajectories, $z_i(t) = \Pi_i w_i(t)$, for any input having an arbitrarily large number of non null derivatives[2].

In view of these considerations, in order to operatively exploit (3.22), it looks reasonable to approximate the current references and the line voltage U with signals which are assumed bounded, $\mathcal{C}^{n-1}$ and with piece-wise constant n-th derivatives (i.e. the higher order derivatives are assumed null along time, except for the isolated points where jumps in n-th derivatives of the inputs are taking place). For the sake of simplicity, without loss of generality, in the reminder of this chapter, bounded, $\mathcal{C}^0$ and piece-wise linear signals will be adopted to represent current references and line voltage[3]. Therefore, the following oscillation-free trajectories can be derived, exploiting (3.22), for the zero dynamics of the $i_1 - \phi_2$, and $i_2 - \phi_1$ model representations, where stator and rotor currents are assumed as outputs, respectively:

$$\begin{aligned} z_{1u}^*(t) &= -\frac{R_1}{\sigma_1\omega_0} i_{1v}^* - \frac{R_1}{\sigma_1\omega_0^2}\dot{i}_{1u}^* + \frac{\dot{U}}{\sigma_1\omega_0^2} \\ z_{1v}^*(t) &= -\frac{U}{\sigma_1\omega_0} + \frac{R_1}{\sigma_1\omega_0} i_{1u}^* - \frac{R_1}{\sigma_1\omega_0^2}\dot{i}_{1v}^* \end{aligned} \tag{3.23}$$

$$\begin{aligned} z_{2u}^*(t) &= \frac{\alpha_1^2 L_m}{M} i_{2u}^* + \frac{\alpha_1\omega_0 L_m}{M} i_{2v}^* + \frac{\alpha_1}{M} U - \frac{N\alpha_1 L_m}{M^2}\dot{i}_{2u}^* - \frac{2\alpha_1^2\omega_0 L_m}{M^2}\dot{i}_{2v}^* - \frac{N}{M^2}\dot{U} \\ z_{2v}^*(t) &= -\frac{\alpha_1\omega_0 L_m}{M} i_{2u}^* + \frac{\alpha_1^2 L_m}{M} i_{2v}^* - \frac{\omega_0}{M} U + \frac{2\alpha_1^2\omega_0 L_m}{M^2}\dot{i}_{2u}^* - \frac{N\alpha_1 L_m}{M^2}\dot{i}_{2v}^* + \frac{2\alpha_1\omega_0}{M^2}\dot{U} \end{aligned} \tag{3.24}$$

where $M = \alpha_1^2 + \omega_0^2$ and $N = \alpha_1^2 - \omega_0^2$. It is worth noting that, in order to compute the above trajectories $\dot{U}$ is needed. In practice, it can be estimated by suitable line voltage observers [52], since it is not the main focus of the work, this issue is not elaborated here. In summary, in this Section, we illustrated how to build the trajectories for the full state (starting from given references for just two out of four states) preventing the oscillations characterizing the DFIM dynamics, even under line voltage fluctuations (since U and its derivatives are explicitly accounted). This result is expected to be profitable to deal with objectives and constraints reported in

[2]the case of $\mathcal{C}^\infty$ inputs with infinite non-null derivatives could be operatively managed only under some conditions guaranteeing convergence and explicit computability of the infinite summation in (3.22). In addition, the result above provides useful insights on how the derivatives of different orders of the inputs (i.e. stator or rotor currents and line voltage) are affecting the zero-dynamics oscillation-free trajectories. In fact, by (3.16), (3.17), (3.22), it can be noted how the k^{th} order current and line voltage derivatives are weighted with a factor $(1/\omega_0)^{k+1}$, which rapidly vanishes for increasing order k (since the line angular frequency is $\omega_0 = 2\pi 50 rad/s$ or $\omega_0 = 2\pi 60 rad/s$)

[3]clearly, the considered smoothness properties for the current references are also consistent with the relative degree of the system, in order to enable the possibility to achieve perfect tracking

Section 3.2. In particular, to manage correctly the rotor control voltage saturation and to avoid rotor overcurrents and violations of magnetic flux saturation limits.
In this respect, it it crucial noting that, whenever an arbitrary jump occurs in the piece-wise constant derivatives of current references or line voltage, the oscillation-free trajectories defined in (3.23) and (3.24), will have a jump, as well, but directly in the state variables (z_{1u}, z_{1v}) or (z_{2u}, z_{2v}). Clearly, this observation applies in the same way to the general case of any input $f_i(t)$ in (3.22) having null derivatives for any order larger than a given one. Therefore, structurally, no even $\mathcal{C}^0$ blending can be imposed between the oscillation-free zero dynamics trajectories corresponding to two subsequent stretches of current references and line voltage signals, even if they are characterized by an arbitrarily smooth blending (i.e. a $\mathcal{C}^{n-1}$ blending with a given jump in the n-th derivative and arbitrarily large n). Hence, whenever an arbitrary derivative change occurs in the current references or in the line voltage, oscillations in the zero dynamics and/or errors in the reference tracking can unavoidably arise, whatever the adopted controller is, and regardless of how large the order of the changed derivatives is, because no smoothness in the oscillation-free zero dynamics trajectories can be guaranteed[4]. However, even if, structurally, any controller cannot guarantee perfect tracking along with no oscillations in the zero dynamics, amplitudes of arising tracking errors and/or zero dynamics oscillations will be shaped by the features of the adopted controller. Therefore, even if the proposed oscillation-free trajectories can be reasonably expected to help in dealing with the control objective and constraints, the role of the adopted feedback controller will be crucial, as well. In the previous Section, it has been shown that the internal zero dynamics for the rotor currents (selected as output variables) are asymptotically stable, while for the stator currents, just non-converging, marginally stable zero dynamics have been obtained. Therefore, it seems profitable to arrange a feedback linearizing control considering rotor currents as controlled outputs. This would allow to naturally deal with rotor current constraints mentioned in item (1) of the list in Section 3.2. While, as concerns the internal variables (stator fluxes), thanks to the minimum phase property, it is not necessary to take care about them explicitly, as the steady state bounded (for bounded references) and not oscillating trajectories computed in (3.24) of Section 3.3 will be asymptotically reached. Therefore, according to the considerations in the end of Section 3.3, it can be underlined that the feedback linearizing control will react to steps in the first derivative of the rotor

[4]these considerations are carried out assuming arbitrary and fixed changes in one of the derivatives of current references and line voltage; clearly, if some of such derivatives' jumps can be adjusted, resetting or, at least, reduction of the jumps in the oscillation-free zero dynamics can be possible (in particular, for reduction purposes, shifting the changing to higher order derivatives can be profitable owing to the lower effect of such terms in (3.22), as previously discussed).

current references or in the line voltage using the rotor control voltage to preserve null tracking error, while poorly damped oscillations in the zero dynamics will take place.
Actually, all of these considerations hold true only in terms of unconstrained stabilization. Indeed, here we show how the aforementioned good theoretical properties are completely lost when line voltage perturbations, along with states and control inputs limitation stemming from the machine physical bounds, are considered. First, a standard feedback linearizing control solution is formulated disregarding the constraints, then it is tested via numerical simulations of a benchmark DFIM under realistic grid faults.

3.4 Feedback linearizing control definition

The DFIM control problem described in Section 3.2 can be briefly formulated as follows: ensure asymptotic rotor current references tracking, and boundedness of all the internal signals, also in face of line voltage perturbations.
Looking at the system dynamics (1.23), and recalling (3.6), the following state feedback, input-output linearizing control law can be used to guarantee asymptotic tracking of (bounded) arbitrary $\mathcal{C}^0$ and piece-wise linear current references i_{2u}^*, i_{2v}^* with known first order time derivatives $\dot{i}_{2u}^*$, $\dot{i}_{2v}^*$:

$$\begin{aligned} u_{2u} =& \sigma_2 \Big(\gamma_2 i_{2u}^* + \dot{i}_{2u}^* - (\omega_0 - \omega_r) i_{2v}^* - \beta_2 \alpha_1 z_{2u} + \beta_2 \omega_r z_{2v} + \beta_2 U + v_{2u} \Big) \\ u_{2v} =& \sigma_2 \Big((\omega_0 - \omega_r) i_{2u}^* + \gamma_2 i_{2v}^* + \dot{i}_{2v}^* - \beta_2 \omega_r z_{2u} - \beta_2 \alpha_1 z_{2v} + v_{2v} \Big). \end{aligned} \tag{3.25}$$

According to what stated at the end of Section 3.2, the machine parameters, line voltage amplitude and angular frequency, stator fluxes and rotor currents, speed and position, have been used to implement the law above. Variables v_{2u}, v_{2v} denote auxiliary output feedback terms to be possibly used for tuning the convergence rate and endow the controller with robustness against parametric uncertainties and measurements errors. Note that, despite stator fluxes are typically not directly available from measurements, while stator currents are usually acquired, still z_{2u}, z_{2v} can be retrieved by expressing ϕ_{1u}, ϕ_{1v} as a function of the stator and rotor currents [53] obtaining the relations: $z_{2u} = L_1 i_{1u} + L_m i_{2u}$, $z_{2v} = L_1 i_{1v} + L_m i_{2v}$.
By the analysis carried out in Section 3.3, we know the corresponding zero dynamics are given by the asymptotically stable LTI system (3.7). Thus, from a theoretical viewpoint, the feedback linearizing strategy (3.25) solves the output tracking problem, as, for limited current references, the solutions of (3.7), and in turn the stator fluxes and the control inputs u_{2u}, u_{2v} are always bounded. However, as mentioned in

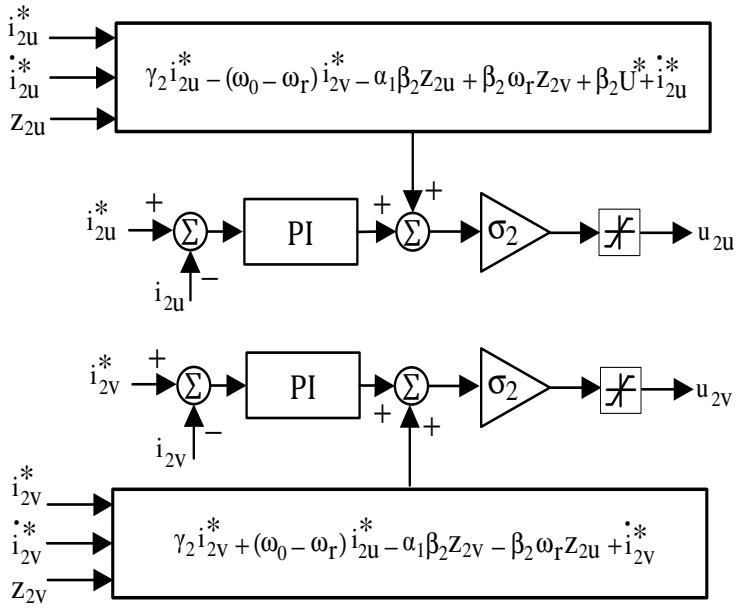

Figure 3.2: Schematic diagram of the feedback linearizing controller.

Subsection 3.3.2, under line voltage faults, the oscillatory modes of the zero dynamics (3.7) would be triggered. As a result, oscillations would also arise in the control inputs (rotor voltages). Theoretically, this is not an issue, as these oscillations will asymptotically vanish in view of the system minimum phase property. However, under severe grid faults, the machine physical limits are likely to be reached/violated and, if not properly handled, make the DFIM disconnected for protection (e.g. overcurrent at rotor side). Thus, the system would fail to properly ride thorough line voltage off-nominal conditions, impairing its reliability and availability.
In next Subsection, the aforementioned considerations will be substantiated by means of significant simulations.

3.4.1 Simulations results with state feedback linearizing control strategy

The control law (3.25) (whose block scheme is reported in Fig. 3.2) has been applied to a 0.5MW 50 Hz DFIG characterized by the parameters reported in Tab. A.1. Machine operation as a generator has been simulated, under constant rotational speed equal to $150 rad/s$, that corresponds to $\omega_r = 300 rad/s$, since the considered DFIG has 2 pole pairs. A three-phase symmetric fault, causing voltage drop in the grid, has been reproduced to underscore its sensitivity to such kind of events. As shown in Fig. 2.1 in the previous chapter, a typical power systems voltage dip consists of three different stages: voltage falling, voltage stabilizing, and voltage recovering [33]. In the following simulations tests, such shape is approximated by a

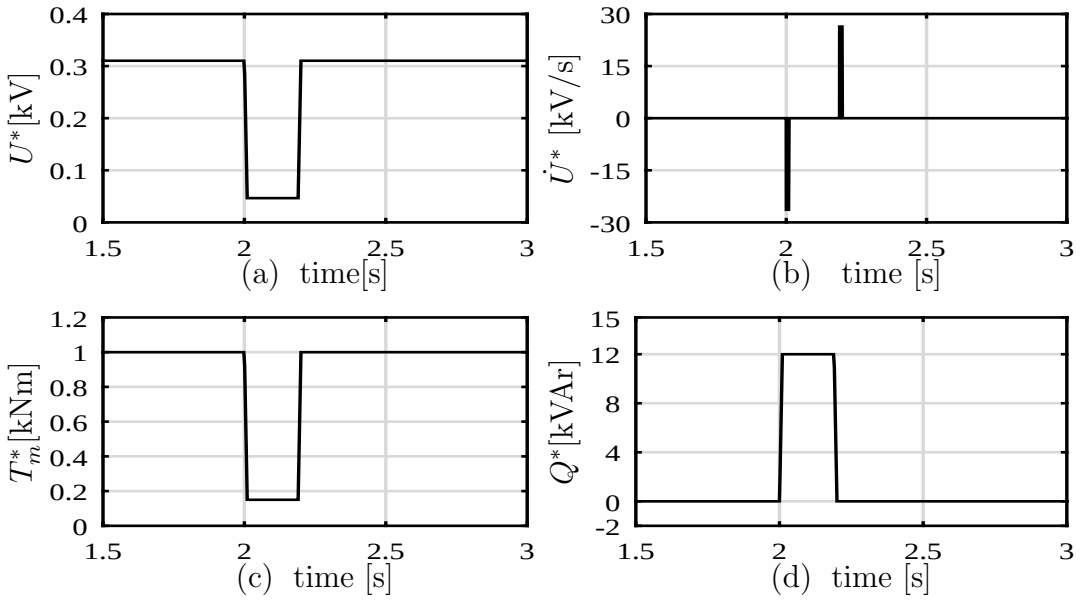

Figure 3.3: Transient results for the studied system equipped with standard feedback linearizing controller at 85% line voltage dip. (a) Stator voltage. (b) First derivative of the stator voltage. (c) Reference torque. (d) Stator-side reference reactive power.

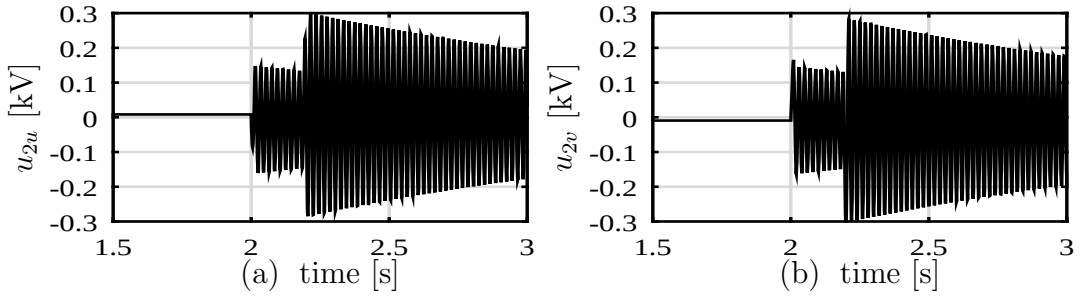

Figure 3.4: Transient results for the studied system equipped with standard feedback linearizing controller at 85% line voltage dip. (a) Rotor u-component control voltage. (b) Rotor v-component control voltage.

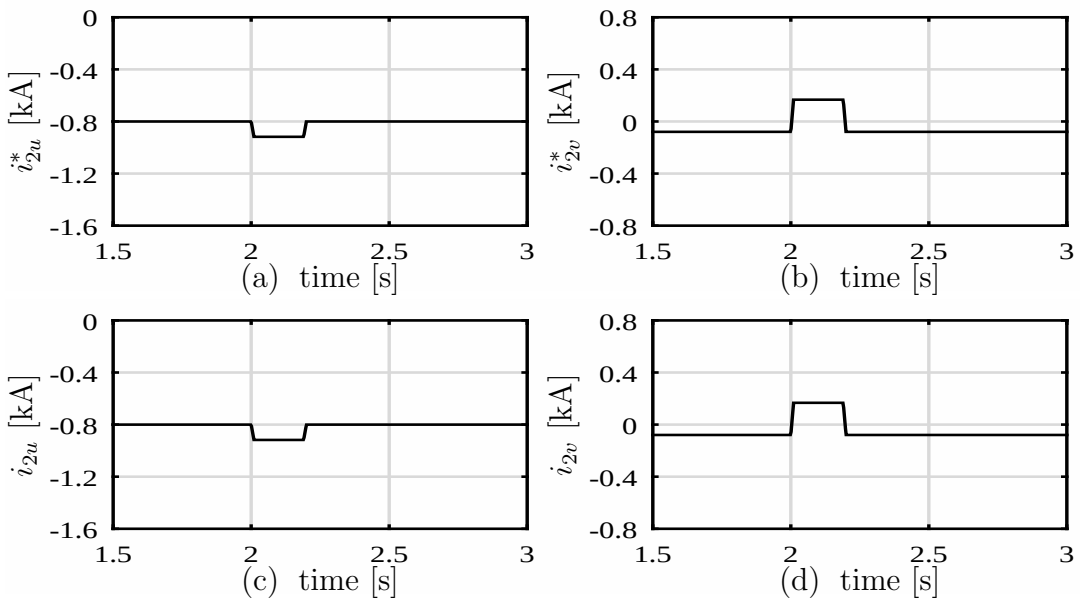

Figure 3.5: Transient results for the studied system equipped with standard feedback linearizing controller at 85% line voltage dip. (a) Rotor u-component reference current. (b) Rotor v-component reference current. (c) Rotor u-component current. (d) Rotor v-component current.

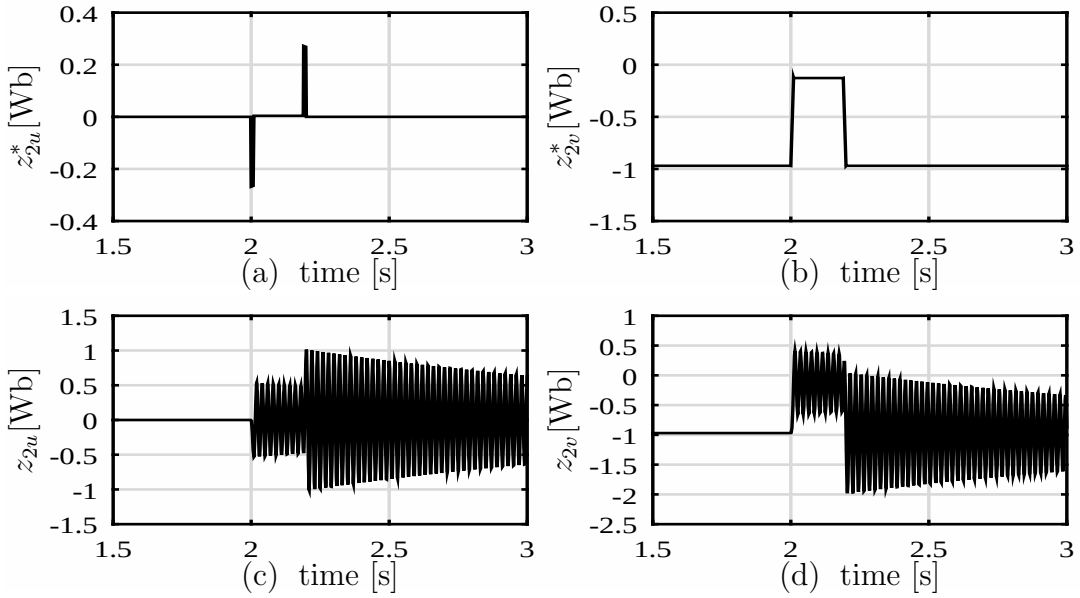

Figure 3.6: Transient results for the studied system equipped with standard feedback linearizing controller at 85% line voltage dip. (a) Zero dynamics (stator magnetic flux) u-component reference. (b) Zero dynamics (stator magnetic flux) v-component reference. (c) Zero dynamics (stator magnetic flux) u-component. (d) Zero dynamics (stator magnetic flux) v-component.

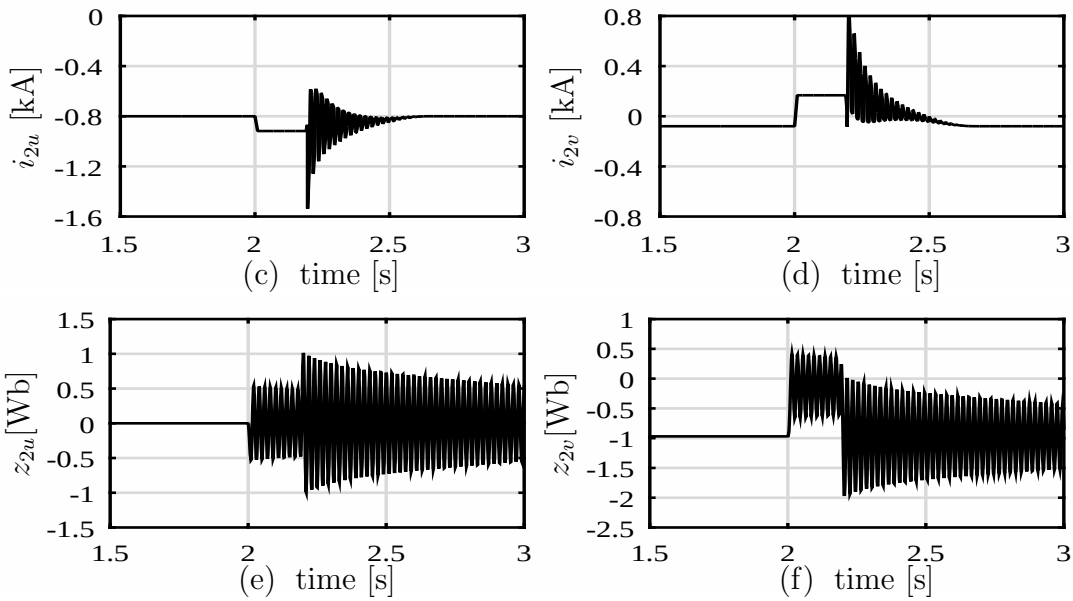

Figure 3.7: Transient results for the studied system equipped with saturated standard feedback linearizing controller under 85% line voltage dip. (a) Rotor u-component control voltage. (b) Rotor v-component control voltage. (c) Rotor u-component current. (d) Rotor v-component current. (e) Zero dynamics (stator magnetic flux) u-component. (f) Zero dynamics (stator magnetic flux) v-component.

trapezoid emulating a 85% voltage amplitude reduction with respect to the nominal value, lasting $180ms$, with $10ms$ for both falling and recovering stages. To a certain extent, this approximation represent real voltage sag profiles closely enough to asses the system behavior and the controller performance in low line voltage conditions. Under nominal conditions, reference values corresponding to constant torque $T_m^* = 1kNm$ and null reactive power $Q^* = 0$, and the respective rotor current references i_{2u}^*, i_{2v}^* have been set. When the voltage sag occurs, the references are changed as follows: T_m^* is reduced according to the dip shape, while Q^* is increased in order to inject capacitive reactive power into the mains, as required for generators under low line voltage conditions in order to sustain the grid voltage [18], [16] (see Figs.3.7 (c)-(d), (h)-(g)). Obviously, i_{2u}^*, i_{2v}^* are moved accordingly. For what concerns the terms v_{2u}, v_{2v}, the following PI regulators have been implemented:

$$\begin{aligned} v_{2u} &= k_i\tilde{i}_d + \lambda\tilde{i}_q - y_{2u},\ \dot{y}_{2u} = -k_{ii}\tilde{i}_{2u} + \lambda\frac{R_1}{\sigma_1}\tilde{i}_{2v} \\ v_{2v} &= k_i\tilde{i}_q - \lambda\tilde{i}_d - y_{2v},\ \dot{y}_{2v} = -k_{ii}\tilde{i}_{2v} - \lambda\frac{R_1}{\sigma_1}\tilde{i}_{2u} \end{aligned} \tag{3.26}$$

with $\lambda = k_{ii}\omega_0^{-1}$ and k_i, k_{ii} arbitrary positive gains. The values selected for the simulations are $k_i = 300$, $k_{ii} = 5458$, and $\lambda = 17.37$.

Simulation results for an ideal unconstrained DFIM are reported in Figs. 3.3-3.6. Rotor currents tracking is always ensured, also under the voltage sag occurring at $t = 2sec.$ (see Figs. 3.5), and the internal variables naturally tend to converge to the steady-state solutions z_{2u}^*, z_{2v}^* derived in (3.24) (see Figs. 3.6). However, large oscillations arise in the rotor voltages (Figs. 3.4), which make the control effort to exceed, by far, the rated value reported in Tab. A.1 ($265V_{RMS}$ line voltage, which corresponds[5] to $216.3V_{peak}$ phase voltage)

When such constraints are enforced by means of saturation nonlinearity for both rotor voltages u_{2u}, u_{2v}, the performance of the feedback linearization approach are significantly impaired, as shown in Fig. 3.7. As expected, during the dip, the control input saturation bounds are hit (see Fig. 3.7 (a)-(b)). In turn, the current tracking is lost during the grid perturbation, and a high current spikes (as portrayed in Figs. 3.7 (c)-(d)) arises, exceeding the rated value reported in Tab. A.1 ($780A_{RMS}$ which corresponds to $1103A_{peak}$). Then, even if current errors are steered back to zero, when nominal conditions are restored, on a real system, the DFIM would have been switched off, disconnected, or some protection mechanism (e.g. a crowbar) would have been triggered to protect it from overcurrent during the dip. Even if under less harsh faults the rotor currents could be kept within the ratings, still large oscillations would affect the torque as well, possibly exciting the mechanical resonance of what connected to the rotor. Similar reasoning applies for the stator fluxes (Figs. 3.7

[5]note that all the values are reported to stator-side both in Tab.A.1 and in simulations

(e)-(f)), which, despite tending to recover constant steady-state values, thank to the minimum phase property, have considerable oscillations during the dip.
In the above tests, a symmetric voltage dip has been simulated by a piece-wise linear profile, hence the oscillations in the internal dynamics look mainly related to the steps in the first order derivative of such variable. Actual voltage dips can have no sudden jump in the first derivative, but, according to application oriented literature they have very sharp and abrupt changes, as well, and even more involved shape as shown in Fig.2.1, therefore the presented results are representative of what can be expected in a real plant. Due to the issues illustrated above, DFIM control cannot be cast as a standard output tracking problem, solved by feedback linearization. Control input saturation has to be considered explicitly and countermeasures need to be taken to dampen rotor currents oscillations along with the internal variables, under line voltage perturbations in order to preserve a graceful behavior of the DFIM.
In this respect, the next Section is devoted to present a novel control strategy based on suitable zero dynamics trajectory planning, derived from the oscillation-free trajectories defined in Section 3.3, and saturated state feedback design.

3.5 Proposed feedforward-feedback control solution

In the previous Section, based on the simulation results, we have shown how the feedback linearizing control approach, while reasonable from a general control viewpoint, cannot be used when practical line faulty voltage scenarios, and DFIM physical limitations are considered. Indeed, the control effort is put solely on keeping rotor current perfect tracking neglecting rotor fluxes and voltages oscillations. The latter has been shown to possibly exeed the RSC voltage rating. Moreover, if the RSC voltage saturation is enforced abruptly in the feedback linearizing controller, overcurrents are generated[6]. Thus, according to the mentioned physical constraints for the state variables of the system in Section 3.2, the control effort should be shared and balanced somehow to take care of the both state-variable groups of stator and rotor. Therefore, in this Section, by proposing a feedforward-feedback control strategy relying on the analysis of the zero dynamics solutions carried out in Subsection3.3.3, we want to regulate all the state variables not only to ensure output tracking under nominal working conditions, but also to satisfy all the corresponding constraints (avoiding excessive oscillation in the system internal states dynamics as

[6]in simulations of Fig.3.7, no antiwindup mechanism was adopted for the PI used in (3.26), but this is not the cause of excessive rotor current spikes

well as output state variables), under line voltage perturbations. A pure open-loop solution, based on the zero dynamics analysis carried out in Section 3.3 is shown first, then it is combined with a state feedback part specifically devoted to limit oscillations under voltage dips, and to explicitly handle control input saturation nonlinearity.

3.5.1 Feedforward control based on zero dynamics trajectories planning

Here, the main idea is to improve the system response under line voltage dips, by exploiting, for control purposes, the oscillation-free internal dynamics trajectories, computed in Subsection 3.3.3, as reference trajectories, planned according to the rotor current references. To this aim, the following open-loop control law is proposed:

$$\begin{aligned} u_{2u} &= \sigma_2 \left(\gamma_2 i^*_{2u} - (\omega_0 - \omega_r) i^*_{2v} - \alpha_1 \beta_2 z^*_{2u} + \beta_2 \omega_r z^*_{2v} + \beta_2 U + \dot{i}^*_{2u} \right) \\ u_{2v} &= \sigma_2 \left(\gamma_2 i^*_{2v} + (\omega_0 - \omega_r) i^*_{2u} - \alpha_1 \beta_2 z^*_{2v} - \beta_2 \omega_r z^*_{2u} + \dot{i}^*_{2v} \right) \end{aligned} \tag{3.27}$$

with z^*_{2u}, z^*_{2v} defined according to (3.24). Taking advantage of the DFIM inherent properties, as highlighted in [41], global asymptotic tracking can be shown to be ensured by the controller (3.27). A sketch of the proof for this result is elaborated in the following.

Proof Replacing (3.27) into (1.23), recalling (3.6), and defining $\tilde{z}_{2u} = z_{2u} - z^*_{2u}$, $\tilde{z}_{2v} = z_{2v} - z^*_{2v}$, the following error dynamics are obtained:

$$\begin{aligned} \dot{\tilde{z}}_{2u} &= -\alpha_1 \tilde{z}_{2u} + \omega_0 \tilde{z}_{2v} + \alpha_1 L_m \tilde{i}_{2u} \\ \dot{\tilde{z}}_{2v} &= -\alpha_1 \tilde{z}_{2v} - \omega_0 \tilde{z}_{2u} + \alpha_1 L_m \tilde{i}_{2v} \\ \dot{\tilde{i}}_{2u} &= -\gamma_2 \tilde{i}_{2u} + \alpha_1 \beta_2 \tilde{z}_{2u} - \beta_2 \omega_r \tilde{z}_{2v} \\ \dot{\tilde{i}}_{2v} &= -\gamma_2 \tilde{i}_{2v} + \alpha_1 \beta_2 \tilde{z}_{2v} + \beta_2 \omega_r \tilde{z}_{2u}. \end{aligned} \tag{3.28}$$

Now, by defining the following Lyapunov candidate

$$V = \frac{1}{2} \left[\tilde{z}^2_{2u} + \tilde{z}^2_{2v} + 2\eta(\tilde{z}_{2u}\tilde{i}_{2u} + \tilde{z}_{2v}\tilde{i}_{2v}) + \frac{\eta}{\beta_2}(\tilde{i}^2_{2u} + \tilde{i}^2_{2v}) \right]$$

the corresponding time derivative along the system (3.28) is:

$$\dot{V} = -\alpha_1(1 - \eta\beta_2)(\tilde{z}^2_{2u} + \tilde{z}^2_{2v}) + (\alpha_1 L_m - \eta\gamma_1)(\tilde{z}_{2u}\tilde{i}_{2u} + \tilde{z}_{2v}\tilde{i}_{2v}) - \frac{\eta}{\beta_2}\frac{R_2}{\sigma_2}(\tilde{i}^2_{2u}\tilde{i}^2_{2v}).$$

Then, it can be verified that there exists $\eta < \frac{1}{\beta_2}$ which makes V positive definite and $\dot{V} < 0$. Therefore, the origin is a globally asymptotically stable equilibrium point for the system (3.28).

Clearly, the above result is instrumental to deal effectively with bounded, $\mathcal{C}^0$, piecewise linear rotor current references and line voltage, since for any stretch of the references and the line voltage with constant derivatives, the system is going to converge toward the desired output trajectory, combined with the corresponding oscillation free internal dynamics trajectory.

3.5.2 Simulation results with open-loop control based on zero dynamics trajectories planning

The open-loop approach based on zero dynamics trajectory planning has been tested under the same simulation scenarios introduced in Section 3.4. The results are shown in Figs.3.8 and 3.9 . As expected, according to the discussion reported at the end of Section 3.3, during the line fault, oscillations in all the state variables are triggered, due to the lack of smoothness U, i_{2u}^* i_{2v}^*, all with discontinuous first time derivatives which, by (3.7), are directly reflected into jumps in z_{2u}^*, z_{2v}^* trajectories (see Figs. 3.9 (a)-(b)). Looking at Figs. 3.8 (c),(d), it can be seen how considerable oscillations, still overcoming the rated peak values (at least for the u component) in Tab. A.1, arise in the rotor currents. On the other hand, looking at stator flux waveforms in Figs. 3.9 (a)-(b), and comparing with those in Figs. 3.6 (a)-(b), it can be noticed a strong reduction in the oscillations amplitude. Therefore, the open-loop solution, based on suitable zero dynamics trajectories, accomplish the task of distributing the oscillations among all the four state variables, rather then taking care only of the outputs, while letting the internal signals completely free to move. Furthermore, the resulting control input are, as expected, free from oscillations, and within the saturation bounds (see Figs. 3.8 (a)-(b)). Then, it looks profitable to build on such positive features, joining some additional terms to the to the feedforward in (3.27), with the purpose of curtailing the states oscillations (in particular the rotor currents), given the limited control effort. To this end, in the following a saturated state feedback will be proposed, casting its design for oscillations minimization into a convex optimization problem.

3.5.3 LMI-based saturated state feedback design

In order to improve the performance of the proposed controller under voltage sags, the control law (3.27) is modified as:

$$\begin{aligned} u_{2u} &= \underbrace{\sigma_2\left(\gamma_2 i_{2u}^* - (\omega_0-\omega_r) i_{2v}^* - \alpha_1\beta_2 z_{2u}^* + \beta_2\omega_r z_{2v}^* + \beta_2 U + \dot{i}_{2u}^*\right)}_{u_{2uff}} + v_u \\ u_{2v} &= \underbrace{\sigma_2\left(\gamma_2 i_{2v}^* + (\omega_0-\omega_r) i_{2u}^* - \alpha_1\beta_2 z_{2v}^* - \beta_2\omega_r z_{2u}^* + \dot{i}_{2v}^*\right)}_{u_{2vff}} + v_v \end{aligned} \tag{3.29}$$

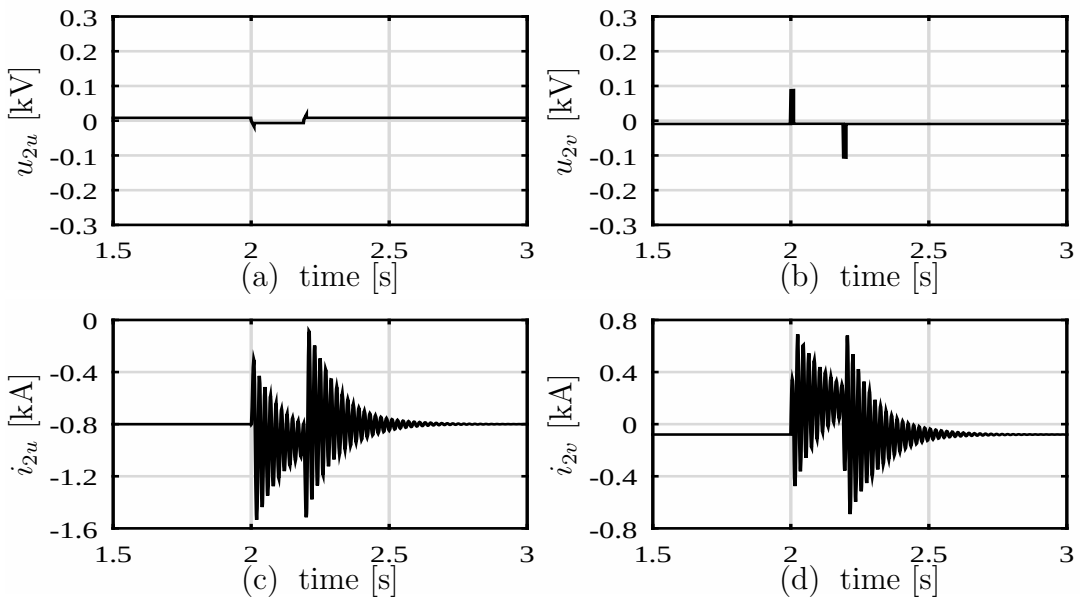

Figure 3.8: Transient results for the studied system equipped with open-loop current controller, based on zero dynamics trajectory planning at 85% line voltage dip. (a) Rotor u-component control voltage. (b) Rotor v-component control voltage. (c) Rotor u-component current. (d) Rotor v-component current.

with v_u, v_v two state feedback terms to be defined in order to dampen oscillations and comply with the system physical saturations. In this respect, a static linear feedback law will be sought, and the corresponding constraints, given by the RSC limits, will be accounted considering a *decentralized vector saturation* function, i.e. a vector of scalar symmetric saturations. The reason for such choice of the feedback structure is to keep a reasonable complexity (also in terms of computational burden) for the overall controller. Furthermore, in case of linear laws, an optimal design procedure (with respect to the required specifications), directly accounting for saturation, can be carried out by formulating a convex optimization problem with LMI constraints. These constraints can be efficiently (in polynomial time) solved with reliable, low complexity numerical algorithms. Finally, beside some degree of conservatism added by such assumption, it is possible to obtain relevant results satisfying the desired objectives. All these features will be clarified in the ensuing discussion, as well as in the next Subsection, where the design method, and simulation results concerning the considered DFIM control problem are respectively reported.
Bearing in mind the previous reasoning, the form for the saturated feedback control is:

$$v = \sigma(p) = \begin{bmatrix} sat(p_u) \\ sat(p_v) \end{bmatrix}, \; p = K\tilde{x} \tag{3.30}$$

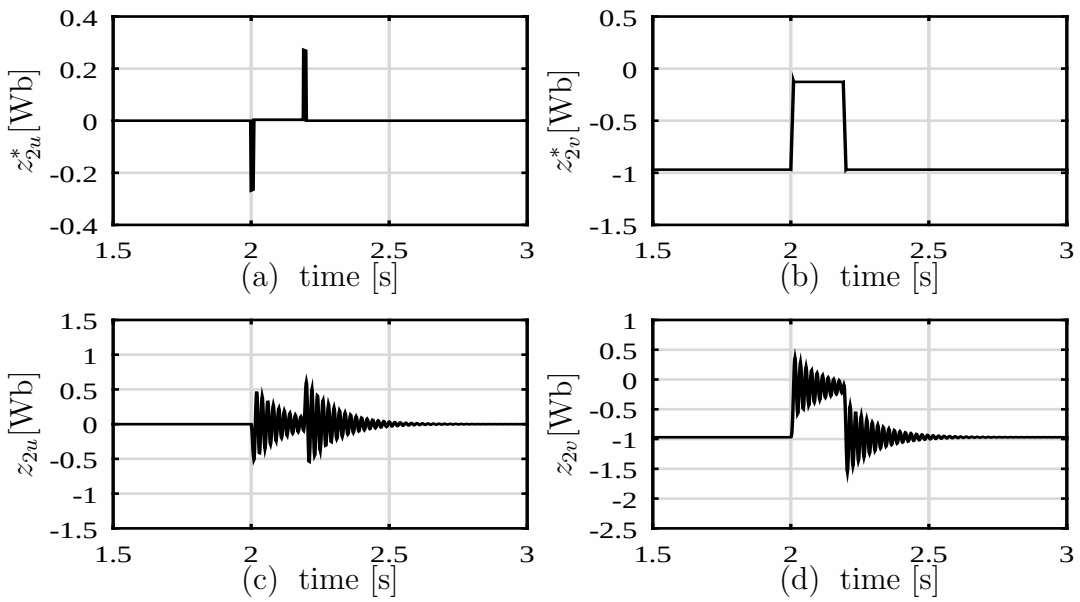

Figure 3.9: Transient results for the studied system equipped with open-loop current controller, based on zero dynamics trajectory planning at 85% line voltage dip. (a) Zero dynamics (stator magnetic flux) u-component reference. (b) Zero dynamics (stator magnetic flux) v-component reference. (c) Zero dynamics (stator magnetic flux) u-component. (d) Zero dynamics (stator magnetic flux) v-component.

where:
$\tilde{x} = [\tilde{z}_{2u}\ \tilde{z}_{2v}\ \tilde{i}_{2u}\ \tilde{i}_{2v}]^T$, $v = [v_u\ v_v]^T$, and $sat(p_j) = (sgn(p_j))(\min\{v_{jmax}, |p_j|)\})$, $j = u, v$. The bounds for v_u, v_v clearly depend on the machine maximum rotor voltages u_{2umax}, u_{2vmax}, stemming from RSC rated voltage and the control effort which is devoted to the feedforward terms u_{2uff}, u_{2vff} underscored in (3.29). The latter is in general varying with the operating conditions. However, assuming some previous knowledge about the system possible trajectories, a safe constant margin can be preserved for terms u_{2uff}, u_{2vff}, and, as a consequence, define constant limits $v_{jmax} = u_{2jmax} - u_{2jffmax}$, $j = u, v$.
The error dynamics under the controller defined by (3.29) and (3.30), can be expressed as:

$$\dot{\tilde{x}} = F(t)\tilde{x} + G\sigma(K\tilde{x}), \text{ with}$$

$$F(t) = \begin{bmatrix} -\alpha_1 & \omega_0 & \alpha_1 L_m & 0 \\ -\omega_0 & -\alpha_1 & 0 & \alpha_1 L_m \\ \alpha_1\beta_2 & -\beta_2\omega_r(t) & -\gamma_2 & \omega_0 - \omega_r(t) \\ \beta_2\omega_r(t) & \alpha_1\beta_2 & \omega_r(t) - \omega_0 & -\gamma_2 \end{bmatrix}, \quad G = \begin{bmatrix} 0 & 0 \\ 0 & 0 \\ -\frac{1}{\sigma_2} & 0 \\ 0 & -\frac{1}{\sigma_2} \end{bmatrix}. \tag{3.31}$$

In the following, the main goal is to design the state-feedback matrix K in order to bound, as much as possible, the oscillations induced during voltage dips owing to

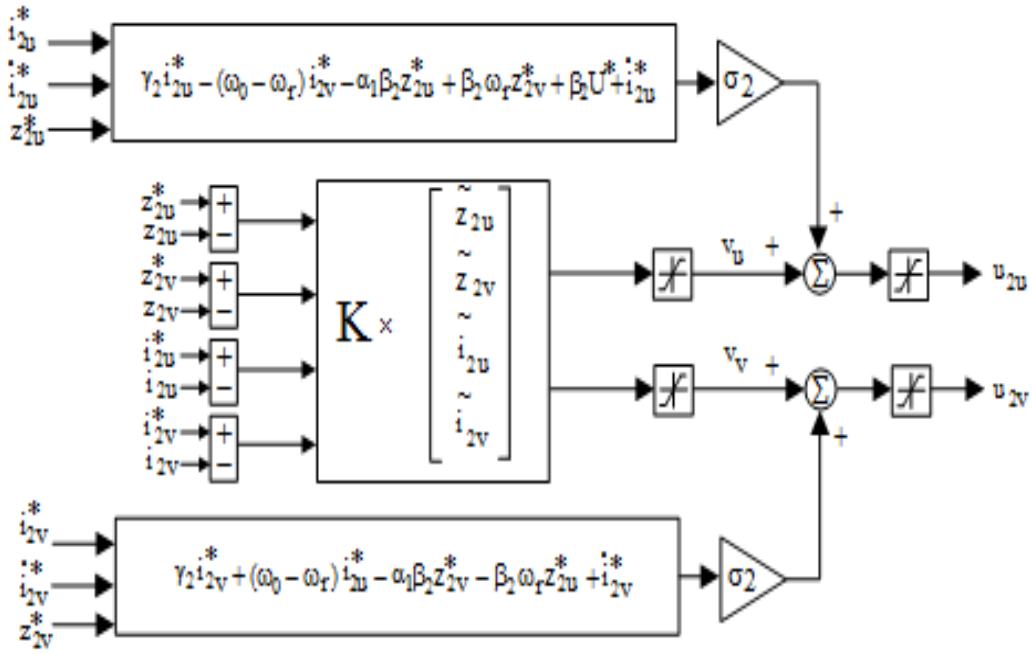

Figure 3.10: Schematic diagram of the proposed feedforward-feedback control solution.

the discontinuities in the zero dynamics reference trajectories z_{2u}^*, z_{2v}^* (as discussed in Subsection 3.3.3).

This objective has to be achieved for all the rotor speed values belonging to the machine nominal range, and explicitly handling constraints on the feedback control effort (accounted via the saturation function $\sigma(\cdot)$ in (3.31)). In this respect, a robust solution with respect to rotor speed variation will be sought considering the following inclusion $F(t) \in \text{co}\{F_{min}, F_{max}\}$, where F_{min}, F_{max} denote the matrix F in (3.31) evaluated at the speed nominal range extreme values ω_{rmin}, ω_{rmax}, respectively, while co indicates the convex hull of the matrices between braces. Then, system (3.31), can be represented by the following differential inclusion:

$$\dot{\tilde{x}} \in \text{co}\{F_{min}, F_{max}\}\,\tilde{x} + G\sigma(K\tilde{x}). \tag{3.32}$$

The next step is to manage the saturation nonlinearity. In this respect, several approaches have been proposed in the literature. Here, we exploit the following property (Lemma 7.3.2 in [54]), extending the classical multivariable circle criterion and vertex analysis [55] representations

$$\begin{aligned} &\sigma(K\tilde{x}) \in \text{co}\left\{D_i K\tilde{x} + D_i^- h(x),\ i \in [1,4]\right\}, \\ &\forall\ h(x) = [h_u\ h_v]^T : |h_j(x)| \le v_{jmax}, j = u, v \end{aligned} \tag{3.33}$$

where $D_i \in \mathbb{R}^{2\times 2}$ are diagonal matrices with 1 or 0 as diagonal elements, and $D_i^- = I - D_i$, while $h(x)$ is a generic auxiliary feedback function. Roughly speaking,

$h(x)$ can be seen as an additional degree of freedom to be exploited for describing the saturation function less conservatively, and as a consequence, obtaining sharper results for the original system. Restricting also this component to static linear laws, i.e. $h(x) = Hx$, and using (3.33), we can represent system (3.32) with the ensuing polytopic linear differential inclusion (PLDI)

$$\begin{aligned} &\dot{\tilde{x}} \in \mathrm{co}\left\{F_k\tilde{x} + G(D_iK\tilde{x} + D_i^- H\tilde{x}),\ k = \{min, max\},\ i \in [1,4]\right\}, \\ &\forall\ \tilde{x} \text{ such that } |H_j\tilde{x}| \leq v_{jmax},\ j = u, v. \end{aligned} \tag{3.34}$$

Now, the problem of limiting the system oscillations during voltage dips by means of saturated state feedback can be expressed as follows:
Assuming that, as soon as the derivative discontinuities related to the voltage dip take place, the state error $\tilde{x}$ jumps inside a known, bounded set $\mathcal{X}_0$, design a state feedback matrix K, which, under input saturation constraints (3.30)*, minimizes the error variables peak value* $\|\tilde{x}\|$.
Clearly, minimizing $\|\tilde{x}\|$ implies minimizing the oscillations of the system variables, as references i_{2u}^*,i_{2v}^* z_{2u}^*, z_{2v}^* are designed such that no oscillating components at ω_0 arise. For what regards $\mathcal{X}_0$, an estimate can be obtained considering the worst case voltage dip scenario, and the corresponding time derivatives value, which cause a step variation in references z_{2u}^*, z_{2v}^*, along with conservative margins for rotor currents tracking errors $\tilde{i}_{2u}$, $\tilde{i}_{2v}$.
A natural choice to evaluate (and shape, as far as state feedback design is concerned) the transient performance of PLDI like (3.34) is by means of invariant ellipsoid, related to level sets of quadratic Lyapunov functions [56] [57]. Here, we adopt such approach to derive a convex optimization formulation, solving the aforementioned problem. For the sake of brevity, the main result is reported, sketching only the crucial points of the strategy, we refer to [56], [57] for technical details and proofs.
In brief, the key idea is to search for the feedback matrix K, the auxiliary one H, and the corresponding quadratic Lyapunov function $V = \tilde{x}^T P\tilde{x}$, providing the smallest contractively invariant unit ellipsoid $\mathcal{E}(P) := \left\{\tilde{x} : \tilde{x}^T P\tilde{\tilde{x}} \leq 1\right\}$ enclosing the set $\mathcal{X}_0$. This would automatically give an outer bound for the norm of $\tilde{x}$, as well as the optimal feedback law. To this aim, it can be verified that the following optimization

problem [56],

$$
\begin{aligned}
&\min_{P=P^T>0,\delta>0,K,H} \delta, \text{ subject to} \\
&\begin{bmatrix} P & I \\ I & \delta I \end{bmatrix} \geq 0 \\
&F_k^T P + P F_k + P G D_i K + + P G D_i^- H + K^T D_i G^T P + H^T D_i^- G^T P < 0, \\
&k = \{min, max\},\ i \in [1,4] \\
&\begin{bmatrix} P & H_j^T \\ H_j & v_{jmax}^2 \end{bmatrix} \geq 0, \text{where } H_j,\ j = u, v, \text{ denotes the rows of } H,\ \mathcal{X}_0 \subseteq \mathcal{E}(P)
\end{aligned}
\tag{3.35}
$$

yields an upper bound of $\|\tilde{x}\|$ as the square root of the optimal value δ^*. The optimal K^* defines the feedback gains required to attain such bound, while the optimal variable P^* defines the smallest forward contractively invariant ellipsoid including $\mathcal{X}_0$. Finally, evaluating the maximum/minimum values over the ellipsoid $\mathcal{E}(P^*)$ allows to compute bounds for specific components of $\tilde{x}$, e.g. the rotor currents errors.
The first constraint expresses (by Schur complement) the fact that, if $\mathcal{E}(P)$ is invariant and contains $\mathcal{X}_0$, then $\|\tilde{x}\|^2 \leq \max_{\tilde{\xi}\in\mathcal{E}(P)} \tilde{\xi}^T\tilde{\xi}$. The second set of constraints enforces the forward contractively invariant property of $\mathcal{E}(P)$ for the PLDI (3.34), and, in turn, for the original error system. Finally, the third set of constraints ensures the inclusion of the invariant ellipsoid in the region where the PLDI description (3.34) holds true (i.e. for $\tilde{x} : |H_j\tilde{x}| \leq v_{jmax},\ j = u, v$), and the inclusion of the set $\mathcal{X}_0$ in the invariant ellipsoid. Problem (3.35) is not convex due to bilinear constraints in the variables K, P, and H. Moreover, the set inclusion $\mathcal{X}_0 \subseteq \mathcal{E}(P)$ has to be transformed into an LMI condition. If the set $\mathcal{X}_0$ is convex, this can be easily obtained. Thus, in the following, it will be assumed an ellipsoidal set $\mathcal{E}(R) := \{\tilde{x} : \tilde{x}^T R\tilde{x} \leq 1\}$, with the matrix R depending on the bounds on $\tilde{x}$ during voltage dips. In this case, the set inclusion $\mathcal{E}(R) \subseteq \mathcal{E}(P)$ can be expressed as $P - R \leq 0$. Then, defining $Q = P^{-1}$, $Y = KQ$, $Z = HQ$, by simple computations, problem (3.35) can be equivalently cast into the following *eigenvalue problem* [58]

$$
\begin{aligned}
&\min_{Q=Q^T>0,\delta>0,Y,Z} \delta, \text{ subject to} \\
&Q - \delta I \geq 0 \\
&Q F_k^T + F_k Q + G D_i Y + G D_i^- Z + Y^T D_i G^T + Z^T D_i^- G^T < 0, \\
&k = \{min, max\},\ i \in [1,4] \\
&\begin{bmatrix} Q & Z_j^T \\ Z_j & v_{jmax}^2 \end{bmatrix} \geq 0\ j = u, v,\ Q - R^{-1} \geq 0.
\end{aligned}
\tag{3.36}
$$

Beside providing less conservative results with respect to traditional absolute stability tools, description (3.34) allows to draw only local results, as it holds only inside

the *linear region* of the auxiliary law $H\tilde{x}$ (i.e. for $\tilde{x} : |H_j\tilde{x}| \leq v_{jmax}$). However, the resulting domain of convergence can be evaluated by means of similar LMI-based techniques. In fact, given the gain matrix K^*, stemming from the solution of problem (3.36), and assuming a quadratic Lyapunov candidate $V_1 = \tilde{x}^T Q_1^{-1}\tilde{x}$, a bound on the system convergence domain, under the saturated law $v = \sigma(K\tilde{x})$, can be evaluated by solving the following problem

$$
\begin{aligned}
&\min_{Q_1=Q_1^T>0,\gamma>0,Z_1} \gamma, \text{ subject to} \\
&\begin{bmatrix} Q_1 & I \\ I & \gamma R_1 \end{bmatrix} \geq 0 \\
&Q_1 F_k^T + F_k Q_1 + G D_i K^* Q_1 + G D_i^- Z_1 + Q_1 K^{*T} D_i G^T + Z_1^T D_i^- G^T < 0, \\
&k = \{min, max\},\ i \in [1,4] \\
&\begin{bmatrix} Q_1 & Z_{1j}^T \\ Z_{1j} & v_{jmax}^2 \end{bmatrix} \geq 0\ j = u, v.
\end{aligned}
\tag{3.37}
$$

where the scalar objective function and the first constraints comes from the choice of an ellipsoidal *shape reference set* $\mathcal{X}_{R1} = \{\tilde{x} : \tilde{x}^T R_1 \tilde{x}\}$ to evaluate the domain of attraction size, and the corresponding condition $(1/\sqrt{\gamma})\mathcal{X}_R 1 \subset \mathcal{E}(Q_1^{-1})$, ensuring there exists a Lyapunov candidate unit level set including the reference set scaled by $1/\sqrt{\gamma}$. Thus, minimizing γ corresponds to maximize the volume of the unit ellipsoid $\mathcal{E}(Q_1^{-1})$ with respect to a predefined shape given by R_1 (see [54] ch. 7 for further details). The LMIs in the second and third lines of (3.37) require $\mathcal{E}(Q_1^{-1})$ to be a forward contractively invariant set for system (3.31), and inclusion of such ellipsoid (estimating the domain of attraction) in the linear region of an auxiliary feedback law $H_1\tilde{x}$, with $H_1 = Z_1 Q_1^{-1}$, according to the PLDI description (3.34).
If the results (3.37) are not satisfying with the gain matrix coming from (3.36), or some guarantees on the domain of attraction want to be ensured while computing K, then the the problems (3.36), (3.37) can be suitably combined by collecting all their constraints and weighting both γ and δ in a single cost function. The previous discussion has been focused on linear and static state feedback, and considering perfectly known machine parameters. If some reasonable bounds are known for parameters uncertain values, then the same approach can be carried out, extending the differential inclusion, to represent such variations, identically to what has been done for the rotor speed ω_r. If it is not the case, and to ensure the controller with more generic robustness properties, integral dynamics can be added to the feedback structure, without significantly modifying the design procedure. In this respect, the original error dynamics can be augmented with integral terms, then a saturated linear law including integral gains can be tuned with the same methods presented before.

3.5.4 Simulations results with the proposed feedforward-feedback control solution

A controller in the form (3.29), with saturated feedback terms v_u, v_v designed according to the LMI-based procedure outlined in the previous paragraph (see Fig.3.10 for the block scheme of the overall control topology), has been applied to the considered benchmark DFIM, under the same faulty line voltage conditions reported in Subsections 3.4.1, 3.5.2. The following parameters have been considered to numerically solve problem (3.36): $v_{jmax} = u_{2jmax}/2,\ j = u, v$, $\omega_r(t) \in [0.7\omega_{nom}, 1.3\omega_{nom}]$, with $\omega_{nom} = 2\pi 50 rad/s$ representing the synchronous speed of the $50Hz$ machine. In order to represent the set of initial conditions for $\tilde{x}$ $R = diag(\tilde{z}_{2u}^{-2}, \tilde{z}_{2v}^{-2}, \tilde{i}_{2u}^{-2}, \tilde{i}_{2u}^{-2})$, where $\tilde{z}_{2u} = 0.25Wb, \tilde{z}_{2v} = 0.85Wb$, $\tilde{i}_{2u} = 100A$, $\tilde{i}_{2v} = 100A$ have been conservatively set according to the estimated jumps in z_{2u}^*, z_{2v}^* and the current tracking error during the voltage sag. The results of the optimization problem with such data are

$$K^* = \begin{bmatrix} 187.6 & -240.4 & 1.582 & -0.004 \\ 240.3 & 187.6 & 0.001 & 1.582 \end{bmatrix},$$

$$H^* = 1 \times 10^{-3} \begin{bmatrix} -1.319 & 0.570 & 1.093 & -0.008 \\ 0.0008 & 0.0013 & -0.008 & 1.093 \end{bmatrix},$$

$$P^* = \begin{bmatrix} 4.12 & 5 \times 10^{-6} & 5.8 \times 10^{-3} & 1.6 \times 10^{-5} \\ 5 \times 10^{-6} & 4.12 & 1.6 \times 10^{-5} & 5.8 \times 10^{-3} \\ 5.8 \times 10^{-3} & 1.6 \times 10^{-5} & 5 \times 10^{-6} & 1.7 \times 10^{-10} \\ 1.6 \times 10^{-5} & 5.8 \times 10^{-5} & 1.7 \times 10^{-10} & 5 \times 10^{-5} \end{bmatrix},\ \delta^* = 1.723 \times 10^5.$$

With the bound $\|\tilde{x}\| \leq \sqrt{\delta^*}$, and the matrix P^* above, it is possible to provide the following estimates of the rotor currents maximum errors $|\tilde{i}_{2u}|, |\tilde{i}_{2v}| \leq 416A$.
The corresponding simulations performance are reported in Fig. 3.11. The benefits in limiting the rotor currents oscillations can be clearly noticed in Fig. 3.11 (c)-(d), which underscores how the oscillations are sharply reduced with respect to results of both the saturated feedback linearization, and the open-loop control with zero dynamics trajectory planning. Indeed, the oscillations amplitude is within the maximum limits provided in Tab. A.1, and not far from the bound estimated above, confirming that, despite some conservative steps (LDI representation and saturation nonlinearity description), the technique discussed in the previous Subsection can be profitably exploited for realistic applications.
Note that the additional feedback action causes the control inputs to hit the assumed bounds multiple times during the grid fault (Figs. 3.11 (a)-(b)), however, since saturation is explicitly considered in carrying out the state feedback design, a graceful behavior of the system is maintained, differently from what observed for

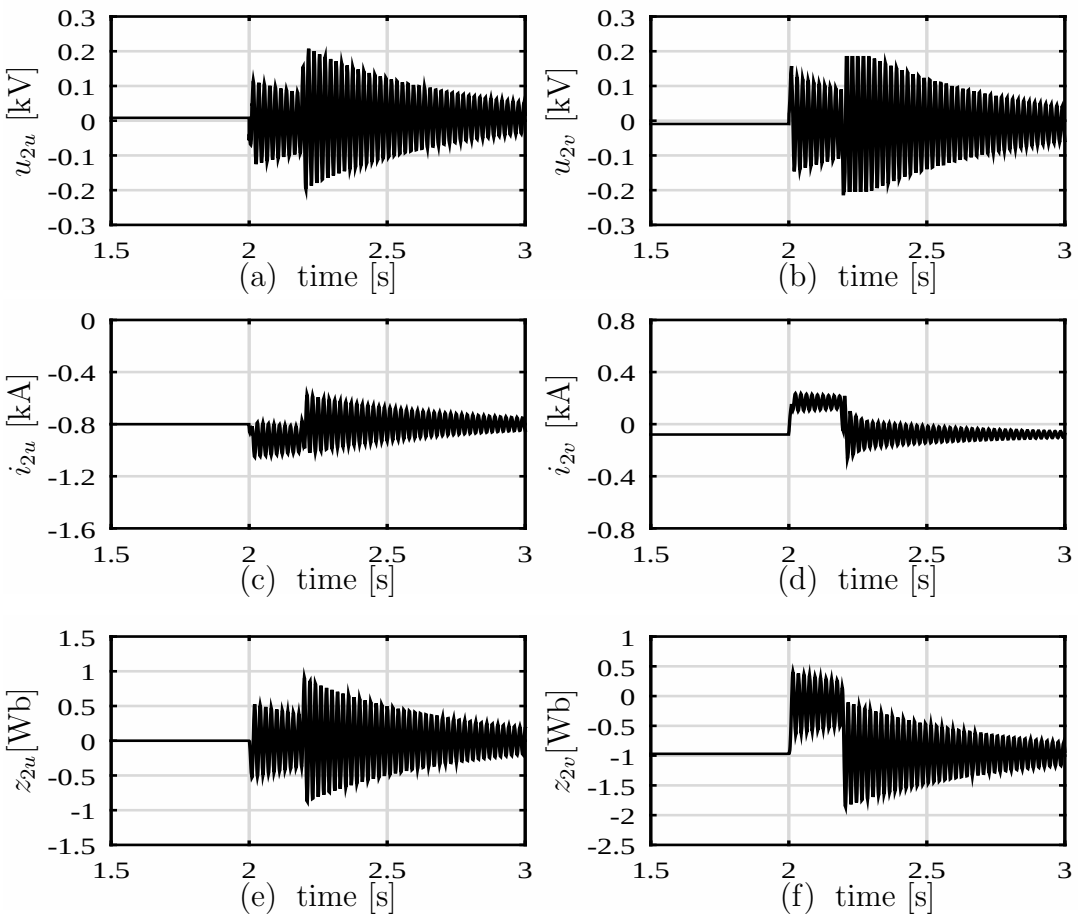

Figure 3.11: Transient results for the studied system equipped with the proposed feedforward-feedback cotnrol strategy at 85% line voltage dip. (a) Rotor u-component control voltage. (b) Rotor v-component control voltage. (c) Rotor u-component current. (d) Rotor v-component current. (e) Zero dynamics (stator magnetic flux) u-component . (f) Zero dynamics (stator magnetic flux) v-component.

the feedback linearizing approach[7].

Compared to the feedforward control solution, the stator fluxes oscillations are slightly higher, and last longer. Anyway, this is an acceptable trade off to keep the rotor current properly bounded, thus preventing the DFIG to be disconnected from the grid due to RSC overcurrent alarms, or to trigger dangerous resonant phenomena in the rotor shaft.

[7]It is worth noting that, due to some conservatism in the feedback part saturation bounds (half of the control effort is constantly preserved for the feedforward terms), the available rotor voltage range is not fully exploited (see Figs 3.11 (a)-(b)). However, the system performance under the line faults are significantly improved, keeping all the variables within the nominal range

3.6 Conclusion

In this chapter, the marginally/asymptotically stable internal zero dynamics of the studied system is studied by means of the Brunovsky forms of the system dynamics. Then, in order to find oscillation-free internal dynamics trajectories under the voltage dip disturbance, the corresponding ODEs are analytically solved in two different solutions (Sylvester and integration by parts). In the following, the system equipped with feedback linearizing controller faces a severe voltage dip in order to check the effects of the large line voltage variations on the studied system. The large oscillations of rotor fluxes/currents seen in simulation results proved that the feedback linearizing control approach is not the ideal solution for the under-dip condition. Therefore, a mixed feedforward-feedback control solution relying on modern saturated control techniques is proposed. The attained oscillation-free trajectory with respect to asymptotically stable internal dynamics is utilized as feedforward and a full-state feedback consisting of the zero dynamics and rotor currents is exploited in order to endow the closed loop system with the good tracking and limit compliance. The efficiently damped transient oscillations is validated by the simulation results This ensures not only a good torque and reactive power tracking, but also the avoidance of magnetic saturations during the grid faults. Furthermore, by keeping the rotor control voltage command inside the corresponding physical bounds, the risk of RSC over-current, during the dip, is surely avoided and the LVRT performance of the faulty system is achieved.

Chapter 4

DFIG Control under Unbalanced Dips

4.1 Introduction

Doubly-Fed Induction Machine (DFIM) is widely used for modern Wind Energy Conversion Systems (WECS) [3]. In this application framework, it is usually referred to as Doubly-Fed Induction Generator, DFIG. The typical scheme for power generation systems with DFIG was shown in Fig. 3.1; the stator windings are directly connected to the grid, while the wound-rotor is fed, by means of slip rings, with voltage provided by a controlled power electronic converter (so-called Rotor Side Converter, RSC). The main advantage of this configuration is that RSC has to manage only a fraction of the generator power, scaling with the slip percentage [5, 6], thus leading to profitable reduced rating/cost of RSC components. Moreover, four quadrant power operation can be achieved [7, 8] also thanks to the controlled boost converter adopted as Grid Side Converter (GSC), whose main task is to keep the DC-link capacitor (C in Fig. 3.1) voltage within a prescribed range, by exchanging undistorted active power with the line.
Several solutions are available, in order to decouple active and reactive power generation control. In the framework of standard vector control [10], different variants have been proposed, depending on the orientation of the considered synchronously-rotating reference frame, and the control algorithm [11, 12, 13, 14].
In the last years, due to the high penetration of renewables, many countries issued specific Grid Codes [15], [16], [17], requiring wind generation units to comply with strict technical requirements, in order to be safely integrated in the power network. A challenging specification regards the Low Voltage Ride Through (LVRT) property, i.e. the ability to remain connected to the grid under voltage dips, while providing some ancillary services, such as reactive current support. As mentioned before,

voltage dips are very critical disturbances for DFIG. Indeed, such events, owing to current limits, reduce the amount of power which can be injected into the line, impairing the wind turbine energy balance (DFIG would generate a power surplus w.r.t. what can be transferred to the grid). Therefore, a sudden reduction in the DFIG torque is usually needed to prevent overvoltage in the DC-link capacitor. Furthermore, in the last chapter, DFIG's high sensitivity to grid low voltage faults was analyzed by presenting the corresponding zero dynamics in which the grid/stator voltage (since the stator windings are directly connected to grid) enters the dynamics as an exogenous input. As illustrated in simulations of the previous chapter, the line variation caused by the grid fault triggers high oscillations in currents and fluxes of both stator and rotor windings. Usually, in particular for asymmetrical dips [20], [21], this phenomenon also makes standard controllers give large voltage commands on RSC, hitting saturation constraints and possibly leading to converter overcurrents.

Many solutions have been suggested in recent literature to cope with such issues. Except the standard crowbar protection, as the classic remedy, a popular strategy is based on demagnetizing current reference [23], i.e. rotor currents set points are modified during the dip, to oppose the components arising in the stator flux; in [24], [25], and [26], virtual resistor, variable structure and hysteresis current controller are respectively exploited for such purpose. In [27] the rotor current reference is switched onto the stator current measurements, while in [28] the reference switch is performed on the rotor flux linkage, scaling it down when a fault is detected, in order to limit rotor current oscillations. In [29], a nonlinear PI-like controller is proposed to stabilize the DFIG dynamics and improve post-fault behavior, while [30], [31] propose feedforward transient compensation terms, added during fault to reduce the system sensitivity to the line voltage disturbance. However, the control-based methods presented in literature can deal only with mild unbalanced sags [37]. Therefore, combination with some auxiliary dedicated hardware is commonly adopted to prevent system tripping under severe asymmetric faults (see [34], [38], [39] for recent proposals exploiting innovative auxiliary hardware).

In this context, the main contribution of this chapter is to propose a novel control strategy for DFIG (i.e. acting on RSC) that is capable of achieving full LVRT features, without additional hardware requirements (w.r.t. what needed for normal operation), even in case of very hard unbalanced line faults, usually not covered by the control-based solutions presented in literature (neither in simulation tests, to the best of our knowledge). To this aim, advanced control theory tools are exploited, first for a clear analysis of the line voltage disturbance effects, then to design a suitable mixed feedforward-feedback solution, based on the analysis results and explicitly accounting for the system's constraints.

Control objectives for the considered class of systems are typically specified in terms of torque and reactive power at the stator side. As will be discussed in the last chapter in details, these original references are suitably mapped into the corresponding (stator or rotor) current references. Here, assuming rotor currents as the output variables to be controlled, the Brunovsky form [40] of the system dynamics is utilized, in order to clearly analyze the zero dynamics, driven by the line voltage and the rotor current references. Such analysis is exploited to design suitable state reference trajectories, based on Sylvester equations and line voltage observation. Even in case of severe symmetrical or unsymmetrical dips, these reference trajectories are free from unpleasant oscillations, related to the poorly-damped oscillatory natural dynamics shown by DFIG in synchronous reference frames (these dynamics turn into a set of almost-pure integrators in a stator stationary frame). The removal of the effects of natural DFIG dynamics in state reference generation, combined with the properties of Sylvester equations, is a key step in the path to achieve robustness to very harsh dips. Indeed, this approach encompasses and extends the basic demagnetization methods, in order to deal with severe unsymmetrical and generic voltage dips. The state reference trajectories thus obtained are used to generate feedforward compensations and design a state feedback part to effectively push the real variables toward the reference ones. The feedback part, taking advantage of the results in [41] in combination with saturated control techniques, allows to further tame oscillations, while dealing with rotor voltage limits, similar to what presented in the last chapter. More specifically, since to obtain full LVRT capability the first task is avoiding overcurrent in RSC, the saturated feedback controller is designed to minimize transients on rotor currents. Finally, a line voltage reconstruction and dip detection unit is designed, based on state observers theory. This unit is crucial, in order to reliably and robustly provide such information to the controller.
This chapter whose contents is according to [59] is organized as follows. In Section 4.2, the general objectives are reported, and the system zero dynamics are briefly recalled, introducing the key ideas for the control strategy. In Section 4.3, unbalanced voltage dip characterization is carried out, recalling the asymmetric fault effect on the line voltages, which will be exploited to consider a suitable model to be used for control purposes. In Section 4.4 the proposed control scheme is presented, showing how to design natural-modes-free zero dynamics trajectory, using Sylvester equations, also under unbalancement, building the corresponding feedforward action, and completing it with LMI-based saturated state feedback design. Line voltage observers and the fault detection method are also introduced. The approach is validated in Section 4.5, via detailed simulations. First, comparisons with a recent solution (based solely on control), presented in [28], are discussed. Then, a harsher asymmetric fault case is considered to further motivate and highlight the features of

the proposed method. Section 4.6 ends the chapter with some final considerations.

4.2 Basic Idea for Control

In this Section, the DFIG dynamics are recalled, and the key system features are introduced, along with the main idea for the control solution. The elaboration will be carried out considering Stator Voltage Oriented (SVO) reference frame, which is a quite standard choice allowing to easily formulate and decouple control objectives [6], [11]. Actually, as it will be detailed later on, an estimated angular position will be used to generate the SVO frame; in nominal condition such angle will be aligned with the line one while, during dips, the projection along time of the pre-fault line behavior will be used, in order not to make the controller sense the line angle jumps and fluctuations during faults. In such rotating frame, it is highlighted how DFIG shows poorly damped oscillatory modes, directly affected by line voltage perturbations. If not properly handled, these can lead to rotor voltage saturation and, as a consequence, overcurrents due to a controllability loss.
Starting from the general modeling given in [6] Ch. 13, the above-mentioned characteristics can be underscored by converting the standard model into the Brunowsky/normal form, selecting the rotor currents as controlled outputs[1]. Thus, the following DFIG electromagnetic dynamics, are considered:

$$\begin{aligned}
\dot{i}_{2u} &= -\gamma_2 i_{2u} + (\omega_L - \omega_r) i_{2v} + \beta_2 \alpha_1 z_{2u} - \beta_2 \omega_r z_{2v} - \beta_2 u_{1u} + \tfrac{u_{2u}}{\sigma_2} \\
\dot{i}_{2v} &= -(\omega_L - \omega_r) i_{2u} - \gamma_2 i_{2v} + \beta_2 \omega_r z_{2u} + \beta_2 \alpha_1 z_{2v} - \beta_2 u_{1v} + \tfrac{u_{2v}}{\sigma_2} \\
\dot{z}_{2u} &= -\alpha_1 z_{2u} + \omega_L z_{2v} + \alpha_1 L_m i_{2u} + u_{1u} \\
\dot{z}_{2v} &= -\omega_L z_{2u} - \alpha_1 z_{2v} + \alpha_1 L_m i_{2v} + u_{1v} \\
T_m &= \eta_2 (z_{2v} i_{2u} - z_{2u} i_{2v})
\end{aligned} \tag{4.1}$$

where (i_{2u}, i_{2v}), (u_{1u}, u_{1v}) are the rotor current and line voltage components in the SVO frame, rotating synchronously at the line frequency ω_L. Note that since u_{1u} is aligned with the voltage vector amplitude, in the steady-state condition u_{1v} is null, while under the unbalanced faulty scenarios it may take different values (depending on the dip shape). ω_r is the rotor electrical speed, and the other parameters have been defined as (1.24) in Ch. 1.
The electrical coefficients appearing in the definitions above are reported in Tab. A.2. Numerical values are referred to a $1.5MW$, $50Hz$ DFIM which will be used for the solution validation and comparison with the LVRT method in [28], where the same machine has been taken as case study. Like the previous chapters, (z_{2u}, z_{2v})

[1]This choice is quite natural, since rotor side converter is the most sensitive device to be protected under line faults. Furthermore, wind turbines control goals (torque and reactive power) are commonly mapped into rotor current references.

denote the internal dynamics variables, which, for the given selection, coincide with the stator fluxes, and T_m is the electromagnetic torque. Now, exactly similar to what we did in Subsection. 3.3.2 in the previous chapter, defining the current errors $\tilde{i}_{2u} = i_{2u} - i^*_{2u}$, $\tilde{i}_{2v} = i_{2v} - i^*_{2v}$ w.r.t. references i^*_{2u}, i^*_{2v}, the corresponding zero dynamics (i.e. for $\tilde{i}_{2u} = \tilde{i}_{2v} = 0$) are:

$$\begin{aligned} \dot{z}_{2u} &= -\alpha_1 z_{2u} + \omega_L z_{2v} + \alpha_1 L_m i^*_{2u} + u_{1u} \\ \dot{z}_{2v} &= -\omega_L z_{2u} - \alpha_1 z_{2v} + \alpha_1 L_m i^*_{2v} + u_{1v}. \end{aligned} \tag{4.2}$$

The ODEs above, similar to 3.7 in 3 (the difference is that here we have also the u_{1v} component due to unbalanced framework) define a LTI system which, given the typical machine parameters values (low α_1), shows lightly damped oscillatory modes, which can be triggered by perturbations in the line voltage, entering directly in (4.2) as input. However, recalling standard system theory results, the response of a (marginally or asymptotically) stable system is the composition of a (vanishing) transient response, related to initial condition and inputs, and a steady state response, again depending on initial state and inputs (or, under some conditions, just inputs). Such considerations can be exploited to remove the terms related to the oscillatory modes of the system zero dynamics response, by finding a natural-modes-free trajectory, which is consistent with the inputs (line voltage and rotor current references). In this case, zero dynamics are given by a (poorly damped, asymptotically stable) LTI system then, by applying superposition principle, we can express its solution as the summation of: a free transient response (related only to initial state, assuming null inputs, and vanishing due to asymptotic stability, according to the system eigenvalues), a forced transient response (related only to inputs, assuming null initial condition, and evolving according to inputs and system eigenvalues, but vanishing) and a forced steady state part (depending only on inputs and not on the system modes). Whenever inputs can be described by linear exosystems (e.g. integrator for constants, oscillator for sinusoids), the forced steady state response can be obtained by solving Sylvester equations [40]. The forced steady state response is an admissible trajectory for the zero dynamics subsystem, since it is always possible to select a suitable initial condition such that the free and forced transient parts cancel each other out. In addition, the forced steady state response of (4.2) is free from the natural oscillatory modes at $-\alpha_1 \pm j\omega_L$, hence such trajectory can be reasonably expected to prevent troubles with voltage saturation and overcurrent.
Bearing in mind these reasoning, the main idea for controlling DFIG under dips is the following: having the inputs (u_{1u}, u_{1v}) and (i^*_{2u}, i^*_{2v}) trajectories, compute the corresponding forced steady state response, and steer the system toward such trajectories by means of a suitable feedforward-feedback controller. This idea will be elaborated in Section 4.4, after presenting dip characteristics in Section 4.3.

4.3 Unbalanced Dip Characteristics

As mentioned before, a typical power system voltage dip consists of three different stages: falling, stabilizing, and recovering [33], as illustrated in Fig.4.1 (a). As detailed in Section 2.2 of Ch. 2, two broad classes of faults can be outlined: in symmetrical/balanced dips conventionally called type A, all the three phases are affected in an identical way by the fault, thus only a variation in the line voltage vector amplitude occurs. While, asymmetrical/unbalanced dips involve only some phases, introducing, in the SVO framework, negative sequence components, i.e. counter-rotating harmonics at double the line frequency [60]. Among the several kind of asymmetrical dips we defined in Section 2.2, the single phase-to-ground fault (SPGF) is the most frequent one [61]. However, since there is usually a star-delta-connected transformer between the grid and the wind turbine, the fault type at the DFIG terminal may differ from what happens upstream [62]. For instance, a single-phase grid voltage dip will be converted to a two-phase dip at the terminal of DFIG [63].

In this chapter, three different dip types will be considered. First, a 70% symmetric dip type A, and a 90% SPGF type B, will be used for comparison with the approach presented in [28]. As for that work, a step-wise falling and recovering stages have been assumed, while the flat part lasts $200ms$. Then, a severe two-phase-to-ground fault type E, lasting $625ms$ has been considered. In this respect, phases b, c experience 100%, and 85% drop, [2] w.r.t. their nominal values, respectively, while phase a is kept unchanged (see Fig.4.1-(b)). To reproduce the profile of a realistic unbalanced voltage sag, the faulty voltages are passed trough a pair of linear filters. In particular, a second order filter with natural frequency at $393Hz$ is placed downstream the faulty phases, in order to emulate line resonance phenomena [64]. To this aim, a rather low damping coefficient, equal to 0.3 has been selected. In addition, a filter acting on the amplitude of the faulty voltages, has been used, with the goal to approximate the effects of the electromechanical devices acting on the grid. Thus, a pair of complex conjugate poles with natural frequency $7Hz$, with a damping coefficient equal to 0.1 has been placed. However, to avoid smoothing the dip falling and recovering stages with such a slow bandwidth, a fast pole at $5KHz$, and a couple of resonant zeros with natural frequency at $6Hz$ and damping coefficient equal to 0.1, have been added to the filter transfer function. This way, a fast decay is ensured and, at the same time, an oscillating tail at $7Hz$, approximating the electromechanical devices response, is obtained. Finally, such devices can have multiple connections/disconnections during a fault, particularly at the beginning

[2] To comply with the fact that, in the real life, it rarely happens to have equal short-circuit impedances for different phases, we have considered different dip amplitudes for the phases b, c.

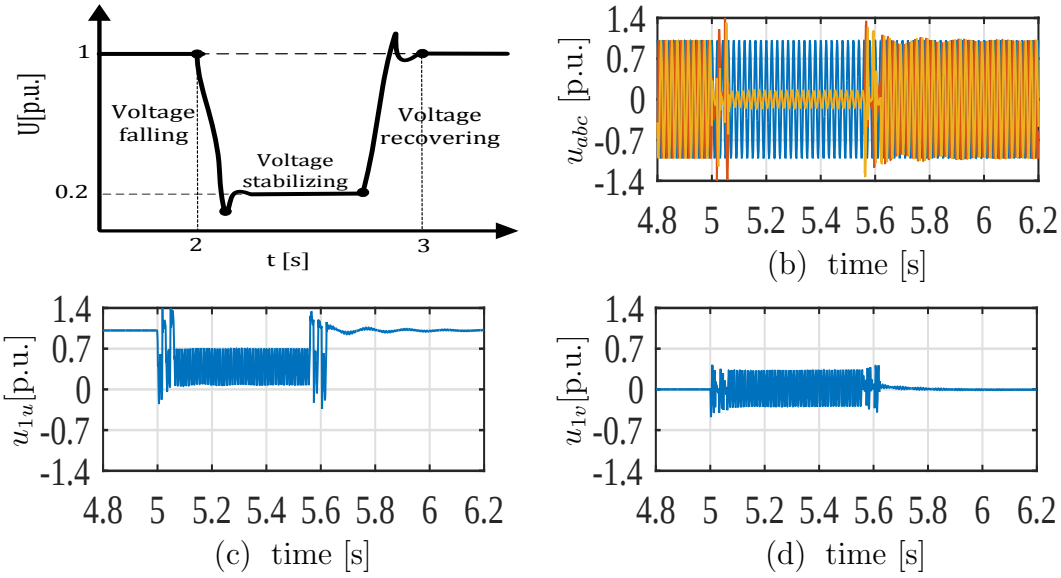

Figure 4.1: Characteristics of the line voltage under the considered two-phase-to-ground unbalanced dip lasting for $625ms$. (a) Typical voltage dip of power system. (b) Line voltage a, b, c components. (c) SVO framework u-component. (d) SVO framework v-component.

and the end. To emulate also such situation, step-wise "bounces" decreasing and increasing (back to the nominal value) the amplitude have been implemented upstream the $7Hz$ filter.

The overall effects of the mentioned dip emulation are shown in Fig. 4.1 (b). It can be noted how, due to the filtering effects, the shape approximate the typical dip illustrated in Fig. 4.1 (a), actually worsening the transients with overshoots, and the aforementioned amplitude bounces. Accordingly, similar effects can be seen in Figs. 4.11:(c)-(d), for both components of the stator voltage in the SVO framework. In addition, a $2\omega_L$ component, related to negative sequences, arises and persists also during the steady-state condition during the flat part of the fault.

Bearing in mind all these considerations, for the control design (later discussed in Subsection 4.4.4), beside the DC components, the faulty voltage profile model will include also $2\omega_L$ sinusoidal components, to account for unbalanced conditions. Furthermore, a non standard fault detection unit is proposed, to robustly cope with harsh faults as the one presented in this Section.

4.4 Control Solution

In this Section the proposed control structure is elaborated: given rotor current references (their generation will be specified later on) and assuming line voltage

description as in Section 4.3, the first step is to generate the forced state trajectory for the zero dynamics (4.2). Then, suitable feedforward and state feedback actions are designed, ensuring asymptotic state (zero dynamics and rotor currents) references tracking, and preventing overcurrent and harmful effects of control inputs saturation.

4.4.1 Generation of zero dynamics forced steady state response

In order to compute the steady state forced part of (4.2) piecewise constant reference rotor currents are assumed (such choice will be motivated later on in this Section) while, for what concerns the line voltage, constant and counter-rotating sinusoidal component at $2\omega_L$, in the SVO $u-v$ frame, will be considered, according to the analysis in Section 4.3. Therefore, defining $v = [i^*_{2u}\ i^*_{2v}\ u_{1u}\ u_{1v}]^T$, we can represent the zero dynamics inputs by the following linear exosystem

$$\begin{bmatrix} \dot{i}^*_{2u} \\ \dot{i}^*_{2v} \\ \dot{w} \end{bmatrix} = \underbrace{\begin{bmatrix} \Omega_I & 0 \\ 0 & \Omega_w \end{bmatrix}}_{\mathbf{\Omega}} \begin{bmatrix} i^*_{2u} \\ i^*_{2v} \\ w \end{bmatrix},\ v = \Gamma[i^*_{2u}\ i^*_{2v} w^T]^T \tag{4.3}$$

$$\Gamma = blkdiag(1,1,\Gamma_w),\ \Omega_I = 0_{2\times 2},\ \Omega_w = blkdiag(0_{2\times 2}, S)$$

with $\Gamma_w = \begin{bmatrix} 1 & 0 & 1 & 0 \\ 0 & 1 & 0 & 1 \end{bmatrix}$, $S = \begin{bmatrix} 0 & 2\omega_L \\ -2\omega_L & 0 \end{bmatrix}$. Then, recalling the reasoning in Section 4.2, the forced steady state response of system (4.1), corresponding to the class of inputs described by (4.3), can be obtained by solving, for Π, the following Sylvester equation

$$\Pi\ \mathbf{\Omega} = A\Pi + B\Gamma \tag{4.4}$$

where $A = \begin{bmatrix} -\alpha_1 & \omega_L \\ -\omega_L & -\alpha_1 \end{bmatrix}$, $B = \begin{bmatrix} \alpha_1 L_m & 0 & 1 & 0 \\ 0 & \alpha_1 L_m & 0 & 1 \end{bmatrix}$. Thus, natural-modes-free trajectories for dynamics (4.2) can be computed as

$$[z^{FSS}_{2u}\ z^{FSS}_{2v}]^T = \Pi[i^*_{2u}\ i^*_{2v}\ w^T]^T. \tag{4.5}$$

Eq. (4.4) can be uniquely solved whenever matrices A and $\mathbf{\Omega}$ have separated spectra, that is inputs u have no components at system (4.2) resonance frequency ω_L. According to the discussion in Section 4.3, this condition is verified also under unbalanced dips.

Generation of references (4.5) requires the line voltage to be split in its constant and sinusoidal components (collected in vector w). Being the pair (Ω_w, Γ_w) observable, this information can be retrieved by means of a state observer, defined as

$$\dot{\hat{w}} = \Omega_w \hat{w} + L(u_1 - \Gamma_w \hat{w}),\ \text{ with } u_1 = [u_{1u}\ u_{1v}] \tag{4.6}$$

where $\hat{w}$ is the state estimate and, by tuning matrix L, the poles/bandwidth of the observer can be arbitrary imposed, so that fast reconstruction of the line voltage signal components can be achieved under line faults.

4.4.2 Observer for line angle reconstruction in nominal and faulty condition

The steady state solution (4.5) and observer (4.6) are designed in a rotating reference frame, $u-v$, which, as anticipated at the beginning of Section 4.2, is supposed to be aligned with the line voltage angle, in nominal conditions, and with its ideal forward projection along time, in faulty conditions. Such reference frame must be generated as well.

The basic idea, is to use another observer scheme to track the line angle, referred as θ_L, in healthy conditions, by exploiting measurement feedback, while, during dips, the feedback correction will be removed, obtaining the forward projection by pure integration of its model equations. The basic observer structure will be considered first, then the mechanism to smoothly switch between the above mentioned conditions will be specified.

A PLL-like polar coordinates observer topology, first presented in [65], is exploited. The reason for choosing this unconventional voltage reconstruction architecture is that it shows strong robustness against measurements perturbations and negative sequence components, arising in asymmetric sags as shown in Section 4.3. The main idea is to perform estimation in a generic rotating reference frame, but imposing estimates dynamics equivalent to what they would be in a frame aligned with the line voltage vector, then to "truly" align the observer by means of suitable correction terms. For brevity here the final observer structure, reported also in Fig. 4.2, is recalled (we refer the interested reader to see [65] for details)

$$\begin{aligned} &\dot{\hat{u}}_{1u} = k_2\tilde{u}_{1u},\ \hat{u}_{1v} = 0,\ \dot{\hat{\bar{\omega}}}_L = \frac{1}{\gamma}\hat{u}_{1u}\tilde{u}_{1v} \\ &\hat{\omega}_L = \frac{k_1}{\hat{u}_{1u}}\tilde{u}_{1v} + \hat{\bar{\omega}}_L,\ \dot{\hat{\theta}}_L = \hat{\omega}_L \end{aligned} \tag{4.7}$$

estimates are denoted with accent $\hat{}$), with errors $\tilde{u}_{1u} = u_{1u} - \hat{u}_{1u}$, $\tilde{u}_{1v} = u_{1v} - \hat{u}_{1v}$, with signals $u_{1\hat{u}},\ u_{1\hat{v}}$ coming from three-phase measurements expressed in the observer frame, rotating with $\hat{\theta}_L$, via Clarke+Park transformation (denoted as $T(\hat{\theta}_L)$ in Fig. 4.2). Finally, k_1, k_2, γ are arbitrary positive gains to be exploited for tuning.

Despite the observer provides full line voltage information (estimated quantities are denoted with accent $\hat{}$), only the angular position $\hat{\theta}_L$ will be exploited to build the considered $u-v$ reference frame, then to implement observer (4.6), trajectories (4.5) and the control scheme which will be defined later. Whenever a dip occurs,

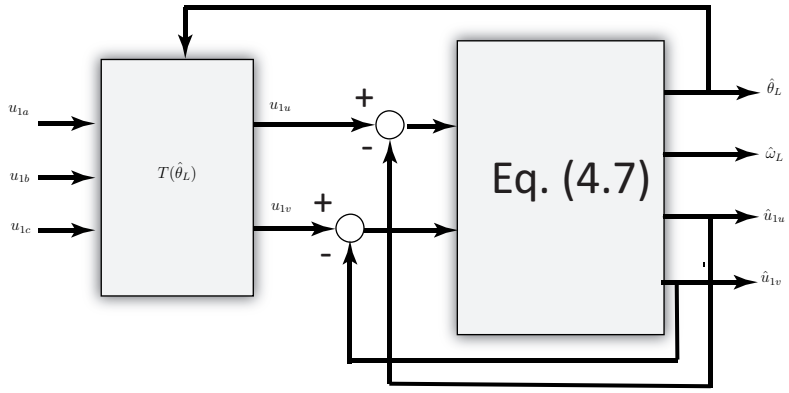

Figure 4.2: Schematic structure of the polar coordinates line observer.

forward projection of the nominal line angle evolution is obtained by switching off the feedback part in (4.7), i.e. zeroing all the right terms except for $\dot{\hat{\theta}}_L$ equation. Being the grid faults commonly short (the duration is less then 1 sec.), the open loop forward projection of the estimated angle during the dip is not expected to drift much from the healthy line phase. Thus no issues for the controller should arise. In addition, at the fault clearance, observer feedback should be restored in order to recover the alignment.

The dip detection/clearance mechanism is arranged by using a finite state machine and two observers having the structure in eq. (4.7): a Low Bandwidth Observer (LBO), which is used to provide the $u-v$ reference frame angle, and an additional High Bandwidth Observer (HBO), which is exploited for robust and reliable dip events and clearance detection. Clearly, the LBO is tuned to have a slow response to line voltage variations, while the HBO will be much faster. The adopted finite state machine is shown in Fig. 4.3, where estimates provided by the HBO are denoted with subscript F.

In the initialization phase (INIT), both the observers will lock in, after a suitable transient. This part is not deeply detailed, since it will be part of the WECS start up procedure. Once initialization has ended, NOMINAL state becomes the active one. As soon as a dip takes place, a large estimation error will arise in the LBO because of its low bandwidth; this is used as a residual to trigger fault detection (with a certain time hysteresis $\bar{t}$), and remove adaptation in the LBO, which will operate in open loop throughout the entire dip, while the HBO is kept on (see NOMINAL to FAULTY state transition in Fig. 4.3). At the dip clearance, the HBO's voltage estimates will be back to constant values "close enough" ($\hat{u}_{uF} >$ greater than 80%

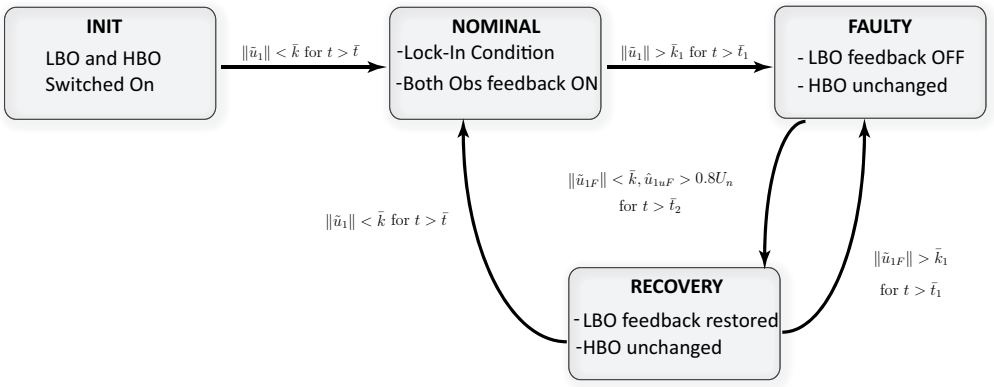

Figure 4.3: Scheme of Dip occurrence/clearance detection logic built on the HBO, LBO polar coordinate observers estimates.

of standard line amplitude U_n) to the nominal one. Such condition is exploited to restore the slow observer feedback and re-align the reference frame with the healthy line (see FAULTY to RECOVERY transition in Fig. 4.3), possibly tuning the LBO gains in order to make re-alignment faster. Finally, when the LBO estimation error is within a given threshold, the logic scheme comes back to the nominal state. Instead, if a fault takes place during the LBO recovery stage, it is detected by monitoring the HBO estimates, which, given the observer fast response, will quickly track line changes, drifting away from the nominal values. In this case, the system is switched back to the faulty scenarios before the re-alignment is completed, disconnecting the LBO feedback again and using the last estimates of the LBO to integrate the angular position (see RECOVERY to FAULTY transition in Fig. 4.3).

4.4.3 Rotor currents reference generation

The last piece of information to compute trajectories in (4.5), is to define rotor current references (i^*_{2u}, i^*_{2v}). As mentioned in the Introduction, common wind turbine control goals are stated as electromagnetic torque and stator reactive current set-points. Therefore, a suitable mapping to rotor currents has to be established.
Typically, torque T^*_m and stator reactive current i^*_{1v} references are slowly varying w.r.t DFIG electromagnetic dynamics, then, from a mathematical view point, we perform the mapping assuming such signals as constant (or piecewise constant). Therefore, rotor current references can be computed using the following expressions for torque and reactive current $T^*_m = \eta_2(z^*_{2v} i^*_{2u} - z^*_{2u} i^*_{2v})$, $i^*_{1v} = \frac{z^*_{2v} - L_m i^*_{2v}}{L_1}$. Both T^*_m and i^*_{1v} depend not only from rotor currents, but also from the zero dynamics (stator fluxes in the considered case) as well. However, we can replace the zero-dynamics variable references (z^*_{2u}, z^*_{2v}) with trajectories in (4.5), as, by virtue of the system properties, discussed in Subsection 4.4.1, we expect the zero dynamics to converge

on these solutions. Forced steady state response in (4.5) itself depends on rotor currents and line voltage components. In this way, a system depending only on rotor current references and known terms ($\hat{w}$ from (4.6) is used in place of w in (4.5)) is obtained and can be easily solved.
Actually, along asymmetric dips, oscillatory components of the line voltage would lead to oscillating zero dynamics according to (4.5)[3]. As a consequence, to obtain constant T_m^* and i_{1v}^* under steady-state oscillatory zero dynamics, oscillating references (i_{2u}^*, i_{2v}^*) would be produced, violating the hypothesis made to build the exosystem (4.3). To avoid such inconsistency, (i_2^*, i_{2v}^*) are computed considering, for the zero dynamics, the forced steady state response related to just the constant components of the line voltage, and clearly (i_{2u}^*, i_{2v}^*). In other words, z_{2u}^*, z_{2v}^* for T_m^*, i_{1v}^* are computed as in (4.5), but using only the first two components ($u-v$ integrators) of the (estimated) vector w, and cutting Π accordingly to its first four columns. The equations obtained by this procedure are reported below

$$\begin{aligned} T_m^* &= \frac{\eta_2((\omega_L\alpha_1 Lm(i_{2u}^{*2}+i_{2v}^{*2})-(\omega_L\hat{w}_1+\alpha_1\hat{w}_2)i_{2u}^*+(\alpha_1\hat{w}_1+\omega_L\hat{w}_2)i_{2v}^*)}{\alpha 1^2+\omega_L^2} \\ i_{1v}^* &= \frac{-\omega_L\alpha_1 L_m i_{2u}^*+L_m(\alpha_1^2-1)i_{2v}^*-\omega_L\hat{w}_1+\alpha_1\hat{w}_2}{L_1(\alpha_1^2+\omega_L^2)} \end{aligned} \tag{4.8}$$

where $\hat{w}_1$, $\hat{w}_2$ denote the estimated constant line voltage $u-v$ components, respectively obtained by (4.6). This way, constant rotor current references can be obtained. Clearly, the reminder oscillatory part of the zero dynamics, which has been neglected in (4.8), will lead to some oscillations in the actual torque and reactive current signals. However, their average values will be identical to the desired constant references.

4.4.4 Feedforward-feedback controller design

Having defined methods for generating natural-modes-free zero dynamics trajectories, and current references suitable for torque and reactive current regulation, a control strategy, ensuring asymptotic tracking of these set-points, is needed. To this purpose, a feedforward-feedback structure is exploited, based on the previous analysis and reference generation strategy for what concerns feedforward terms, while a saturated state feedback part will be designed to further minimize oscillations, particularly for rotor currents, under line faults, and accounting for rotor voltage limits.
Starting with the feedforward part, by (4.1), to track references (i_{2u}^*, i_{2v}^*), (z_{2u}^*, z_{2v}^*), defined according to (4.8) and (4.5) respectively, the following open-loop law can be

[3]Clearly this are steady-state forced oscillations, not related to system (4.2) natural modes, but forced by the $2\omega_L$ counter-rotating terms given by unbalancement.

designed

$$\begin{aligned} u_{2uff} &= \sigma_2 \left(\gamma_2 i^*_{2u} - (\omega_L - \omega_r) i^*_{2v} - \alpha_1\beta_2 z^*_{2u} + \beta_2\omega_r z^*_{2v} + \beta_2 u_{1u}\right) \\ u_{2vff} &= \sigma_2 \left(\gamma_2 i^*_{2v} + (\omega_L - \omega_r) i^*_{2u} - \alpha_1\beta_2 z^*_{2v} - \beta_2\omega_r z^*_{2u} + \beta_2 u_{1v}\right). \end{aligned} \tag{4.9}$$

Taking advantage of the DFIG inherent properties, global asymptotic tracking can be shown to be ensured by the pure feedforward controller above (very similar arguments to what in [41] can be used for proving such result, thus, for brevity, we refer to that work for details). This result is instrumental for achieving rotor current tracking, and natural-modes-free internal dynamics, for stretches of piecewise constant references, and line voltage behavior complying with description (4.3). As remarked in Section 4.3, these conditions holds only in the flat part of the dip, while during transients, spurious harmonic contents, not captured either by (4.3) nor (4.6), arise in the voltage. Similarly, not constant current references will be generated as a consequence of the torque and reactive current reference variations. As a result, solution (4.5) will not be exact and, in turn, some oscillations will be triggered.
In order to deal with such issue, and provide the controller with robustness as well, controller (4.9) is modified as:

$$u_{2u} = u_{2uff} + \xi_u,\ u_{2u} = u_{2vff} + \xi_v \tag{4.10}$$

with ξ_u, ξ_v state feedback terms to be designed in order to dampen oscillations and comply with the RSC actuation limits. In this respect, the following saturated linear law is defined

$$\xi = \sigma(p) = \begin{bmatrix} sat(p_u) \\ sat(p_v) \end{bmatrix},\ p = K\tilde{x}_a \tag{4.11}$$

with $\tilde{x}_a = [\tilde{x}^T\ \ \tilde{\chi}^T]^T$, $\tilde{x} = \left[\tilde{z}_{2u}\ \tilde{z}_{2v}\ \tilde{i}_{2u}\ \tilde{i}_{2v}\right]^T$, and $\tilde{\chi} = \left[\underbrace{\int \tilde{i}_{2u}}_{\tilde{\chi}_u}\ \underbrace{\int \tilde{i}_{2v}}_{\tilde{\chi}_v}\right]^T$ integral terms on rotor currents, providing some robustness against parametric uncertainties. While $\xi = [\xi_u\ \xi_v]^T$ and $sat(p_j) = (sgn(p_j))(\min\{\xi_{jmax}, |p_j|)\})$, $j = u, v$. Bounds for ξ_u, ξ_v clearly depend on the machine maximum rotor voltages u_{2umax}, u_{2vmax}, stemming from RSC rated values and the control effort required by the feedforward terms. The latter vary with the operating conditions. However, assuming some a-priori knowledge about the system set of trajectories, safe constant margins $u_{2jffmax}$, $j = u, v$ can be preserved for u_{2uff}, u_{2vff}, and then define constant limits $\xi_{jmax} = u_{2jmax} - u_{2jffmax}$, $j = u, v$, accordingly.

Applying controller (6.7)-(4.11), yields

$$\dot{\tilde{x}}_a = F(t)\tilde{x}_a + G\sigma(K\tilde{x}_a), \text{ with } G = \begin{bmatrix} 0 & 0 & -\frac{1}{\sigma_2} & 0 & 0 & 0 \\ 0 & 0 & 0 & -\frac{1}{\sigma_2} & 0 & 0 \end{bmatrix}^T$$
$$F(t) = \begin{bmatrix} -\alpha_1 & \omega_L & \alpha_1 L_m & 0 & 0 & 0 \\ -\omega_L & -\alpha_1 & 0 & \alpha_1 L_m & 0 & 0 \\ \alpha_1\beta_2 & -\beta_2\omega_r(t) & -\gamma_2 & \omega_L - \omega_r(t) & 0 & 0 \\ \beta_2\omega_r(t) & \alpha_1\beta_2 & \omega_r(t) - \omega_L & -\gamma_2 & 0 & 0 \\ 0 & 0 & 1 & 0 & 0 & 0 \\ 0 & 0 & 0 & 1 & 0 & 0 \end{bmatrix}. \tag{4.12}$$

System above is time-varying due to rotor speed ω_r, and nonlinear due to control inputs saturation. The inclusion $F(t) \in \text{co}\{F_{min}, F_{max}\}$ can be used to handle the first issue, where F_{min}, F_{max} are evaluations of F at the rotor speed range extreme values ω_{rmin}, ω_{rmax}, respectively, while co denotes the convex hull of the matrices between braces. For what regards saturation, exploiting Lemma 7.3.2 in [54], the following inclusion can be derived

$$\begin{aligned} &\sigma(K\tilde{x}_a) \in \text{co}\left\{D_i K\tilde{x}_a + D_i^- H(\tilde{x}_a),\ i \in [1,4]\right\} \\ &\forall\ H\tilde{x}_a = [h_u\ h_v]^T : |H_j\tilde{x}_a)| \leq \xi_{jmax}, j = u, v \end{aligned} \tag{4.13}$$

where D_i are diagonal matrices with 1 or 0 as entries, and $D_i^- = I - D_i$, while H is an auxiliary feedback which is exploited as a degree of freedom for representing saturation function less conservatively w.r.t. standard absolute stability and vertex analysis methods. Combining these descriptions, the nonlinear system (6.8) can be analyzed (with some conservatism) by means of the following Polytopic Linear Differential Inclusion (PLDI)

$$\begin{aligned} \dot{\tilde{x}}_a \in \text{co}\{F_k\tilde{x}_a + G(D_i K\tilde{x}_a + D_i^- H\tilde{x}_a)\},\ k = \{min, max\}, \\ i \in [1,4],\ \forall\ \tilde{x}_a \text{ such that } |H_j\tilde{x}_a| \leq v_{jmax},\ j = u, v. \end{aligned} \tag{4.14}$$

Now, the problem of limiting oscillations during voltage dips via saturated state feedback (4.11) can be seen as finding a gain matrix K so that the peak value $\|\tilde{x}\| = \|C\tilde{x}_a\|$, with $C = [I_4\ 0_{4\times 2}]$, is minimized. It is worth to point out that, despite the output matrix C weights all the components of $\tilde{x}$ in the same way, given the different scales of rotor currents and stator fluxes, the peak error values of the former will be penalized more. As it will be shown in Section 4.5, this allows to keep the rotor currents within the physical bounds, also under very harsh unbalanced line faults.

In addition, we assume that oscillations triggered during at dip occurence, makes $\tilde{x}_a$ to "jump" inside a known bounded set $\mathcal{X}_0$ (an estimate of this set can be obtained

considering a worst case scenario).
All that being given, after some computation following the approach presented in [57], the matrix K minimizing oscillations can be computed solving the following convex, LMI-constrained, optimization problem

$$\begin{aligned}
&\min_{Q=Q^T>0,\delta>0,Y,Z} \delta, \text{ subject to} \\
&C^T Q C \leq \delta I_4 \\
&QF_k^T + F_k Q + GD_i Y + GD_i^- Z + Y^T D_i G^T + Z^T D_i^- G^T < 0 \\
&\begin{bmatrix} Q & Z_j^T \\ Z_j & v_{jmax}^2 \end{bmatrix} \geq 0 \; j = u, v, \; Q - R^{-1} \geq 0.
\end{aligned} \tag{4.15}$$

with $Y = KQ$, $Z = HQ$, while Q, R are positive definite symmetric matrices defining invariant ellipsoids containing $\tilde{x}_a$ trajectories and the set $\mathcal{X}_0$, respectively.
In brief, the first constraint expresses (by Schur complement) the fact that trajectories starting in $\mathcal{X}_0$ have a peak bound $\|\tilde{x}\| \leq \sqrt{\delta}$, guaranteed by an invariant ellipsoid defined by matrix Q. The second set of constraints enforces system asymptotic stability inside the aforementioned ellipsoid, while constraints in the third row, ensures the invariant ellipsoid lies in the region where (4.14) holds true, and it includes the ellipsoid defining/approximating set $\mathcal{X}_0$.
The optimal state feedback, giving minimal peak δ^* for error variables $\tilde{x}$ can be retrieved by the solution of (6.9) as $K^* = Y^* Q^{*-1}$.
Note that problem (6.9) can be solved offline, assuming a worst case scenario for $\tilde{x}_a$ initial conditions. Along with fixed bounds ξ_{jmax} for the feedback components, this makes the solution suboptimal w.r.t. what could be obtained with on-line optimal control (such has MPC). However, low computational burden is required, making its implementation easy, and sustainable for standard embedded computational platforms used for the considered applications. In addition, as it will be shown in Section 4.5, satisfying LVRT performance can be ensured, indicating a not critical loss in optimality. The block scheme of the proposed solution, combining all the units designed in this Section is summarized in Fig. 4.4.
Again, it is worth to remark the role natural modes free flux references generation (by eq. 4.4), which enter the feedforward part. Combined with the optimally tuned feedback part, this allows to avoid rotor overcurrent, also under hard unbalanced faults, thus keeping the system connected, but also improving state reference tracking, and thus LVRT performance. In turn, also the variables T and i_{1v} will exhibit a smooth behavior; torque reduction during the dip will not induce relevant mechanical stress on the wind turbine, and accurate reactive current injection, close to i_{1v}^*, can be ensured. Such features are assessed in the next Section via extensive numerical simulations.

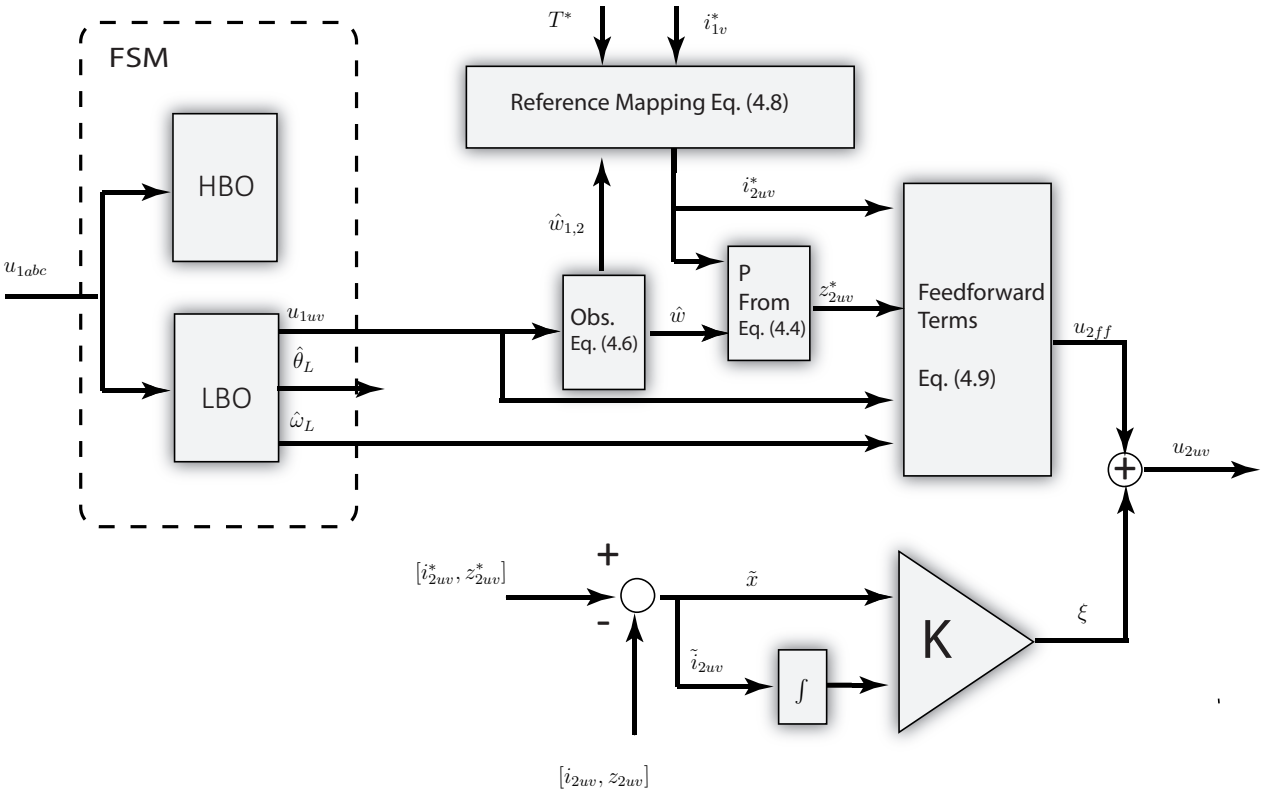

Figure 4.4: Overall block scheme of the proposed RSC control unit.

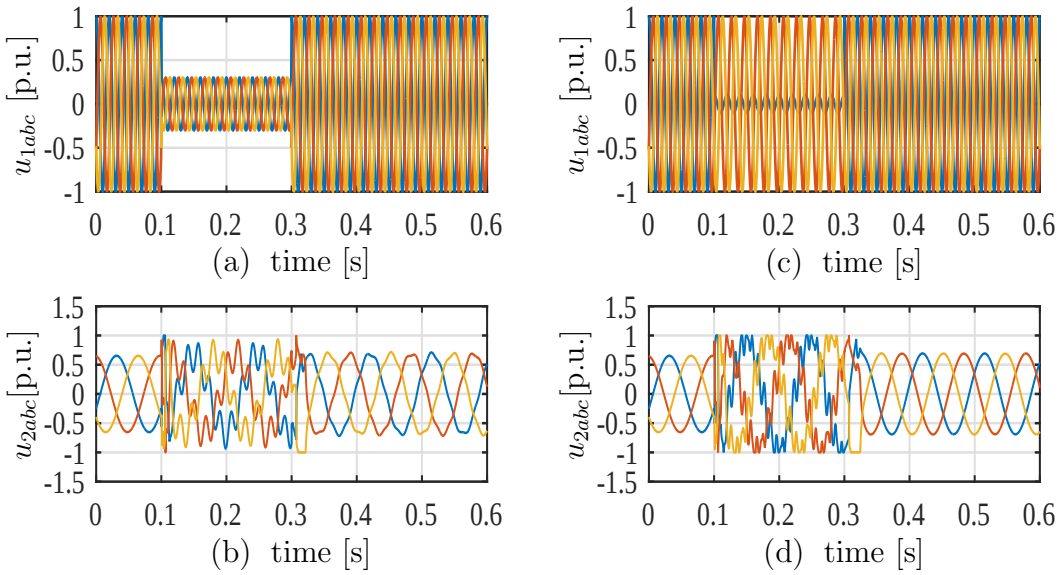

Figure 4.5: Results of the studied system under a 70% symmetrical fault, left column, plots (a)-(b), and under asymmetrical 90% single phase dip, right column plots (c)-(d).
(a)-(c): Stator voltages. (b)-(d): Rotor voltages.

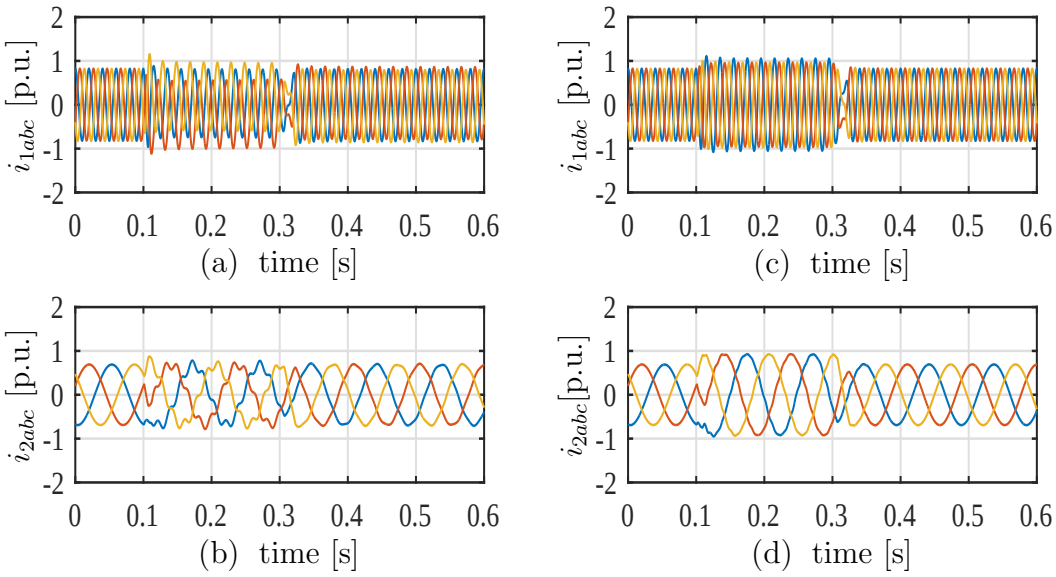

Figure 4.6: Results of the studied system under a 70% symmetrical fault, left column, plots (a)-(b), and under asymmetrical 90% single phase dip, right column plots (c)-(d).
(a)-(c): Stator currents. (b)-(d): Rotor currents.

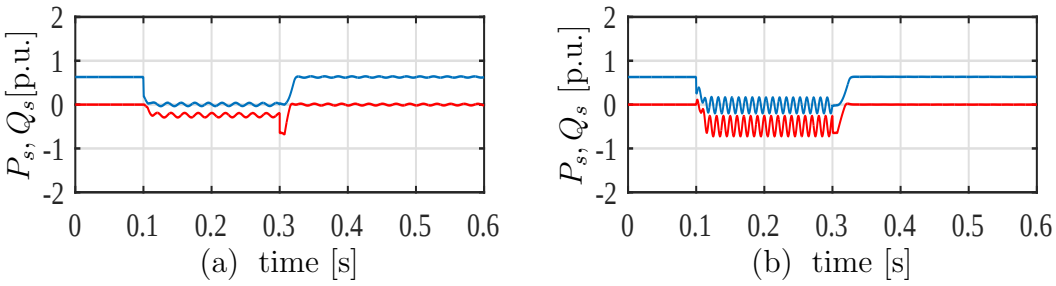

Figure 4.7: Stator-side active and reactive powers of the studied system under a 70% symmetrical fault, left column, and under asymmetrical 90% single phase dip, right column.

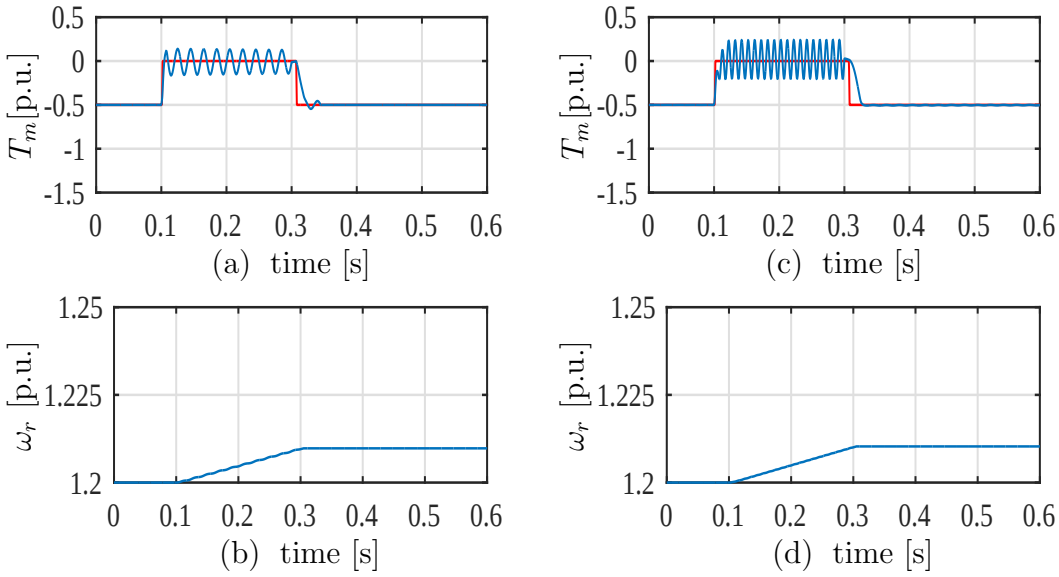

Figure 4.8: Results of the studied system under a 70% symmetrical fault, left column, plots (a)-(b), and under asymmetrical 90% single phase dip, right column plots (c)-(d).
(a)-(c): Electromagnetic torque. (b)-(d): Rotor angular speed.

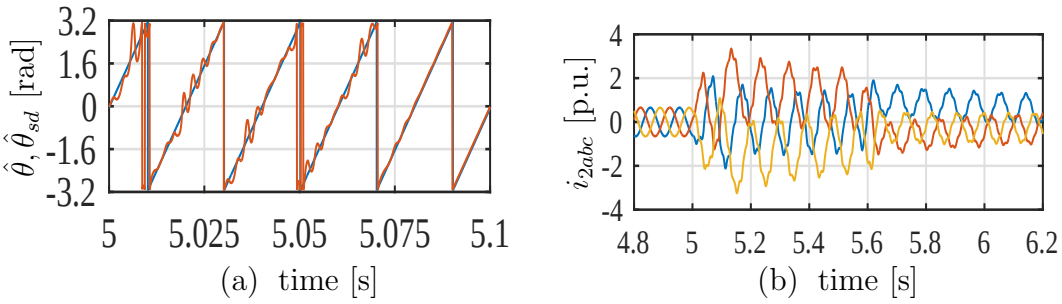

Figure 4.9: Performance of delayed signal cancellation angle reconstruction method, under the considered unbalanced dip. (a) comparison between the proposed open-loop angle forward projection (blue) and delayed signal cancellation estimate (red). (b) rotor currents obtained with delayed signal cancellation reconstruction, and the proposed control solution.

4.5 Simulation Results

In order to assess the performance of the proposed control solution, a $50Hz$ $1.5MW$ DFIG, characterized by the parameters reported in Tab.A.2, has been considered as case study. A controller in the form (6.7), with saturated feedback terms ξ_u, ξ_v, tuned according to the LMI-based procedure, outlined in the previous Section, has been designed. A discrete time version both of the controller, given by eq. (4.9)-(6.7)-(4.11), and the observers in (4.6), (4.7), has been implemented, using standard backwar Euler discretization method. In addition, a switching RSC driven by a $2.5kHz$ PWM technique has been considered. The discretization sampling time has been set equal to the PWM carrier period. The following parameters have been considered to solve problem (6.9): $\xi_{jmax} = u_{2jmax}/2,\ j = u, v$, $\omega_r(t) \in [0.7\omega_{nom}, 1.3\omega_{nom}]$, with $\omega_{nom} = 2\pi 50 rad/s$ the synchronous speed of the $50Hz$ machine. In order to represent the set of initial conditions for $\tilde{x}_a$ $R = diag(\tilde{z}_{2u}^{-2}, \tilde{z}_{2v}^{-2}, \tilde{i}_{2u}^{-2}, \tilde{i}_{2u}^{-2}, \tilde{\chi}_{2u}^{-2}, \tilde{\chi}_{2v}^{-2})$, where $\tilde{z}_{2u} = 0.3Wb, \tilde{z}_{2v} = 0.93Wb$, $\tilde{i}_{2u} = 200A$, $\tilde{i}_{2v} = 200A$, $\tilde{\chi}_{2u} = 20As$, $\tilde{\chi}_{2v} = 20As$ have been conservatively set according to the estimated tracking error jumps during the dip described in Fig. 4.1. The resulting feedback matrix is $K^* = \begin{bmatrix} 419.9 & -58.7 & 2.7 & -0.017 & 1.67 & 0.018 \\ 99.8 & 184.9 & -0.067 & 1.93 & -0.004 & 0.016 \end{bmatrix}$. For what concerns the polar coordinate observers (4.7), the following gains have been set, LBO: $k_1 = 9.5$, $k_2 = 2$, $\gamma = 3850$; HBO: $k_{1F} = 150$, $k_{2F} = 15$, $\gamma_F = 1500$, which, according to tuning rules in [65], correspond to bandwidth equal to $9Hz$ and $300Hz$, respectively. For observer (4.6), the following output injection matrix has been chosen $L = \begin{bmatrix} -628.3 & 0 & -89.9 & 13.3 \\ 0 & -628.3 & -13.3 & -89.9 \end{bmatrix}^T$, providing a bandwidth of $70Hz$. Finally, the parameters used in the finite state machine are $\bar{k} = 15V,\ \bar{k}_1 = 15V,\ \bar{t} = 2s,\ \bar{t}_1 = 5ms,\ \bar{t}_2 = 20ms$.

With these settings, several numerical tests have been carried out. First, comparisons with a significant, recently proposed method in [28], relying only on control to sustain also asymmetrical dips have been performed. To this aim, the same machine parameters (reported in Tab. A.2), operating conditions (mechanical power, torque, rotor speed), and fault scenarios have been replicated. The machine is made to operate in generator mode, with an input mechanical power equal to 67% of its rated value, and keeping a speed equal to 120% of the nominal value. Then, at $0.1s$ a grid fault lasting $200ms$ is emulated. As mentioned in Section 4.3, two dips have been considered as in [28]; a 70% symmetric sag, and a 90% single-phase fault. When the dip is detected the torque reference is decreased to zero, however, differently from what in [28], no waiting time after the dip clearance detection is applied to bring back the reference to the previous value. Furthermore, the amount of stator

reactive current (required to sustain the grid voltage by injecting capacitive power in the mains [15], [16]), is set according to the sag depth (estimated via the HBO), independently from other controller parameters. In contrast, in [28] the stator reactive current/power is related to a controller constant (called "tracking gain") set to reduce the machine rotor flux during the fault, thus combination other reactive power support strategies could be needed.

The simulation results corresponding to the two aforementioned scenarios are shown in Figs. 4.5-4.8. Starting with the symmetric dip case, shown in the left column, and comparing it with Fig. 7(a) in [28], it can be seen how, while both the methods ensure rotor currents to stay below the critical value of 2 $p.u.$[4], much smaller oscillations are ensured with the proposed technique. Indeed, the peak rotor currents value during the fault does not exceed 1 $p.u.$ (see Fig. 4.6 (a)). Stator currents (in Fig. 4.6 (a)) are limited as well, while voltage saturation occurs, particularly at the beginning and the end of the dip (see Fig. 4.5 (b)), but, thanks to the proposed LMI-based tuning, it is correctly handled ensuring a suitable machine behavior. Also the stator active and reactive power, portrayed in plot 4.6 (f), exhibit a smooth profile. It is further to note the spike in the reactive term during the dip recovery stage. This phenomenon is due to the sudden increase in the line voltage, which cannot be instantaneously detected, nor perfectly tracked by the observer (4.6). Then, the reactive current reference is reduced with a delay w.r.t. the line voltage recovery, resulting in a temporary reactive power increase. As concerns torque (Fig. 4.8 (a)), a decreasing oscillation at ω_L can be seen during the sag. Such ripple is higher w.r.t. the one in [28], however, it does not affect the generator speed (in Fig. 4.8 (b)), which increases less than in [28] due to the prompt restore of the torque immediately after the fault. The reason for such oscillations lies in the feedback terms design, which, putting most of the (saturated) effort in avoiding rotor overcurrent, lets the stator variables (fluxes and currents) to slowly converge to the steady state references (computed in Subsection 4.4.1).

Similar reasoning applies for the single phase fault shown in the right column of Figs. 4.5-4.8. Again, comparing rotor currents with results in Fig. 9 of [28], a considerable improvement can be noted. In addition, the steady state sinusoidal regime is restored much faster after the dip clearance. The key point for achieving such results is the trajectories planning (4.5), and the corresponding feedforward terms in (4.9). In fact, this solution goes beyond a simple reduction of the machine flux, by managing explicitly the counter rotating components, related to asymmetrical faults, thanks to the design of natural oscillation-free (DC-free in three phase stationary frame) zero dynamics trajectories. Again, slightly higher oscillations are present on torque

[4]Typically the RSC electronics is sized to withstand peak currents up to double the rated machine value for small time periods.

signal, this time at $2\omega_L$ and settling to a constant amplitude throughout the whole dip (see Fig. 4.8 (c)). The permanent oscillation around the reference is due to the approximated mapping, remarked at the end of Subsection 4.4.3, while transient response stems from the aforementioned feedback design. The effects of such tuning are underscored also by the stator currents waveforms during the unbalanced fault (Fig. 4.6 (c)). A slowly vanishing DC component arises in the stator currents, while rotor ones do not have such shape. Again, this is the consequence of the control choice to keep the rotor currents tightly close to their references, while letting the unbalancement (natural modes oscillations in the SVO frame) to affect more the, less critical, stator variables. Later on it will be shown how such strategy is crucial to prevent rotor overcurrent under challenging faults like the one described in Fig. 4.1.

Another important feature which allows the presented approach to cope with harsh dips is the detection and line angle reconstruction based on the state machine and the observers discussed in Subsection 4.4.2. To motivate the need for such structure combined to our control solution, a standard, quite popular angle reconstruction method for LVRT (adopted in ([28],[27]), based on the so called *delayed signal cancellation* [66], has been used under the fault portrayed in Fig. 4.1. The obtained results are reported in Fig. 4.9. It is clear how, if the positive sequence angle estimated by delayed signal cancellation is used in place of the open-loop integration (from the last not faulty point of the PLL observer), the controller performance are lost, as highlighted in the rotor currents signals in Fig. 4.9 (b). Indeed, during the harsh transients, with overshoots and bounces, a non sinusoidal line regime arises, impairing the key assumption of the delayed signal cancellation reconstruction method. As a result, the estimated angle shows oscillatory behavior with abrupt jumps (see Fig. 4.9 (a)).

Instead, if the proposed dip detection and voltage estimation scheme is used to feed the controller, a more graceful behavior, compliant with the system current limits, is obtained, as proved by results in Fig. 4.10. Rotor currents (in Fig. 4.10 (d)) are still well below 2 $p.u.$ (less then 1.5 $p.u.$). Due to the harsher nature off the fault, more control effort w.r.t. the unbalanced case in Fig. 4.5 is required to tame the rotor currents, and saturation occurs more frequently throughout the entire dip (see Fig. 4.10 (e)). The line estimate and dip detection mechanism are clarified by Figs. 4.10 (m), (n). In plot (m), it is highlighted how the dip is detected by LBO, leading to a permanent estimation error during the dip, due to disabling the observer adaptation. Differently, in plot (n), the HBO is kept operating, estimating the line also during the fault, and allowing the dip clearance detection. Note that, while the line amplitude bounces and overshoot are sensed by the HBO, the logic defined in scheme 4.3 prevents the LBO reconnection during the fault, allowing to restore this

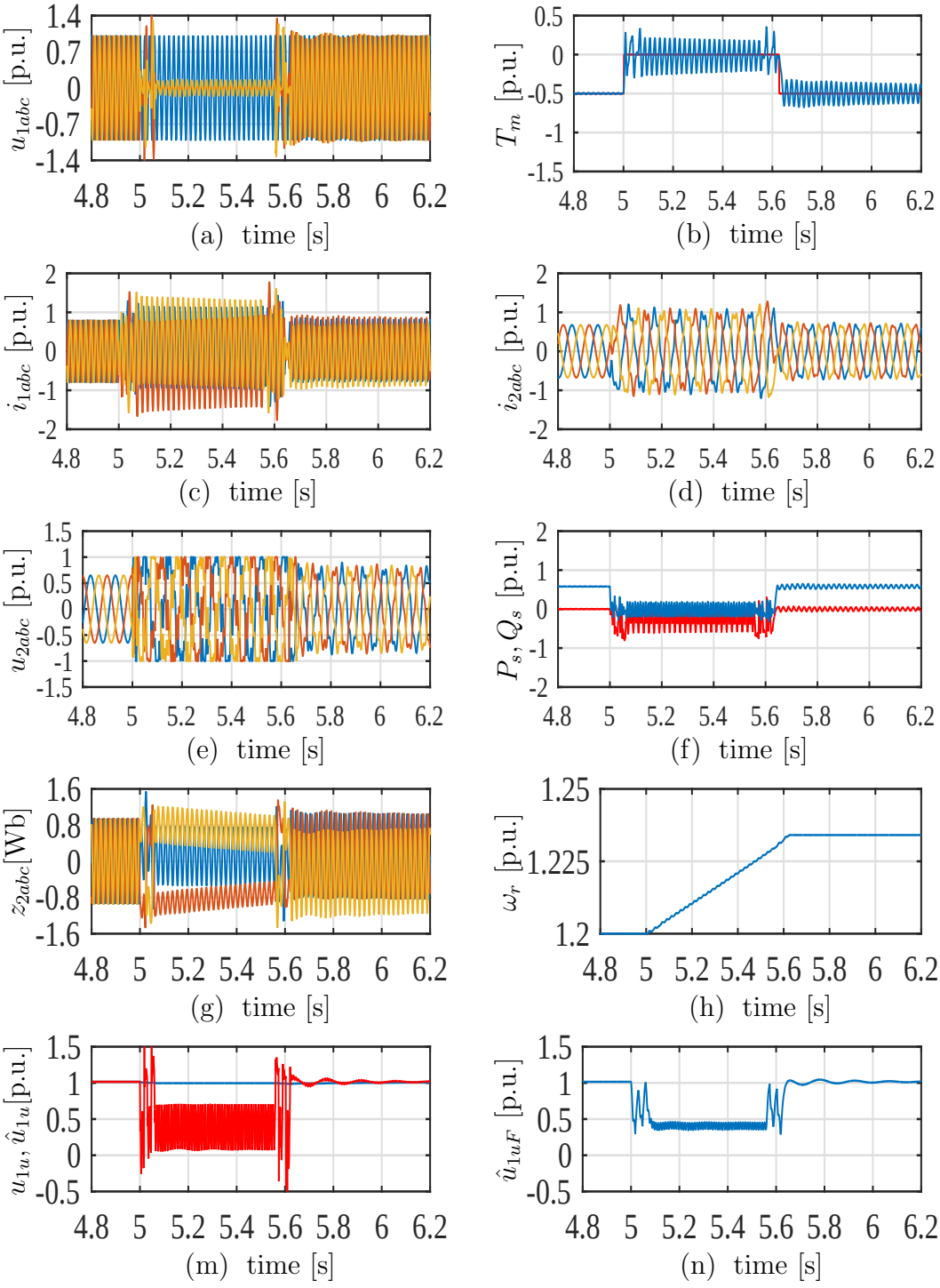

Figure 4.10: Results of the studied system under the considered two-phase unbalanced fault. (a) Faulty stator voltage (b) Electromagnetic torque. (c) Stator currents. (d) Rotor currents. (e) Rotor voltages. (f) Stator active (blue) and reactive (red) power. (g) Stator fluxes. (h) Rotor speed. (m) Stator voltage u-component (red) and LBO estimate (blue). (n) Estimated stator voltage u-component by HBO.

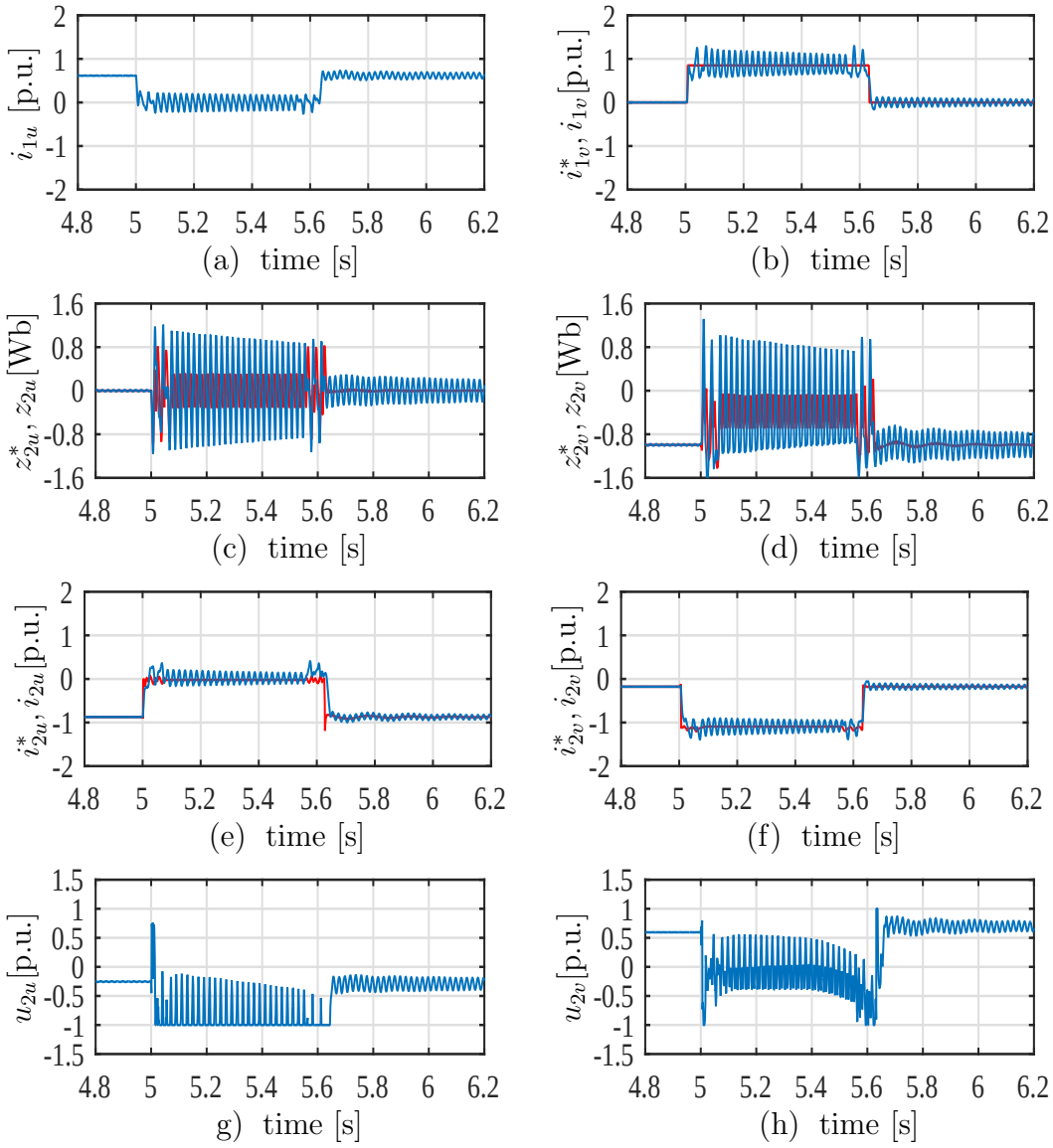

Figure 4.11: Results of the studied system under the considered two-phase unbalanced fault, signals in the $u - v$ SVO framework. (a) Stator current u-component. (b) Stator currents v-component reference (red) and measured (blue). (c) Zero dynamics (stator flux) u-component reference (red), and measured (blue). (d) Zero dynamics v-component reference (red) and measured (blue). (e) Rotor currents u-component reference (red) and measured (blue). (f) Rotor currents v-component reference (red) and measured (blue) (g) Rotor voltage u-component. (h) Rotor voltage v-component.

observer only after the actual dip clearance. Even in this case $2\omega_L$ oscillations are present on torque and power signals (see Figs. 4.10 (b) and (f)). Here, the effect of "pushing" the unbalancement onto the stator variables is even more evident w.r.t. the (milder) asymmetric fault of Figs. 4.5-4.8. Indeed, looking at stator currents and fluxes in Figs. 4.10 (c), (g) respectively, it can be noted how a DC component arises at the beginning of the dip, and tends to decrease with a quite slow rate (mostly given by constant α_1 for the fluxes). In order to further clarify the behavior of the presented solution, signal in the SVO $u-v$ frame have been reported, along with the respective references, in Fig. 4.11. It is clear how the control favors rotor currents (Fig. 4.11 (e), (f)) which track the references quite closely, with limited oscillations. Instead, the stator fluxes convergence to the natural-modes-free references is slower (see Figs. 4.11 (c), (d)). Stator currents in Figs. 4.11 (a), (b) also have larger oscillations w.r.t. the rotor ones. As mentioned, this is a necessary trade-off for making the system to survive challenging faults with the limited control authority given by the RSC voltage limitation.
To further validate the proposed solution, the same test as in Figs. 4.10, 4.11 has been repeated, considering noisy measurements and parametric uncertainties. In this respect, zero-mean white Gaussian noises with standard deviation equal to 3% of nominal values, have been added to the measured signals. Furthermore, stator and rotor resistance values have been increased by 75%, while inductances L_1, L_2, L_m have been decreased by 30%. Fig.4.12 shows the corresponding results. Despite some slight fluctuations due to noisy measurements, particularly in the control action (see Figs. 4.12 (g)-(h)), the control objectives, fulfilled in the previous tests, are again substantiated. It is further to remark that rotor currents asymptotic tracking is ensured in spite of parametric mismatch, thanks to the feedback integral terms.

4.6 Conclusions

In this chapter, the challenging problem of endowing doubly-fed machines with LVRT property under sever asymmetric voltage dip has been tackled by means of advanced system theory and control tools. A careful system analysis has allowed to define natural-modes-free trajectories for the system internal dynamics, which are directly affected by line faults. Building on this result, a suitable feedforward action has been designed, and completed with a saturated state feedback part, providing additional oscillations damping and robustness. In addition, a dip detection scheme, based on suitable line observers, has been designed. This strategy has been tested via realistic numerical simulations, and proved to be capable of handling harsh unbalanced line faults, not considered before in the literature. Such characteristics make it a promising solution for achieving LVRT in DFIG-based wind energy systems,

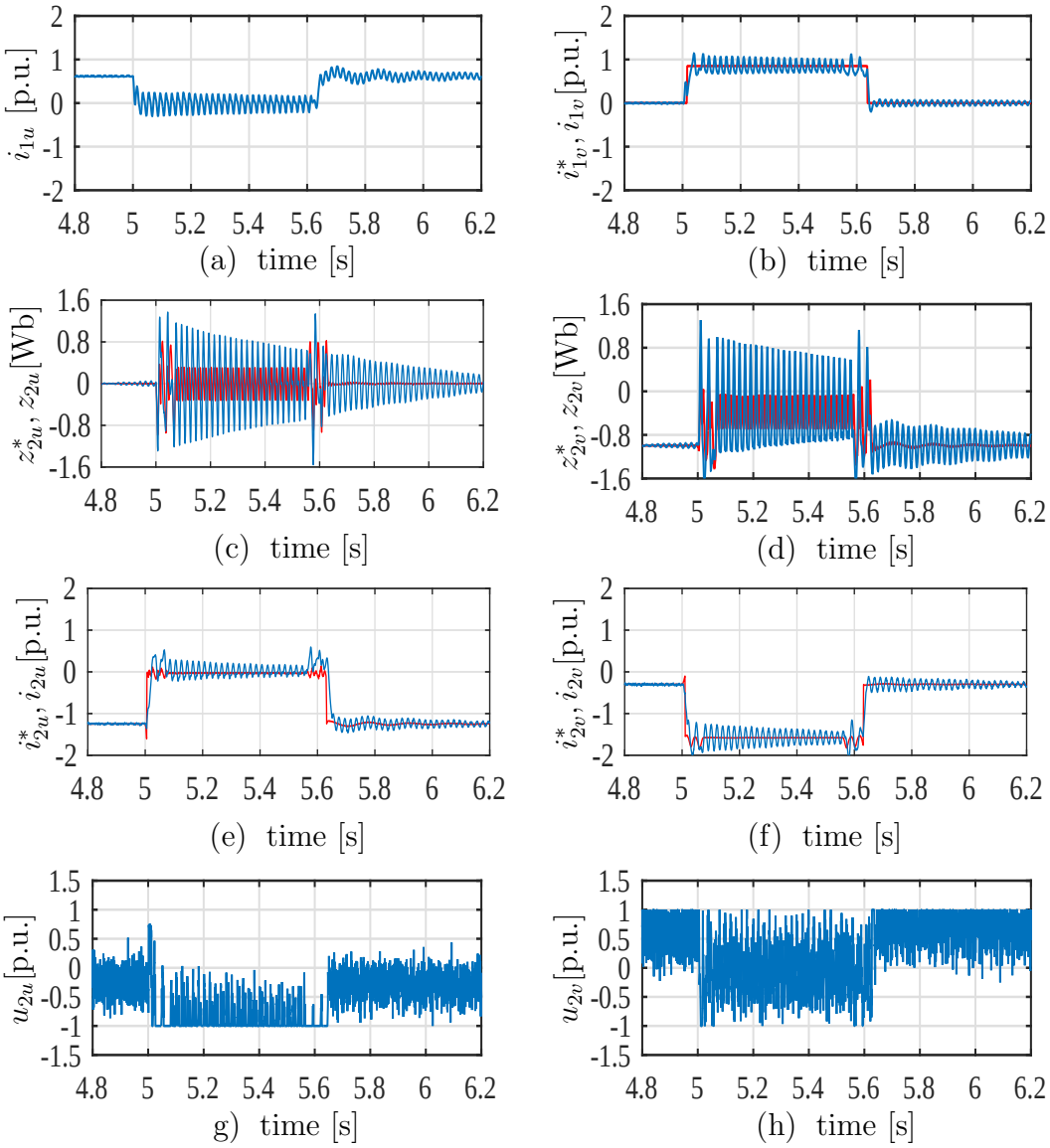

Figure 4.12: Results of the studied system under the considered two-phase unbalanced fault with noisy measurements and machine parameters uncertainties. Signals in the $u-v$ SVO framework. (a) Stator current u-component. (b) Stator currents v-component reference (red) and measured (blue). (c) Zero dynamics (stator flux) u-component reference (red), and measured (blue). (d) Zero dynamics v-component reference (red) and measured (blue). (e) Rotor currents u-component reference (red) and measured (blue). (f) Rotor currents v-component reference (red) and measured (blue) (g) Rotor voltage u-component. (h) Rotor voltage v-component.

with minimal (ideally null) help of auxiliary protection hardware.

Chapter 5

Trajectory Design for after-dip Restore in Wind Turbines

5.1 Introduction

As outlined in the previous chapters, the global cumulative installed wind capacity has been exponentially increasing for the past two decades, reaching 430 GW at the end of 2015 [67]. Such trend is due to both an augmentation in the number of installed wind energy conversion systems (WECSs) and in their power size, making wind turbines (WTs) critical sources for modern power grids. As a result, more demanding regulations about the operation of such systems have been issued, requiring, in turn, sophisticated control methods in order to be met.
In this respect, beside the standard goal to keep the WECS working within some power, generator torque, and speed limits, extracting the maximum power from the wind whenever possible (i.e. up to the rated power of the electric generator drive), two crucial aspects need to be tackled: I) Dealing with line voltage dips, II) Suppressing mechanical vibrations.
As regards the first goal, it was explained that given the aforementioned pervasive penetration of WECS into nowadays power networks, national grid codes and regulations have been updated and specifically tailored to such systems, demanding the so called Low Voltage Ride Through (LVRT) capability (see [68], [69] and references therein for a comprehensive overview of international regulations specifications). As discussed in the Ch.2, the main negative effects of voltage dips on WECSs were the surplus generated power (compared with the delivered one) and the large oscillations triggered by the voltage perturbation in the DFIG's internal dynamics. Several solutions have been proposed in the literature to tackle the aforementioned problems from the electrical viewpoint, and endow WECSs with LVRT property. In [32], [31], and [35] some of them are reported.

For what concerns vibrations in the turbine mechanical structure, owing to large loads and dimensions of nowadays turbines, they cause relevant fatigue stresses which significantly shorten the system lifetime, and, in some cases, can lead to damages [47]. Therefore, a proper damping of mechanics oscillatory modes need to be guaranteed. To this aim, advanced control strategies have been proposed, mainly focusing on the drivetrain torsional vibrations, which, owing to rather low frequency, lightly damped, resonant modes, are the most critical ones [42]. A popular approach is based on linearization around the working point/trajectory and exploit advanced gain scheduling methods [70], [71], [43]. In [44] a nonlinear state feedback speed controller has been proposed, with filters on the reference and control input (the generator torque) to prevent the drive train resonant mode excitation, while in [72] a nonlinear model predictive controller has been used. Regardless of the specific solution, in general, a High-Bandwidth-Feedback control (referred as HBF, for brevity) is needed for a strong damping injection, minimizing the drive train torsional oscillations. Such feedback controller has to act on the generator torque, which can be changed with the required bandwidth. Indeed, while nowadays turbines are typically equipped with variable pitch blades, this control knob cannot be used for damping injection, since it is subject to strict rate of change limits, due to the large blade inertia and low bandwidth of the actuation system.
Actually, mechanical vibration suppression is affected by voltage dip management. As mentioned before, generator torque has to be removed (or highly reduced) during the line voltage sags, since there is no room for a reliable power exchange with the grid (voltage amplitude is close to zero and highly fluctuating). Therefore the high bandwidth controller need to be quickly turned off during the fault. Consequently, turbine speed will increase and some oscillations will arise in the drivetrain. These phenomena are usually disregarded in the state feedback design because the turbine inertia and the fault duration are assumed to be respectively large and short enough (tens of milliseconds) to give just a minor change in the WT state with respect to the pre fault condition. Then, after the dip clearance, the feedback controller, devoted to drivetrain strong damping, is just turned on again, assuming it can recover smoothly the nominal steady state condition. Actually, in practice, it can take seconds before the line voltage is restored and stabilized within its nominal range [73], as it is acknowledged by some grid codes [16]. Since it is reasonable to switch on the state feedback controller only when the line has been safely restored, i.e. at the very end of dip profile, the system can end up in a status which is quite far from the pre-fault working point. This fact, combined with the abrupt turn on of a high bandwidth feedback algorithm, can lead to torque saturations, and, in turn bad behavior in the turbine speed, and drivetrain state. Taking the cue from this considerations, it is necessary to formulate and solve a new control problem in order

to preserve the HBF controller also after the dip clearance and, at the same time, prevent bad system behavior, and torque saturation. Such control problem can be outlined as: just after the voltage dip, restore the original steady-state condition in minimum time, without violating torque limits and triggering oscillations. There exist powerful techniques, to cope with this kind problem, in particular, Model Predictive Control (MPC) has become the standard modern framework to approach constrained optimal control [74]. However, MPC is computationally heavy in its standard formulation, as it requires the on-line solution of constrained optimization problem. If explicit MPC [75] can be applied, then the bottleneck can be the memory usage.

Bearing in mind these considerations, in this chapter, we propose a different solution, specifically tailored to the WT application, with the following purposes: to have a very "low footprint" in terms of computational time and memory usage at run time, and to be easily joined as an add-on for the HBF controller. Such solution is based on a state trajectory design that, accounting for the system structural property and physical limits, ensure a suitable reference smoothness and a minimum recovery time to the nominal steady state after the dip. The optimization problem naturally stemming from minimum time requirement is solved offline for different boundary conditions after the dip clearance, and a low-size lookup table and interpolation are used on-line to get the trajectory corresponding to general post fault scenarios. This ensures low complexity at run time, and easy combination with state feedback, since the reference trajectory can be used to generate feedforward actions, and feed the HBF controller, which in this work is based on pretty standard linearization and pole placement techniques.

Similar to other works in the literature [42], [43], [44] a two-mass model is adopted to capture the WT crucial mechanical behavior. The WT mechanical and aerodynamics models which will be used for control purposes, were detailed in Section 1.3 of the first chapter. The substance of this chapter, published in [76] is structured as follows: In Section 5.2 the twofold control problem combining the basic HBF objective based on pole placement and the after-dip recovery management is formulated. In Section 5.3, first it is shown the system unstable behavior after the line fault, if just standard state feedback configuration is used. Then, the proposed trajectory planning is presented in detail. Finally, simulation results, validating the proposed control strategy, are provided and discussed in Section 5.4. Particular attention will be paid to parametric uncertainties, which could affect the model based trajectory planning. Section 5.5 ends the chapter with some final remarks.

5.2 Problem Statement and Objectives

As mentioned before, recent grid codes specify LVRT capability for WECSs, demanding the system to remain connected to the grid for classes of faults characterized in terms of voltage reduction and duration. German E.ON Netz regulation requiring WT to ride through 85% voltage shortage lasting $625ms$ [77], and American FERC asking to face a 100% voltage drop lasting for a maximum of 9 *cycles* (around $150ms$) [31], were two examples detailed in the Ch.2. However, the restoring of grid voltage nominal value, usually lasts longer (around $1s$ [73]). From a power exchange perspective, it is profitable to limit the generator power injection, i.e. keeping the torque low, until the fault effects have completely vanished, and the grid is back to a stable condition. Therefore, in this chapter a worst case 100% voltage drop, completely cleared after $1s$ will be considered for the controller design. In this context, the control objectives can be summarized as:

1. Assuming full state information, establish a HBF controller, based on linearization about the current working point and standard pole placement, to impose fast enough real poles, suppressing torsional oscillations, and ensuring safe performance of the drivetrain to increase the WT life time.

2. Whenever a grid fault occurs, guarantee the minimum time after-dip recovery, preserving HBF controller, without violating torque constraints.

Although both generator torque T_g and pitch angle β can be used to control modern variable speed variable pitch turbines, the natural control input to achieve the goals above is T_g, since it can be changed with a high bandwidth compliant with the oscillations damping requirement. On the other hand, blade pitching requires many seconds due to the actuation slow dynamics and the blade size. Thus, it is common to exploit β only for off-nominal or emergence conditions, including an external feedback loop to ensure reliable and safe turbine operation in any case. Owing to space constraint the outer control loop design will not be elaborated, focusing on objectives 1)-2).
As control design guideline, the idea is to start from standard feedback solutions for objective 1), then add a sort of plug-in unit devoted to objective 2). An additional requirement is to keep the plug-in unit as light as possible both from computational burden and memory footprint viewpoints. In this way, the control algorithm can be easily implemented in medium-end embedded system. For this reason, possible solutions based on dynamic programming and MPC are avoided, since they would enforce heavy computational/memory burden.

5.3 Proposed Control Strategy

The key novel part of the proposed solution is to fulfill objective 2), defined in Section 5.2, by plugging a suitable trajectory planning in the system equipped with the a standard HBF control based on pole placement. Such trajectory planning has to: ensure feasibility of the reference according to the system structural properties, comply with the generator torque bound, guarantee a minimum time profile towards the steady-state pre-fault condition. The last (minimal time) specification implies an optimization problem has to be solved. Thus, to keep the on-line complexity low, the trajectory has to be defined offline. However, the system state at the fault clearance point, which clearly would be the starting point of the state reference, depends on the dip nature and cannot be fully known in advance. Similar reasoning holds for the final point of the reference trajectory, which, being the optimal power point, clearly depends on the current wind speed. To manage this issue, a set of suitable trajectories, corresponding to some anticipated reasonable initial states and wind speed values, is computed offline. Then, in order to generate trajectories for the actual after fault conditions, interpolation among the offline computed set can be used at run time. Indeed, it will be shown later how some features of the system can be exploited to preserves feasibility, i.e. the interpolated signals do not cause any torque saturation.
In the following, the HBF state feedback controller is designed first, then the trajectory planning is presented.

5.3.1 State Feedback Controller

In order to deal with objective 1) in Section 5.2 a simple linear state feedback solution is considered. To this aim, system (1.25) can be linearized about its steady state defined by:

$$\theta^*_{dss} = \frac{T_w(\omega^*_{tss},\beta,V_w)}{K_s},\ \frac{\omega^*_{gss}}{n} = \omega^*_{tss} = \omega_{t-opt}(V_w),\ T^*_{gss} = \frac{K_s\theta^*_{dss}}{n}. \tag{5.1}$$

Clearly ω_{t-opt} varies with the current wind speed, however, a set of working conditions can be considered and gain-scheduling techniques can be applied to adapt the state feedback law to the actual system conditions.[1] Now, defining the error signals $\tilde{\theta}_d = \theta_d - \theta^*_{dss}$, $\tilde{\omega}_t = \omega_t - \omega^*_{tss}$, $\tilde{\omega}_g = \omega_g - \omega^*_{gss}$, and augmenting the system with the integral term $\tilde{\omega}_{tI} = \int \omega_t - \omega^*_{tss}$, in order to provide some robustness and ensuring the optimal turbine speed is reached in face of parametric uncertainties, the augmented

[1] From a practical viewpoint state feedback matrix could be stored in a lookup table and interpolation can be used similarly to what mentioned for the trajectory planning.

system linearized error dynamics can be expressed as

$$\begin{bmatrix} \dot{\tilde{\theta}}_d \\ \dot{\tilde{\omega}}_{tI} \\ \dot{\tilde{\omega}}_t \\ \dot{\tilde{\omega}}_g \end{bmatrix} = \underbrace{\begin{bmatrix} 0 & 0 & -1 & \frac{1}{n} \\ 0 & 0 & 1 & 0 \\ \frac{K_s}{J_t} & 0 & \frac{K_w^* - D_s}{J_t} & \frac{D_s}{nJ_t} \\ \frac{K_s}{nJ_g} & 0 & -\frac{D_s}{nJ_g} & \frac{D_s}{n^2 J_g} \end{bmatrix}}_{A} \underbrace{\begin{bmatrix} \tilde{\theta}_d \\ \tilde{\omega}_{tI} \\ \tilde{\omega}_t \\ \tilde{\omega}_g \end{bmatrix}}_{\tilde{x}} + \underbrace{\begin{bmatrix} 0 \\ 0 \\ 0 \\ -\frac{1}{J_g} \end{bmatrix}}_{B} \Delta T_g \tag{5.2}$$

where $K_w^* = \frac{\partial T_w}{\partial \omega_t}|_{\omega_{tss}^*, V_w, \beta}$ and $\Delta T_g = T_g - T_{gss}^*$. Then, a state feedback law $\Delta T_g = K\tilde{x}$ can be designed for the system above, ensuring the closed loop state matrix $A + BK$ is Hurwitz and with real eigenvalues providing the required bandwidth to steer the system towards the desired equilibrium, and strongly damp vibrations in the drivetrain[2].

5.3.2 Trajectory Planning

Before presenting the trajectory planning, its necessity is proven by showing some simulations, applying the above-considered standard feedback controller which is switched off during the fault to reset the torque command, and restored right after the dip clearance. The HBF controller has been applied to a 0.5MW variable speed horizontal axis WT characterized by the parameters reported in Tab. A.3, leading to a resonance frequency of about 1Hz. A constant wind speed $V_w = 10m/s$ is emulated, for which the considered turbine can extract the maximum wind energy without torque/power saturation, thus with no pitching ($\beta = 0$). For this nominal condition, the state feedback matrix $K = [-0.047 - 0.256 - 0.0008 - 2.619] \times 10^{10}$ has been designed according to what presented in Subsection 5.3.1, placing the linearized system poles at $[-5 - 6 - 7 - 9]Hz$ (i.e. at least five times faster w.r.t. the drivetrain resonant frequency). With the system at the corresponding optimal equilibrium (with $\omega_{t-opt} = 3.329\ rad/s$) a symmetric fault type A according to ABC classification detailed in Section 2.2, causing voltage drop in the grid, has been reproduced, to evaluate the performance of the controller against such kind of events. In Fig. 2.1 a typical power systems voltage dip was portrayed, consisting of three different stages: falling, stabilizing, and recovering [33]. In the simulation tests, a 100% voltage amplitude reduction has been emulated, with $20ms$ for falling and $1.02s$ for the stabilizing and recovering stages.

Fig. 5.1 show results under the aforementioned state feedback control law, saturated as $|T_g^* + K\tilde{x}| \leq T_{gmax} = 2T_{gnom}$ (rated value T_{gnom} is reported in Tab. A.3) in

[2] Clearly, the electrical dynamics bandwidth of the controlled generator has to be considered in setting the above poles, since the T_g command has to be effectively tracked by the actual generator torque.

order to comply with generator torque limits. As expected (see Section 5.1), at the end of the dip (lasting from $t = 5s$ to $6.02s$), when the HBF controller is switched on again, a large generator torque, beyond the system limit, is requested, therefore heavy saturation occurs (see Fig. 5.1(c)). As a consequence all the turbine states experience large unstable oscillations, as shown in Figs. 5.1 (a),(b),(d). This behavior gives evidence of the need for suitable countermeasures to explicitly handle after fault recovery under control input limitations.

As introduced at the beginning of this Section, the main idea is to design a suitable state reference trajectory, ensuring the system is steered back to the optimal steady state point in minimum time and with no torque constraint violation. In this respect, a feedforward term, based on the defined reference, will be joined (summed) to the HBF controller to achieve tracking of the trajectory.

The first step for state trajectory design is a suitable elaboration of system (1.25). To this aim, following a systems theory based approach, the ensuing procedure will be carried out:

- Considering the turbine speed as the controlled output variable (complying with the mentioned objectives), model (1.25) will be represented in standard normal form [40]. This allow to highlight, the "smoothness level" a state trajectory needs to have to be feasible for the system. By functional controllability arguments, we define smoothness level as the number of finite derivatives which is needed for a trajectory to be feasible, according to the given system dynamics and assuming a possibly discontinuous, arbitrarily large, but bounded input (in this case the generator torque);

- With the results of the item above at hand, the torque command which is needed to steer the system along a given feasible trajectory can be computed by left-inverting the system in normal form.

Starting with the first point, it is easy to verify that system (1.25) has relative degree two from input T_g to output ω_t. Then, selecting turbine speed and its derivative as states, and leaving θ_d unchanged to complete the new state vector, the considered system normal form can be written as (5.3).

$$\begin{bmatrix} \dot{\omega}_t \\ \ddot{\omega}_t \\ \dot{\theta}_d \end{bmatrix} = \begin{bmatrix} 0 & 1 & 0 \\ 0 & \left(\frac{K_s}{D_s} - \frac{D_s}{n^2 J_g} + \frac{D_s}{J_t} + \frac{1}{J_t}\frac{\partial T_w}{\partial \omega_t}|_{\omega_t, V_w, \beta}\right) & -\frac{K_s^2}{J_t D_s} \\ 0 & \frac{J_t}{D_s} & -\frac{K_s}{D_s} \end{bmatrix} \begin{bmatrix} \omega_t \\ \dot{\omega}_t \\ \theta_d \end{bmatrix} + \\ + \begin{bmatrix} 0 \\ \left(\frac{D_s}{n^2 J_t J_g} - \frac{K_s}{J_t D_s}\right) T_w - \frac{D_s}{n J_t J_g} T_g \\ 0 \\ -\frac{T_w}{D_s} \end{bmatrix} \tag{5.3}$$

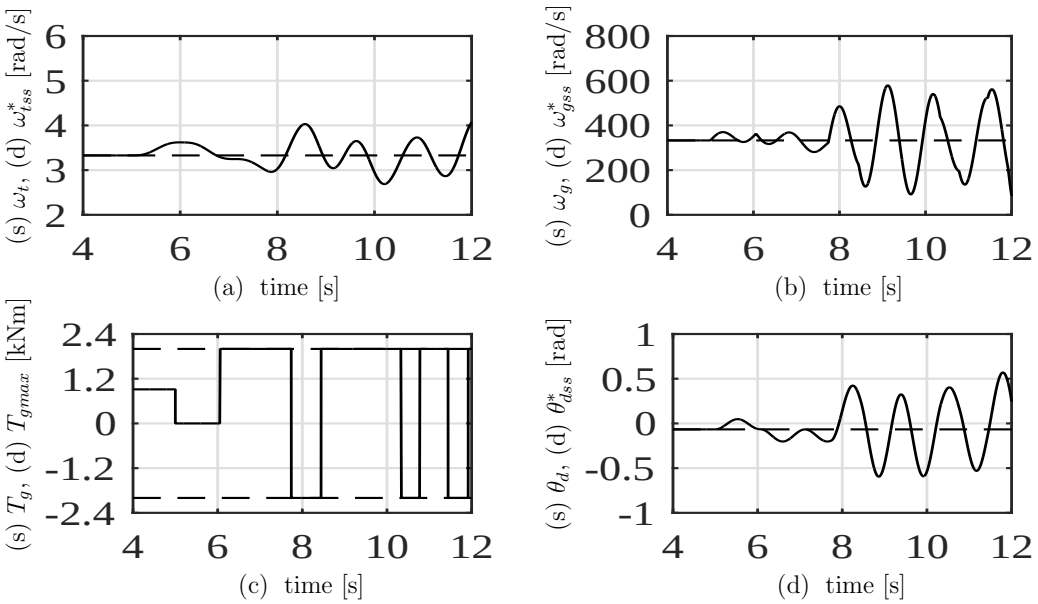

Figure 5.1: Results for the studied system equipped with the constrained HBF controller under 100% line voltage dip lasting for $1s$ with $10m/s$ wind speed. (a) Turbine speed (solid) and reference (dashed). (b) Generator speed (solid) and reference (dashed). (c) Generator torque (solid) and saturation limits (dashed). (d) Low speed shaft displacement (solid), and reference (dashed).

Given the relative degree of the system, the minimum smoothness level for a feasible trajectory has to be set accordingly to 2. Indeed, looking at (5.3) it is clear how, as T_g directly affect $\ddot{\omega}_t$, the speed reference must have finite second order time derivative if tracking with a bounded torque has to be ensured.

However, it is further to notice that system (1.25) relative degree depends on the damping coefficient D_s, which is physically related to mechanical friction. Ideally, D_s should be null and, in this case, it can be verified how the system relative degree increases to 3, and so does the minimum smoothness level requested for a feasible trajectory. In practice, friction is usually quite small and uncertain, then, from now on, a smoothness level 3 will be adopted for trajectory design, even if the model in (5.3) with $D_s \neq 0$ will be considered. This choice guarantees a smooth behavior of the system even for very small friction coefficients[3], and allow to exploit an additional degree of freedom (the reference second order derivative) in the problem, as it will be clarified in the following.

In the light of these considerations, among all the possible choices, polynomials are

[3]It can be verified that, given a generic trajectory with smoothness degree of 3, and the corresponding torque command, computed with the relative degree 2 model, for $D_s \to 0$, converge to the one computed with the relative degree 3 model, having $D_s = 0$. Owing to space limits, this analysis is not reported.

selected as trajectory candidates, due to their "easy-to-manage structure". In fact, to build a speed trajectory connecting two arbitrary points with smoothness level 3, a fifth order polynomial, with 6 tunable coefficients can be used, as illustrated in the following

$$\begin{aligned}\omega_t^* &= a_0 + a_1 t + a_2 t^2 + a_3 t^3 + a_4 t^4 + a_5 t^5 \\ \dot{\omega}_t^* &= a_1 + 2a_2 t + 3a_3 t^2 + 4a_3 t^3 + 5a_4 t^4 \\ \ddot{\omega}_t^* &= 2a_2 + 6a_3 t + 12a_4 t^2 + 20a_5 t^3.\end{aligned} \tag{5.4}$$

Coefficients $a_i,\ i = 0, \ldots, 5$ can then be selected to design a speed reference recovering the turbine optimal working point, starting from the condition after the dip, in minimum time and complying with the generator torque limitations. This point will be further elaborated in next paragraph, by posing a constrained optimization problem.

To this aim, it is profitable to explicitly express the torque command required to track a feasible trajectory. As mentioned this can be easily obtained by inverting system (5.3), i.e.

$$\begin{aligned}T_g^* = &-\tfrac{J_t}{n}\dot{\omega}_t^* + \tfrac{T_w(\omega_t^*, V_w, \beta)}{n} - nJ_g\dot{\omega}_t^* + \tfrac{nJ_g}{D_s}K_w^*\dot{\omega}_t^* + \\ &+ \tfrac{nJ_gK_s}{D_s}\left(\tfrac{J_t\dot{\omega}_t^* - K_s\theta_d^* - T_w(\omega_t^*, V_w, \beta)}{D_s}\right) - \tfrac{nJ_gJt}{D_s}\ddot{\omega}_t^*\end{aligned} \tag{5.5}$$

with $K_w^* = \frac{\partial T_w}{\partial \omega_t}|_{\omega_t^*, V_w, \beta}$, while the zero dynamic reference trajectory θ_d^* can be obtained integrating the third ODE in (5.3), that is by solving[4]

$$\dot{\theta}_d^* = \frac{J_t\dot{\omega}_t^* - K_s\theta_d^* - T_w(\omega_t^*, V_w, \beta)}{D_s}. \tag{5.6}$$

In this way the torque constraint can be straightforwardly expressed as a function of the speed reference trajectories and its derivatives. Furthermore, T_g^* in (5.5) can be used as a feedforward action to ensure tracking of the time varying trajectory, replacing the steady-state value defined in (5.1). Similarly ω_t^* and θ_d^* can be used to feed the state feedback part, along with a time varying reference for the original state ω_g which, by (1.25) can be expressed as $\omega_g^* = n\left(\omega_t^* + \dot{\theta}_d^*\right)$.

5.3.3 Optimization Problem

Having set the general structure of the trajectory as (5.4), and the corresponding feedforward torque command and state trajectories (for $D_s \neq 0$), it remains to be defined an optimization problem, aimed at minimizing the time to recover the original speed (and state) after the dip is cleared. Minimization has to be performed under the following constraints:

[4]It is worth noting that, in (5.6), as $D_s \to 0$, by Singular Perturbation arguments, it results $\theta_d \to \frac{1}{K_s}(J_t\dot{\omega}_t^* - T_w(\omega_t^*, V_w, \beta))$, which is the result of the model with $D_s = 0$ and relative degree equal to 3.

1. Initial state: Assumed to be known by measuring the turbine state, just after the dip clearance;

2. Final state: The desired trajectory must lead to the pre-fault (assuming the average wind speed has not changed during the fault, otherwise the corresponding optimal value can be set) optimal speed $\omega_{t-opt}(V_w)$ in the steady state condition $\dot{\omega}_{t-opt} = 0$, $\ddot{\omega}_{t-opt} = 0$, in order to guarantee the system settlement at the final point;

3. Torque constraint: The generator torque needed to achieve tracking, has to be inside the bounds along the entire trajectory.

Clearly, the initial and final states constraints can be explicated only at run-time, as they depend on the particular dip realization and current wind speed. Here this issue is neglected and assuming the initial and final conditions are given, the basic optimization strategy is formulated. In the next paragraph it will be shown how to exploit the basic problem solution to arrange an offline management of the a-priori unknown initial and final conditions. As regards the feasible generator torque bound, as usual the feedforward term in (5.5) will be considered for computing the control effort corresponding to the reference design. Thus, 10% margin is saved w.r.t. the limit T_{gmax}, in order to leave room for the state feedback action and compensation of parametric uncertainties.
Bearing in mind these considerations, the optimization problem is defined as follows. Assuming known initial points of ω_t, $\dot{\omega}_t$, and final points of ω_t, $\dot{\omega}_t$ and $\ddot{\omega}_t$, while letting the initial value of $\ddot{\omega}_t$ as a free decision variable, minimize the time t_f to move from initial to final point with a fifth order polynomial turbine speed shape, satisfying the generator torque constraints.
Note that the initial value for $\dot{\omega}_t$ can be retrieved from the turbine original state variables $\omega_t, \omega_m, \theta_d$ (assumed known from measurements), and dynamics (5.6).
Now, recalling the reasoning of Subsection 5.3.2, the following mathematical formulation is provided

$$
\begin{aligned}
&\min_{t_f,\ddot{\omega}_t(0),a_0,a_1,a_2,a_3,a_4,a_5} t_f, \text{ subject to} \\
&\omega_t^*(0) = \omega_t(0) = a_0,\ \dot{\omega}_t^*(0) = \dot{\omega}_t(0) = a_1,\ \ddot{\omega}_t(0) = 2a_2 \\
&a_0 + a_1 t_f + a_2 t_f^2 + a_3 t_f^3 + a_4 t_f^4 + a_5 t_f^5 = \omega_t^*(t_f) = \omega_{t-opt} \\
&a_1 + 2a_2 t_f + 3a_3 t_f^2 + 4a_3 t_f^3 + 5a_4 t_f^4 = \dot{\omega}_t^*(t_f) = \dot{\omega}_{t-opt} = 0 \\
&2a_2 + 6a_3 t_f + 12a_4 t_f^2 + 20a_5 t_f^3 = \ddot{\omega}_t^*(t_f) = \ddot{\omega}_{t-opt} = 0 \\
&-0.9T_{gmax} \leq T_g^*(t) \leq 0.9T_{gmax} \forall t \in [0, t_f] \\
&\text{with } T_g^* \text{ as in (5.5) and } \theta_d^* \text{ given by (5.6)}
\end{aligned}
\tag{5.7}
$$

The first set of equalities in (5.7) expresses the initial and final point constraint according to the polynomial trajectory structure defined in (5.4). The initial time has been set to zero for the sake of simplicity and without loss of generality. The last two constraints express the torque bound and the shaft torsional displacement as a function of turbine speed reference and its derivatives, according to model (5.3). By the problem structure (eight decision variable and six algebraic equality constraints) it can be verified that there are two degrees of freedom to be exploited for time minimization, the time interval t_f itself, and the initial value of the turbine speed second derivative $\ddot{\omega}_t^*(0)$, or, equivalently, coefficient a_2. Still the problem is nonlinear and non convex due to the products between a_2 and t_f and torque expression (5.5). However, given the limited number of true decision variables, it can be effectively solved numerically by *fmincon*, given in *Matlab* framework.

5.3.4 Offline Solution of the Proposed Optimization Problem

As stated before, we need to take into account the fact that, while the model data are a-priori known, even if with some uncertainty, the initial and final states are available only at runtime, the first one will mainly depend on the particular dip realization, while the second will stem from the current wind speed, giving the optimal turbine speed for MPPT. Thus, in principle, the trajectory planning should be executed at run time, right after the dip clearance. However, this would require a considerable computational effort to solve problem (5.7) on-line. To avoid this drawback, the key idea is to solve the problem offline for a meaningful set of boundary conditions, then use suitable interpolation to define the run-time state reference from the offline trajectories.

In order to reduce the dimensions of the boundary conditions to be considered, as a first step, the dependency on the final state is removed by reformulating the dynamics (5.3) in terms of displacement with respect the final state. In particular, knowing the average wind speed V_w, just after the dip clearance, i.e. at $t = 0$, and assuming it constant in the following seconds, the final state corresponding to MPPT optimal turbine speed can be computed. Namely, defining $\omega_{t-opt}(V_w)$ as the turbine speed giving the maximum power for a given average wind velocity[5], V_w, and $T_{w-opt}(V_w)$ as the corresponding torque, the final state for the trajectory design will be $\omega_t(t_f) = \omega_{t-opt}(V_w)$, $\dot{\omega}_t(t_f) = 0$, $\theta_d(t_f) = -T_{w-opt}(V_w)/K_s$. Therefore, introducing $\bar{\omega}_t = \omega_t - \omega_{t-opt}(V_w)$, $\dot{\bar{\omega}}_t = \dot{\omega}_t$, $\bar{\theta}_d = \theta_d + T_{w-opt}(V_w)/K_s$, dynamics (5.3) can be rewritten as in (5.8), and the optimal problem (5.7) can be reformulated by replacing ω_t and its derivatives with $\bar{\omega}_t$ and its derivatives, leading to a fixed end

[5]A pitch angle $\beta = 0$ is assumed from now on, without loss of generality.

condition equal to zero for any wind speed.

$$\begin{bmatrix} \dot{\bar{\omega}}_t \\ \ddot{\bar{\omega}}_t \\ \dot{\bar{\theta}}_d \end{bmatrix} = \begin{bmatrix} 0 & 1 & 0 \\ 0 & \left(\frac{K_s}{D_s} - \frac{D_s}{n^2 J_g} + \frac{D_s}{J_t} + \frac{1}{J_t}\frac{\partial T_w}{\partial \omega_t}|_{\omega_t, V_w, \beta}\right) & -\frac{K_s^2}{J_t D_s} \\ 0 & \frac{J_t}{D_s} & -\frac{K_s}{D_s} \end{bmatrix} \begin{bmatrix} \bar{\omega}_t \\ \dot{\bar{\omega}}_t \\ \bar{\theta}_d \end{bmatrix} + \\ + \begin{bmatrix} 0 \\ \left(\frac{D_s}{n^2 J_t J_g} - \frac{K_s}{J_t D_s}\right)(T_w - T_{w-opt}) - \frac{D_s}{n J_t J_g} T_g \\ 0 \\ -\frac{T_w - T_{w-opt}}{D_s} \end{bmatrix} \tag{5.8}$$

Actually, the new optimization problem in displacement coordinates w.r.t. the final state is not completely independent of the absolute final state, because of the non-linear terms in (5.8). Nevertheless, the following effective linear approximations can be adopted:

$$\begin{gathered} \frac{\partial T_w}{\partial \omega_t}|_{\omega_t, V_w, \beta} \approx K_{wM} = \max_{V_w} |\frac{\partial T_w}{\partial \omega_t}|_{\omega_{t-opt}(V_w), V_w} \\ T_w(w_t, V_w) - T_{w-opt}(V_w) \approx K_{wM} \bar{\omega}_t \end{gathered} \tag{5.9}$$

Hence, the resulting optimization problem is fully independent of the final condition, and with linear torque bound stemming from (5.8), (5.9). However, a meaningful set of initial conditions (reformulated as displacements w.r.t. final state) need to be defined for computing off-line solutions. To this purpose, an admissible range for the initial condition of the three state components $\bar{\omega}_t$, $\bar{\omega}_g = \omega_g - n\omega_{t-opt}(V_w)$, $\bar{\theta}_d$ need to be defined. Starting from the shaft torsional displacement, a reasonable choice is to select $[\bar{\theta}_{dmin}, \bar{\theta}_{dmax}] = \left[-1.5\frac{nT_{gnom}}{K_s}, 1.5\frac{nT_{gnom}}{K_s}\right]$, that is a considerable variation related to the steady-state angular displacement corresponding to the generator nominal torque. For what concerns the turbine and generator angular speed the intervals $[\bar{\omega}_{t-min}, \bar{\omega}_{t-max}] = [0.7\Delta\omega_t - \Delta\omega_o, 1.3\Delta\omega_t + \Delta\omega_o]$, and $[\bar{\omega}_{g-min}, \bar{\omega}_{g-max}] = [n\bar{\omega}_{t-min}, n\bar{\omega}_{t-max}]$. Where $\Delta\omega_t$ is defined as the speed variations (increases) corresponding to setting T_g to zero and assuming a constant wind torque $T_{w-opt}(V_wM)$, with V_{wM} the maximum admissible wind speed, to push the turbine for the entire nominal line fault defined in Section 5.2. This is an approximated worst case scenario (T_w actually decreases when $\omega_t > \omega_{t-opt}$) allowing to easily compute the speed variations from dynamics (1.25). Then a $\pm 30\%$ change of such variation is considered to construct the angular speeds ranges, in order to deal with lighter and harsher real dips. In addition, $\Delta\omega_o$ takes into account the speed variations due to conversion of the spring potential energy stored in the drivetrain with an initial torsion equal to $\bar{\theta}_{dmax}$.

All that being given, it has to be defined how many points to consider within the specified states intervals. A suitable trade-off between memory request and performance has to be sought; obviously considering a fine grid of points allows to reduce

the optimality gap of interpolation w.r.t. on-line optimization, on the other hand a large number of points (then offline computed trajectories) implies a larger look up table which has to be stored on board of the turbine control hardware. In this work, a good compromise has been found by taking five points for each state variable, as it will be assessed in next Section simulation tests. However, the main issue is to guarantee that interpolation of offline trajectories provides feasible solutions, that is the corresponding torque command is inside the admissible bounds. Linearity of the constraints in the optimization problem obtained by applying (5.9) in (5.8) can be effectively exploited for such issue. Indeed, by linearity, the feasibility is ensured for any reference obtained by convex combination of the offline computed trajectories, that is for any initial condition belonging to the convex hull of the considered state range. As a result, feasibility is preserved no matter what grid granularity is chosen. Then, grid resolution can be tuned only for obtaining interpolated solutions which are not too suboptimal w.r.t. the on-line results.
In addition, it is worth noting that, beside the initial state points defined above, one additional point can be introduced, the one characterized by $\bar{\omega}_t(0) = 0$, $\bar{\omega}_g(0) = 0$ and $\bar{\theta}_d(0) = 0$. Clearly for such point the optimal trajectory will be identically null. Then, this can be easily exploited to generate interpolated trajectories for any initial condition characterized by $\bar{\omega}_t(0) < \bar{\omega}_{t-min}$ or $\bar{\omega}_g(0) < n\bar{\omega}_{t-min}$.

5.4 Simulation Results

To assess the quality of the proposed solution, the considered benchmark WT, equipped with the proposed controller, combining the HBF controller and a feed-forward term depending on the fifth order polynomial speed reference design as in (5.5) has been tested under the same wind speed and faulty line voltage conditions reported in Subsection 5.3.2.
Fig. 5.2 shows results corresponding to the on-line optimization solution, tailored to the system conditions after the simulated dip, which for the sake of completeness, are here reported: $\omega_t(t_{dip-end}) = 3.62 rad/s, \omega_g(t_{dip-end} = 362.8 rad/s,\ \theta_d(t_{dip-end}) = -0.07 rad$. Using such values as initial conditions to solve problem (5.7) yields $t_f = 2.51s$, $\ddot{\omega}_t^*(0) = 0.058 rad/s^3$, and $a_0 = 3.62,\ a_1 = -0.0234,\ a_2 = 0.029,\ a_3 = -0.194,\ a_4 = 0.11,\ a_5 = -0.017$. As illustrated in Fig.5.2 (a), the trajectory is perfectly tracked, and steers the WT to the optimal steady-state condition in short time, while keeping generator torque within constraints (see Fig.5.2 (b)). Looking at the torque and generator speed waveforms in Fig. 5.2 (b), (c) respectively, it seems discontinuity in the first derivative arises at the trajectory end point. Actually, the required smoothness is preserved also around that points, only the final decrease to steady state is fast, and cannot be clearly observed at the current plot time scale.

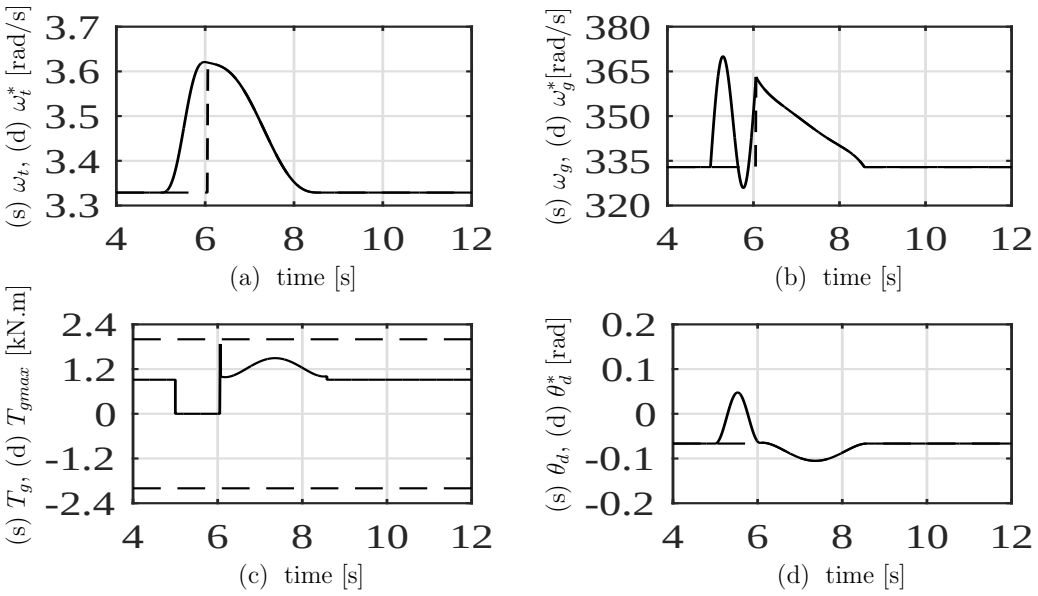

Figure 5.2: Transient results for the studied system equipped with the suboptimal trajectory planning obtained by interpolation from a look up table at 100% line voltage dip lasting for $1s$ with nominal wind speed ($10m/s$). (a) Turbine speed (solid) and reference (dashed). (b) Generator speed (solid) and reference (dashed). (c) Generator torque (solid) and saturation limits (dashed). (d) Low speed shaft displacement (solid), and reference (dashed).

To validate the interpolation strategy of offline trajectories, obtained according to the procedure described in Subsection 5.3.4, a look up table has been built containing the optimization results corresponding to the sets $[\bar{\omega}_{t-min}, \bar{\omega}_{t-max}] = [0.04, 0.61]rad/s$, $[\bar{\omega}_{g-min}, \bar{\omega}_{g-max}] = [4, 61]rad/s$, $[\bar{\theta}_{d-min}, \bar{\theta}_{d-max}] = [-0.1, 0.1]rad$. These ranges have been computed according to the guidelines outlined in Subsection 5.3.4. Each range has been equally spaced into five different points for offline computation. Fig. 5.3 shows the corresponding simulation results, with interpolation strategy used to deal with the same scenario reported before. The trajectory parameters obtained by interpolation are: $t_f = 3.24s$, $\ddot{\omega}_t^*(0) = 0.06rad/s^3$, and, as a consequence $a_0 = 3.62$, $a_1 = -0.023$, $a_2 = 0.03$, $a_3 = -0.09$, $a_4 = 0.049$, $a_5 = -0.005$. By this values, and looking at Figs. 5.3 (a),(b),(d), it can be noted how the performance, in terms recovery time minimality, are not too far for what can be obtained with an on-line optimization. In addition, thanks to the conservative linearization of inequality constraints (5.5), torque feasibility is preserved, as underscored by Fig. 5.3 (c). It is further to remark that, to obtain a feasible trajectory, the zero dynamics reference θ_d^*, has been generated on-line by (5.6) using the actual value of T_w, instead of the interpolation of trajectories based on bound (5.9). Being the integration of a first order ODE, this does not add significant complexity to the control unit.

Finally, to investigate robustness of the proposed approach against relevant parametric uncertainties, several simulation tests have been carried out, focusing in particular on friction coefficient D_s and shaft stiffness K_s variations, as these parameters are typically roughly known in practice. Owing to space limits, results for one scenario are reported in Fig. 5.4, corresponding to D_s reduced to one third and K_s to 80% w.r.t. the values reported in Tab. A.3, which have been used for control design. It can be noted how the integral action of the HBF ensures the optimal turbine speed is reached (Fig. 5.4 (a)), despite a static error on θ_d (Fig. 5.4 (d)), due to the mismatch in K_s. Indeed, thanks to the margin left for the HBF stabilizing and damping action, and the conservative torque bounds linearization, the after dip recovery is smooth (even if, clearly, perfect tracking cannot be achieved), and saturation limits are not hit (see Fig. 5.4 (c)), despite the relevant parametric uncertainty.

5.5 Conclusion

In this chapter a simple, low complexity control solution has been presented for what concerns the post grid fault recovery of wind turbines. In this respect, a standard high bandwidth state feedback controller, devoted to achieve WT nominal objectives, such as speed tracking and damping injection to tame shaft mechanical

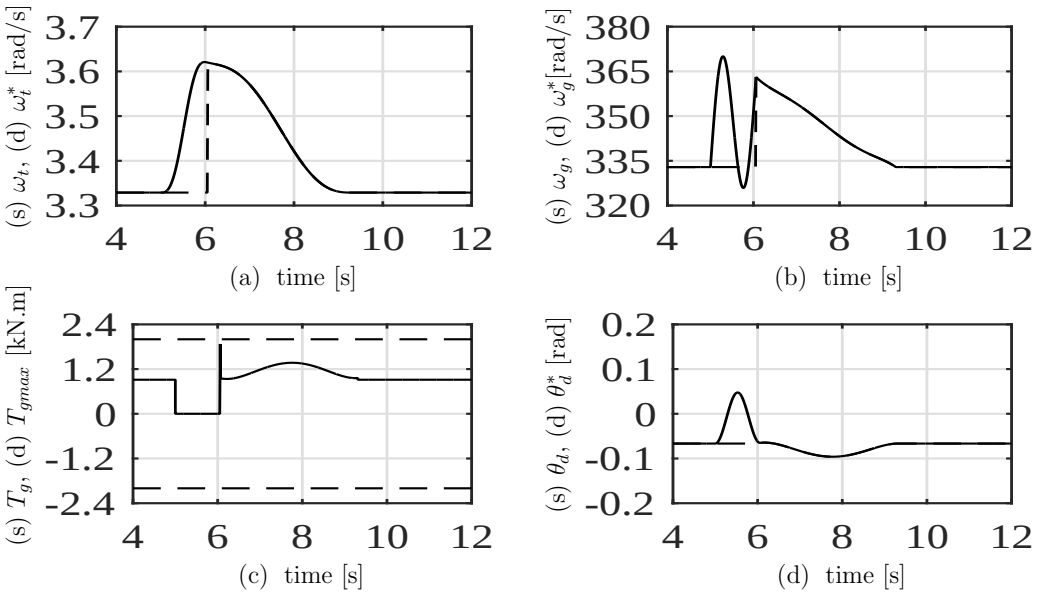

Figure 5.3: Transient results for the studied system equipped with the suboptimal trajectory planning obtained by interpolation from a look up table at 100% line voltage dip lasting for $1s$ with nominal wind speed ($10m/s$). (a) Turbine speed (solid) and reference (dashed). (b) Generator speed (solid) and reference (dashed). (c) Generator torque (solid) and saturation limits (dashed). (d) Low speed shaft displacement (solid), and reference (dashed).

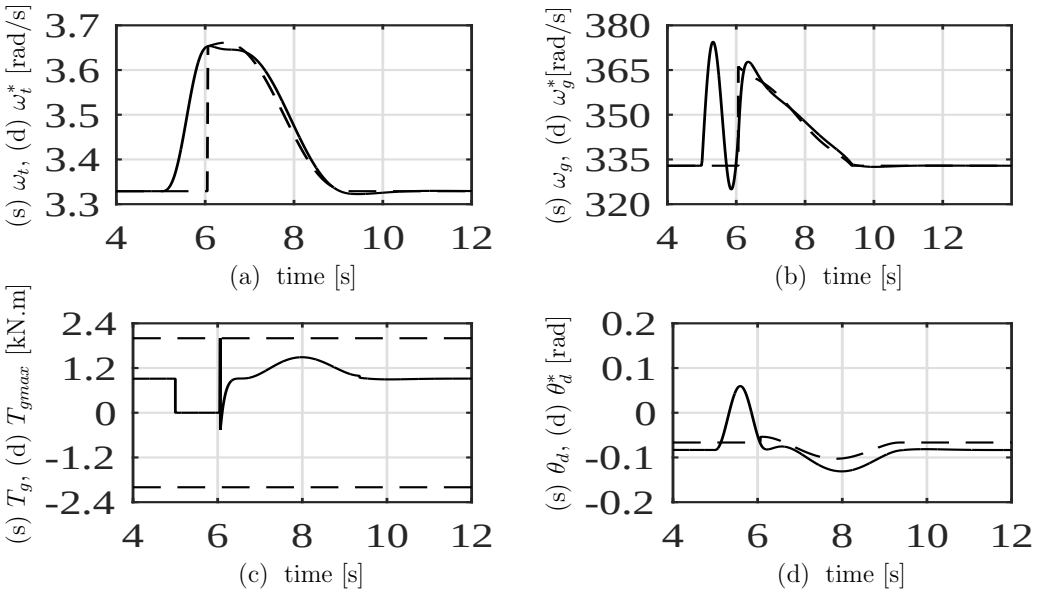

Figure 5.4: Transient results for the studied system,equipped with the trajectory planning obtained by interpolation from a look up table at 100% line voltage dip lasting for $1s$ with nominal wind speed ($10m/s$). -20% and -66.7% variations w.r.t. nominal values have been implemented for K_s and D_s, respectively. (a) Turbine speed (solid) and reference (dashed). (b) Generator speed (solid) and reference (dashed). (c) Generator torque (solid) and saturation limits (dashed). (d) Low speed shaft displacement (solid), and reference (dashed).

vibrations, has been joined to a suitable reference trajectory planning. By functional controllability arguments and optimization, it has been shown how to design such unit to guarantee a smooth, minimum time, and feasible transition back to the turbine optimal equilibrium after the fault has been cleared. Such performance cannot be achieved with standard linear filters applied to smooth the transients.
Exploiting insights from the system properties, optimization has been shifted offline in order to preserve low complexity of the run time control algorithm. Simulations show promising performance, making the solution a potential alternative to more complex and computationally heavy frameworks such has dynamic programming and model predictive control.
In future works, on-line filters as the ones of [78] can be considered, even if their usage is not straightforward in the presented framework, without introducing relevant conservatisms.

Chapter 6

Improved Trajectory Tracking and LVRT Performance in DFIG-based Wind Turbines

6.1 Introduction

As mentioned before, DFIG is one of the most popular technologies for wind energy applications. Indeed, more than 50% of the currently installed Wind Energy Conversion Systems (WECSs) use this class of electrical machines [4]. Fig.6.1 shows the configuration of a complete benchmark of a DFIG-based Wind Turbine (WT) system, in which stator is connected directly to grid, while rotor is fed by back-to-back Grid/Rotor Side Converters (GSC/RSC) allowing bidirectional power flow between the grid and generator rotor side. This topology allows WT variable speed control, with RSC managing a fraction (around 30%, but depending on slip value) of the overall generation system power. Thus, RSC has about one third of the size, cost and losses of a conventional variable-speed drive. It was outlined before that among the regulations issued within the national grid codes, LVRT capability achievement for a predefined set of possible grid faults, is one of the most critical requirements. In this way, well-known American FERC and German E.ON Netz regulations were exemplified as the base LVRT requirements should be taken into account in control design. For the voltage dip drawbacks detailed in Ch.2, the most conventional remedy crowbar protection was checked and it's corresponding side effects, as well [27, 32, 79, 22].

To overcome these drawbacks, and endow WECSs with LVRT property, several strategies have been proposed in the literature [32, 80, 35, 36]. The main contribution of this chapter to such literature is to limit electromagnetic signals oscillations by the pure control solution detailed in Ch.3 in combination with a suitably accurate

tracking of torque and reactive current references throughout the voltage dip.
In this way, improved LVRT performance can be achieved, also for severe faults, with no additional protection hardware.

The solution is mainly focused on rotor-side control, which is the knob to be used to obtain the aforementioned properties. In this context, the framework of field-oriented control (see [13], [11] for applications to DFIG control in nominal scenarios) will serve as the base to design advanced strategies to deal with line faults. For what regards grid side control, the goal is to regulate the DC-link voltage, briefly presented here and well-stated in the literature [9]. In this chapter, both RSC and GSC controls will be implemented and considered, along with power electronic converters non-idealities, WT and gearbox mechanics, and Maximum Power Point Tracking (MPPT) algorithm, for validation on a complete WECS benchmark via detailed simulations. In this context, a feedforward-feedback RSC control unit, first presented in [50] and detailed in Ch.3 is exploited, assuming rotor currents as the controlled output variables. As stated before, the feedforward terms are based on suitable oscillation-free state references which, in turn, are derived from a thoughtful analysis of the system internal dynamics behavior under line voltage sags. Also the feedback part designed according to modern saturated control techniques (details in Ch.3) is utilized again to endow the controller with some robustness, to improve convergence towards the desired state trajectories, and to further limit oscillations under faults. Relying on such unit, an additional, novel key point presented here is an exact, analytical method to convert torque and stator reactive current references (the typical variables of interest for DFIG-based WT) into the corresponding rotor currents references. This improves tracking under line faults, with clear benefits on the system overall behavior under line dips.

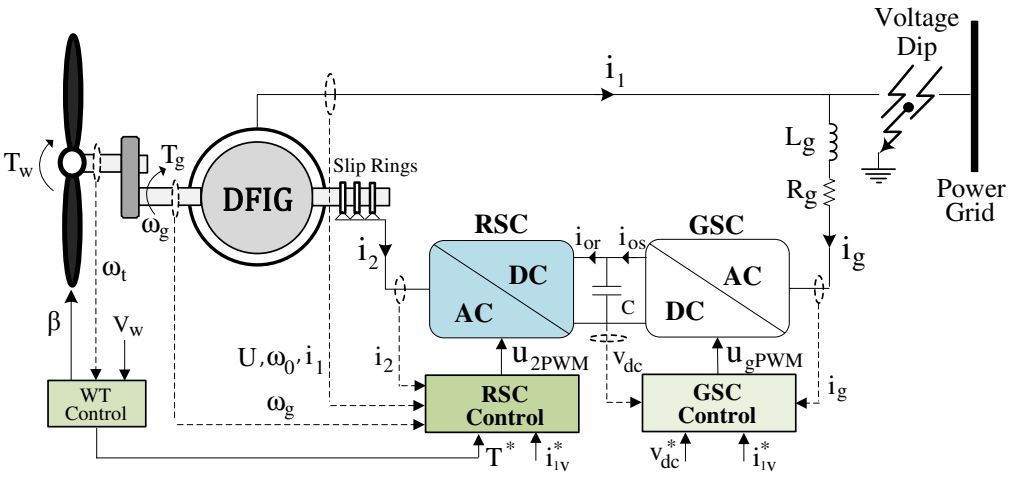

Figure 6.1: General configuration of the studied DFIG WT system.

The outlines of this chapter which is according to what we have presented in [81], is structured as follows. In Section 6.2, control objectives and system physical limits are presented. In this way, the Subsection 6.2.3 is devoted to RSC Control in which the first two parts are dedicated to recalling the trajectory planning and state feedback designs, which are detailed in Ch.3. Then, in the last part, the analytical approach for obtaining rotor current references from torque and stator reactive current is elaborated, based on the previously obtained oscillation-free zero dynamics trajectories. Finally, a brief remark of grid side control is given in the Subsection 6.2.3.
Numerical simulation results, obtained using Matlab/Simulink environment, are presented in Section 6.3 for a $0.5MW$ DFIG-based WT, to validate the proposed strategy. Some final remarks on the presented solution are discussed in Section 6.4.

6.2 Control Strategy

Here the control strategy, devoted to make DFIG-based wind turbine to cope with severe voltage faults, is elaborated. First, Maximum Power Point Tracking (MPPT) and pitch control of the WT is briefly explained. As mentioned in the Introduction, the focus is put on rotor-side control, which is crucial to achieve proper generator performance. Then, grid side control which is handled by means of standard solutions detailed in literature, is briefly recalled.

6.2.1 MPPT and Pitch Control

Extracting the maximum wind power is the main goal in the turbine control process. If the blade characteristic is accurately known, then the turbine reference speed maximizing the power captured from the wind can be easily computed as $\omega_{t-opt} = \frac{\lambda_{opt} V_w}{R_w}$, where, λ_{opt} is the value maximizing the coefficient C_P for an optimized pitch angle $\beta_1 opt$ (usually $\beta_1 opt = 0$), which can be easily derived by equations similar to (1.28). Otherwise, the optimal speed reference can be retrieved by Maximum Power Point Tracking (MPPT) algorithms [82] [83]. In this thesis, the blade aerodynamics is assumed known.
Whenever generator power/torque saturation is hit (in case of strong wind), then the torque reference is frozen to the saturation value and the turbine speed is regulated by the pitch system [33].
The blade pitch angle control is designed to maximize the power extraction of the wind as well as to prevent over rated power production in high wind conditions. In

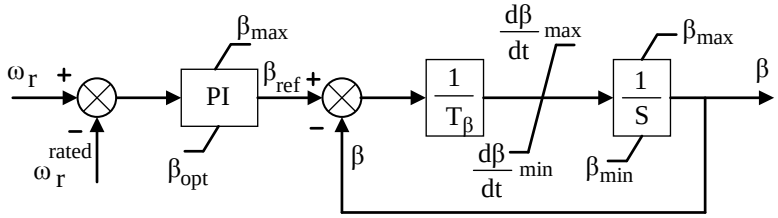

Figure 6.2: Standard two-mass wind turbine model with gearbox.

this thesis, the pitch servo is modeled as:

$$\frac{d\beta}{dt} = \frac{1}{T_\beta}(\beta_{ref} - \beta) \tag{6.1}$$

The pitch control block is illustrated in Fig. 6.2. When the generator speed increases, the pitch control will be activated to tune the pitch angle in such a way that the turbine power gets restricted inside the rated values.

6.2.2 Rotor Side Control

As elaborated before, DFIG's objectives are usually formulated in terms of torque, and stator-side reactive current reference values[1]. The corresponding equations are recalled as follows:

$$T_m = \eta_2(\phi_{1v} i_{2u} - \phi_{1u} i_{2v}). \tag{6.2}$$

$$Q = -\frac{3}{2} U i_{1v} = -\frac{3}{2} U \left[\frac{\phi_{1v} - L_m i_{2v}}{L_1}\right]. \tag{6.3}$$

Hence, the last equation gives:

$$i_{1v} = \frac{\phi_{1v} - L_m i_{2v}}{L_1}. \tag{6.4}$$

References on such variables need to be mapped into corresponding trajectories for the state variables in (1.23), namely rotor currents and stator fluxes. It was also mentioned that in principle, there are infinite possibilities, as two trajectories must be converted into four state variables references. However, only two control inputs are available, thus the state evolution cannot be arbitrarily imposed [2]. In addition, the ensuing constraints, stemming from the machine physical limits, have to be accounted for: rotor current limits, given by RSC power switches ratings, flux linkage bounds (due to magnetic core saturation), and rotor voltages limitation, again related to RSC power electronics sizing.

[1]Tipically, Grid Codes specify LVRT reactive power support capability in terms of capacitive stator current requirements [33].

[2]Some dependencies arise, related to the system relative degree with respect to control inputs, and the form of the corresponding internal dynamics.

Beside such nominal operation goals, a "graceful behavior" has to be guaranteed under grid faults, limiting oscillations, particularly for rotor currents, and ensuring a proper tracking of T_g and i_{1v} set points. To keep the oscillations small, state references should be suitably adapted to line voltage disturbances. This will be shown to be crucial for preventing DFIG's disconnection during voltage dips. Clearly, a proper control unit, has to be designed for tracking the aforementioned references. Here, the problem is tackled as follows: first known rotor current references, related to torque and reactive power set points, are assumed to design stator flux trajectories meeting objectives and constraints mentioned before. Based on such references suitable feedforward control actions are generated. Then, a state feedback unit is combined to these in order to provide robustness, and further minimize oscillations under faults, accounting for bounds on control inputs (rotor voltages).
To achieve improved tracking under voltage dips, in 6.2.2, a method to perform exact mapping from the original torque and reactive power references (assumed to belong to specific class of functions) to rotor current set points is elaborated. In Section 6.3, it will be shown how such procedure allows to achieve better torque accuracy, particularly when abrupt decrease due to line dips is required, making it a not negligible part of the overall proposed solution.

Trajectory Planning and Feedforward Action Generation

As mentioned above, here known rotor currents references (i_{2u}^*, i_{2v}^*) are assumed. Then, it remains to determine suitable trajectories $(\phi_{1u}^*, \phi_{1v}^*)$ for stator fluxes, whose dynamics in (1.23), can be recognized as the system internal ones [40]. Assuming perfect rotor currents tracking, the corresponding zero dynamics, w.r.t. current outputs, of system (1.23) reads as the equations (3.7). In the Subsection 3.3.1, it was explained that for conventionally small α_1, the asymptotically stable LTI system (3.5) shows poorly damped oscillatory modes at $-\alpha_1 \pm j\omega_0$. Moreover, the voltage perturbations enters the dynamics as exogenous input. Hence, the highe sensitivity of DFIG to voltage dip disturbances can be concluded. Then, in order to get rid of the solutions with the national oscillations, through the analytical solution of the mentioned ODEs, the forced steady-state response under inputs (i_{2u}^*, i_{2v}^*, U) were smartly selected. To operatively exploit the analytical solution (3.20), assumptions on the class of input functions need to be made, in order to bound the number of their not null time derivatives. In the remainder of this chapter, current references and the line voltage U will be assumed bounded piece-wise linear signals, i.e. derivatives from second order on will be assumed null. Details about the kind of torque and reactive power signals which can be generated with this approximation are given in paragraph 6.2.2. Summarizing all these reasoning detailed in 3.3.1, the stator flux

references are selected as:

$$\begin{aligned} z_{2u}^*(t) &= K_{1u}i_{2u}^* + K_{2u}i_{2v}^* + K_{3u}U + K_{4u}\dot{i}_{2u}^* + K_{5u}\dot{i}_{2v}^* + K_{6u}\dot{U}, \\ z_{2v}^*(t) &= K_{1v}i_{2u}^* + K_{2v}i_{2v}^* + K_{3v}U + K_{4v}\dot{i}_{2u}^* + K_{5v}\dot{i}_{2v}^* + K_{6v}\dot{U} \end{aligned} \tag{6.5}$$

where all the "K-coefficients", depending on system parameters, are reported in Tab. A.4 in the Appendix. To compute trajectories above, $\dot{U}$ is needed. For this purpose, and to estimate the line angle for the $u-v$ frame, a suitable observer will be adopted[3]. Finally, based on (6.5), and known current references, the ensuing feedforward control terms are defined

$$\begin{aligned} u_{2uff} &= \sigma_2\left(\gamma_2 i_{2u}^* - (\omega_0-\omega_g)i_{2v}^* - \alpha_1\beta_2 z_{2u}^* + \beta_2\omega_g z_{2v}^* + \beta_2 U + \dot{i}_{2u}^*\right), \\ u_{2vff} &= \sigma_2\left(\gamma_2 i_{2v}^* + (\omega_0-\omega_r)i_{2u}^* - \alpha_1\beta_2 z_{2v}^* - \beta_2\omega_g z_{2u}^* + \dot{i}_{2v}^*\right). \end{aligned} \tag{6.6}$$

Beside the open loop law above, it can be proved to provide global asymptotic stability, in order to achieve robustness against parametric uncertainties, and further tame oscillations during faults, a feedback term needs to be designed. This part is specified in the next paragraph.

State Feedback Design

In Subsection 3.5.3, it was explained that in order to enrich the transient performance of the studied system under voltage dip conditions, the feedforward control designed based on zero dynamics trajectory planning, was modified as a closed-loop controller by adding a saturated linear feedback law in the following form:

$$\begin{aligned} u_{2u} &= u_{2uff} + v_u,\ u_{2v} = u_{2vff} + v_v \\ \underbrace{\begin{bmatrix} v_u \\ v_v \end{bmatrix}}_{v} &= \sigma(p) = \begin{bmatrix} sat(p_u) \\ sat(p_v) \end{bmatrix},\ p = K\tilde{x}_a \end{aligned} \tag{6.7}$$

where a saturated linear feedback law v on the augmented (with integral terms on currents) state error $\tilde{x}_a = \Big[\underbrace{\tilde{\phi}_{1u}\ \tilde{\phi}_{1v}\ \tilde{i}_{2u}\ \tilde{i}_{2v}}_{\tilde{x}}\ \underbrace{\int\tilde{i}_{2u}\int\tilde{i}_{2v}}_{\tilde{\chi}}\Big]^T$, needs to be tuned to further limit oscillations during dips. Bounds on v can be determined as $v_{jmax} = u_{2jmax} - u_{2jffmax},\ j = u, v$ where u_{2jmax} are given by RSC ratings and $u_{2jffmax}$ by upper bounds on the feedforward effort in some worst case scenarios.
By some computations, using (6.6)-(6.7) and (1.23), state feedback design can be performed on the following linear, input-saturated error dynamics:

$$\dot{\tilde{x}}_a = F(t)\tilde{x}_a + G\sigma(K\tilde{x}_a),\ \text{with}\ \tilde{x} = C\tilde{x}_a. \tag{6.8}$$

[3]Details are not reported here for brevity, the interested reader is referred to [52].

where $F(t)$ is related to the right autonomous side of (1.23) depending on the time-varying rotor speed $\omega_g(t)$. Then, by means of modern saturated feedback design techniques and differential inclusion arguments to deal with time-varying systems, matrix K satisfying the aforementioned goals can be obtained by solving the following optimization problem (see [50] for details):

$$\begin{aligned}
&\min_{Q=Q^T>0,\delta>0,Y,Z} \delta, \text{ subject to} \\
&C^T Q C \leq \delta I_{n\tilde{x}} \\
&QF_k^T + F_k Q + GD_iY + GD_i^- Z + Y^T D_i G^T + Z^T D_i^- G^T < 0, \\
&k = \{min, max\},\ i \in [1,4] \\
&\begin{bmatrix} Q & Z_j^T \\ Z_j & v_{jmax}^2 \end{bmatrix} \geq 0\ j = u, v,\ Q - R^{-1} \geq 0.
\end{aligned} \tag{6.9}$$

and recovering K as $K = YQ^{-1}$.

Reference Mapping for Improved Tracking

As mentioned, beside keeping the oscillations limited, for LVRT it is important to precisely track the varying torque and capacitive current under line faults. However, rotor currents are typically steered by means of RSC control. In this part, a precise mapping from the original torque and reactive current references into the corresponding currents references (i_{2u}^*, i_{2v}^*) is designed and analytically solved, taking into account the zero dynamics solutions obtained for the desired oscillation-free trajectories in (6.5). The rationale behind this approach is the following: improved tracking cannot be achieved without a suitable planning of the system zero dynamics, otherwise high flux oscillations would arise inducing core saturation and downgrading the system behavior[4]. Therefore, the zero dynamics reference planning has to be preserved. To improve tracking results w.r.t. what in [50] (and commonly applied in the literature), first-order time derivatives of all the signals involved are considered leading to a non trivial system of nonlinear equations which is analytically solved. Starting with torque, assuming a known reference T_g^* (provided from the MPPT solution recalled in 6.2.1), by the last equation of (1.23), we can write:

$$\begin{aligned}
T_g^* &= \eta_2(z_{2v}^* i_{2u}^* - z_{2u}^* i_{2v}^*) \\
\dot{T}_g^* &= \eta_2(\dot{z}_{2v}^* i_{2u}^* + z_{2v}^* \dot{i}_{2u}^* - \dot{z}_{2u}^* i_{2v}^* - z_{2u}^* \dot{i}_{2v}^*).
\end{aligned} \tag{6.10}$$

Now, the desired stator flux trajectories obtained in (6.5), and their first-order time derivatives can be replaced in (6.10) to express the torque set point and its derivative

[4]See [50] where an example with standard feedback linearisation control is reported to underscore this fact.

only as a function of the rotor current references, and line voltage U. Recalling the hypothesis of piecewise linear rotor currents made to derive references (6.5), and assuming the same for U (corresponding to a trapezoidal dip shape approximation) leads to:

$$\begin{aligned} \dot{z}^*_{2u} &= K_{1u}\dot{i}^*_{2u} + K_{2u}\dot{i}^*_{2v} + K_{3u}\dot{U}, \\ \dot{z}^*_{2v} &= K^*_{1v}\dot{i}^*_{2u} + K_{2v}\dot{i}^*_{2v} + K_{3v}\dot{U}. \end{aligned} \tag{6.11}$$

Substituting the expressions above, as well as the zero dynamics trajectories from (6.5), into (6.10), the equations describing the torque reference and its derivative based on rotor currents, stator voltage, and their first-order derivatives read as:

$$\begin{aligned} &-\frac{T}{\eta_2} + (K_{3v}U + K_{6v}\dot{U})i^*_{2u} - (K_{3u}U + K_{6u}\dot{U})i^*_{2v} + K_{1v}{i^*_{2u}}^2 + \\ &\quad + (K_{2v} - K_{1u})i^*_{2u}i^*_{2v} - K_{2u}{i^*_{2v}}^2 + K_{4v}i^*_{2u}\dot{i}^*_{2u} - K_{5u}i^*_{2v}\dot{i}^*_{2v} + \\ &\quad - K_{4u}\dot{i}^*_{2u}i^*_{2v} + K_{5v}\dot{i}^*_{2v}i^*_{2u} = 0 \end{aligned} \tag{6.12}$$

$$\begin{aligned} &-\frac{\dot{T}}{\eta_2} + 2K_{1v}\dot{i}^*_{2u}i^*_{2u} - 2K_{2u}\dot{i}^*_{2v}i^*_{2v} + (K_{2v} - K_{1u})\dot{i}^*_{2u}i^*_{2v} + K_{3v}\dot{U}i^*_{2u} + \\ &\quad + (K_{2v} - K_{1u})\dot{i}^*_{2v}i^*_{2u} + (K_{5v} - K_{4u})\dot{i}^*_{2u}\dot{i}^*_{2v} + K_{4v}(\dot{i}^*_{2u})^2 + \\ &\quad + (K_{3v}U + K_{6v}\dot{U})\dot{i}^*_{2u} - K_{3u}\dot{U}i^*_{2v} - (K_{3u}U + K_{6u}\dot{U})\dot{i}^*_{2v} - \\ &\quad + K_{5u}(\dot{i}^*_{2v})^2 = 0. \end{aligned} \tag{6.13}$$

Similar reasoning can be made for what concerns the mapping reactive stator current reference i^*_{1v}, which, recalling (6.4), can be written as: $i^*_{1v} = \dfrac{z^*_{2v} - L_m i^*_{2v}}{L_1}$. Again, substituting z^*_{2v} according to (6.5), the intended equation for i^*_{1v} is attained as:

$$\begin{aligned} &-L_1 i^*_{1v} + K_{3v}U + K_{6v}\dot{U} + K_{1v}i^*_{2u} + (K_{2v} - L_m)i^*_{2v} + \\ &\quad + K_{4v}\dot{i}^*_{2u} + K_{5v}\dot{i}^*_{2v} = 0. \end{aligned} \tag{6.14}$$

Deriving (6.14), the equation expressing $\dot{i}^*_{1v}$ in terms of the unknowns $i^*_{i2u}, i^*_{2v}, \dot{i}^*_{2u}, \dot{i}^*_{2v}$ is easily obtained:

$$-L_1\dot{i}^*_{1v} + K_{3v}\dot{U} + K_{1v}\dot{i}^*_{2u} + (K_{2v} - L_m)\dot{i}^*_{2v} = 0. \tag{6.15}$$

From the algebraic viewpoint, we have obtained a system of four equations, including two second-order non-linear (6.12), (6.13), and two linear ones (6.14), (6.15), relating the known variables (original references) $[T^*_g, \dot{T}^*_g, i^*_{1v}, \dot{i}^*_{1v}]$, with the set of four unknown variables $[i^*_{2u}, i^*_{2v}, \dot{i}^*_{2u}, \dot{i}^*_{2v}]$ also via the known parameters $[U, \dot{U}]$. In terms of the class of torque and reactive current signals which can be obtained by the equations above, it can be shown[5] that, assuming piecewise linear rotor currents, piecewise quadratic functions can be obtained for what concerns torque, due

[5]Owing to space constraints the mathematical details are omitted.

to the nonlinear nature of eqs. (6.12), (6.13). While piecewise linear function can be clearly achieved for what concerns i^*_{1v}. This degree of freedom is sufficient to generate the typical references arising in DFIG-based WT control application.
For what concerns the system of equations solution, the following simple procedure can be carried out: first, $\dot{i}^*_{2u}, \dot{i}^*_{2v}$ in the non-linear equations (6.12), (6.13) are replaced by the solutions (parametrized in i^*_{2u}, i^*_{2v}), of the linear equations (6.14), (6.15). This way, the torque equation and its first-order derivative are expressed as quadratic functions of the rotor currents references. This equations can be manipulated with standard procedure[6] to obtain a fourth-order equation in one variable (e.g. i^*_{2v}), defining a *Quartic Function*, whose roots can be expressed in closed-form in terms of its coefficients. Obviously, the other variables can be retrieved substituting back such roots in the equations. From an engineering view point, we are clearly interested in real valued solutions (the nature of solutions depends on the value that the coefficients assume at a given instant). In case, there are more than one, the one providing the minimum *Euclidean norm* for the rotor current reference vector is selected. This choice stems from quite obvious energy efficiency considerations: the less the currents the lower the power dissipation by *Joule* effect is, and also the RSC electronics would be less stressed.
It is further to remark that the proposed mapping solution, beside being exact (for the class of references mentioned before), can be efficiently implemented online, for each set of the original references T^*_g and i^*_{1v}, and parameters U, $\dot{U}$. Indeed, being a closed-form solution, no iterative procedure is needed and the computational burden is reduced to the evaluation of a function providing the roots in terms of the current coefficients, and the best solution selection, according to the criterion explained above.

6.2.3 Grid Side Control

The controlled boost converter adopted as Grid Side Converter (GSC) in the back-to-back PWM driven scheme shown in Fig.6.1, enables DFIG to work in both super and sub synchronous modes. In super-sync, both rotor and stator windings deliver power to network, while in sub-sync mode, rotor intakes and stator delivers power from/to network [7, 8]. The main goal of the grid side control is to keep the DC-link voltage on the capacitor C inside a prescribed range by exchanging just undistorted active power with the line grid, regardless the magnitude and direction of the rotor power [7]. Using the SVO framework, two independent control loops for active (u-axis) and reactive powers (v-axis) flowing between RSC and GSC can be obtained.

[6] E.g. combining the equations to eliminate the square terms in one of the two variables, solving for it, and replacing the roots in one of the two original equation.

The equation describing the dynamic behavior of the DC-link is expressed as:

$$C\frac{dV_{dc}}{dt} = i_{os} - i_{or} \tag{6.16}$$

where i_{os} and i_{or} are the DC-link currents of the GSC and RSC, respectively (see Fig. 6.1). Ignoring the power electronic losses, by some basic equations, it can be shown that i_{os} is proportional to the u-axis current of GSC notated as i_g in the Fig. 6.1, and i_{or} is related to the reactive power of GSC. Again by some simple equations, it is shown that the DC-link voltage is proportional to the u-axis of i_g. In this chapter, a standard regular asymmetric-sampling, current-regulated PWM converter is used with the parameters reported in Tab. A.5 in the Appendix. For sake of brevity, the control details i.e. the standard inner/outer current loops and the corresponding PI regulators as well as the cascade scheme of the active power loop, widely discussed in literature, is not repeated here. Hence, the interested readers are referred to [32] and [7].

6.3 Simulation Results

To validate the proposed strategy, a $0.5MW$ DFIG-based WT system has been considered. Mechanical model parameters are reported in Tab. A.3, while the DFIG coefficients are reported in Tab. A.1. A PWM-driven back-to-back switching converter, providing GSC and RSC functionalities has been emulated as well, with parameters of Tab. A.5. For RSC, a discrete time version of controller (6.7), with saturated feedback terms v_u, v_v designed according to the LMI-based procedure outlined in 6.2.2, has been implemented, with sampling time equal to the PWM period. The following parameters have been considered to numerically solve problem (6.9): $v_{jmax} = u_{2jmax}/2,\ j = u, v,\ \omega_g(t) \in [0.7\omega_{nom}, 1.3\omega_{nom}]$, with $\omega_{nom} = 2\pi 50 rad/s$ representing the synchronous speed of the machine. Initial conditions for $\tilde{x}_a$ have been assumed to belong to a unit ellipsoid defined by $R = diag(\tilde{z}_{2u}^{-2}, \tilde{z}_{2v}^{-2}, \tilde{i}_{2u}^{-2}, \tilde{i}_{2u}^{-2}, \tilde{\chi}_{2u}^{-2}, \tilde{\chi}_{2v}^{-2})$, where $\tilde{z}_{2u} = 0.25Wb, \tilde{z}_{2v} = 0.85Wb$, $\tilde{i}_{2u} = 100A$, $\tilde{i}_{2v} = 100A$, $\tilde{\chi}_{2u} = 10As$, $\tilde{\chi}_{2v} = 10As$ have been conservatively set according to tracking steps during the voltage sag. The resulting feedback matrix, obtained by solving (6.9) with these data is $K = \begin{bmatrix} 116.5 & -112.8 & 0.491 & -0.001 & 1.67 & 0.0005 \\ 191.4 & 49.14 & -0.008 & 0.679 & -0.00016 & 1.57 \end{bmatrix}$. While for the GSC, standard decoupled $d-q$ control loops have been applied [7]. Similarly, a discrete version of the observer in [52] has been implemented to get information about U, $\dot{U}$. A symmetric three-phase short-circuit fault at the PCC (as shown in Fig. 6.1) causing a 100% stator voltage drop lasting for $150ms$, has been emulated, while system operates in the steady-state condition corresponding to nominal $10m/s$ and high $13m/s$ wind speed (the latter requiring pitching). In nominal

condition, the reference torque corresponding to the maximum power point defined in Section 6.2.1, or the generator rated value in case of high wind speed, is considered, while null capacitive current is set. When the voltage sag is detected (via the line observer), the references are changed as follows: T_g^* is reduced according to the dip depth, while i_{1v}^* is increased to comply with the grid codes requirements asking to keep it above 90% of the rated value to sustain the grid voltage [16], [84]. Before showing the behavior of the system scenarios, we compare, under the aforementioned dip, the proposed mapping solution, with a steady-state mapping approach, which assumes constant rotor currents [7]. Results are portrayed in Fig. 6.3 for the steady-state simplified mapping, and 6.4 for the proposed mapping. The torque and reactive current signals constructed by means of the mapping solutions are denoted with the accent $\hat{}$. By Fig. 6.3, it is clear how ignoring the first-order derivatives of the rotor currents in the zero dynamics calculations, results in a large u-axis stator flux trajectory ($\hat{z}_{2u}^*$), beyond the machine physical limits (see Fig. 6.3 (g)). As a consequence, large and inconsistent translated reference torque $\hat{T}_g^*$ is obtained (see Fig. 6.3 (b)). Hence, the steady-state mapping is not suited for dealing with harsh line faults. Instead, as confirmed by plots in Fig.6.4, references computed with the mapping solution presented in 6.2.2, accurately track the desired torque and capacitive stator current. As can be seen in Fig.6.4 (e), in contrast to the steady-state mapping, $\hat{z}_{2u}^*$ is reasonably inside the machine's physical constraints and the corresponding torque reference $\hat{T}_g^*$ computed through the mapped signals (see Fig.6.4 (a)), matches perfectly the desired torque reference T_g^* (see Fig.6.3 (a)). Therefore, the importance of the proposed improved mapping solution is underscored. Thus, in the following simulations, the proposed mapping is used to evaluate the overall system response to the voltage dip. Fig.6.5 illustrates results for the system operating with $10m/s$ wind speed, while facing the above-introduced grid fault. The oscillations of all the state variables are generally well below the system limits (provided in Tab. A.1), as highlighted in Figs. 6.5 (a)-(f)). Fleeting spikes arise in the rotor current u-component (due to the slight delay in dip detection via the observer), still they are inside the peak bound for RSC electronics[8]. Moreover, they quickly vanish to the desired references, as well as the other state variables. Note that the feedback action causes saturation of the control inputs multiple times during the dip (Fig. 6.5 (g)), however, since saturation is explicitly considered in designing the state feedback part, a graceful behavior of the system is maintained [9]. Accurate tracking of

[7] In this case, coefficients K_{4u}, K_{5u}, K_{4v}, K_{5v} in (6.5) are set to zero, and rotor currents are computed solving a standard second-order quadratic equation.

[8] Usually two times the rotor current nominal value.

[9] It is worth noting that, due to some conservatism in the feedback part saturation bounds (half of the control effort is constantly preserved for the feedforward terms), the available rotor voltage range is not fully exploited.

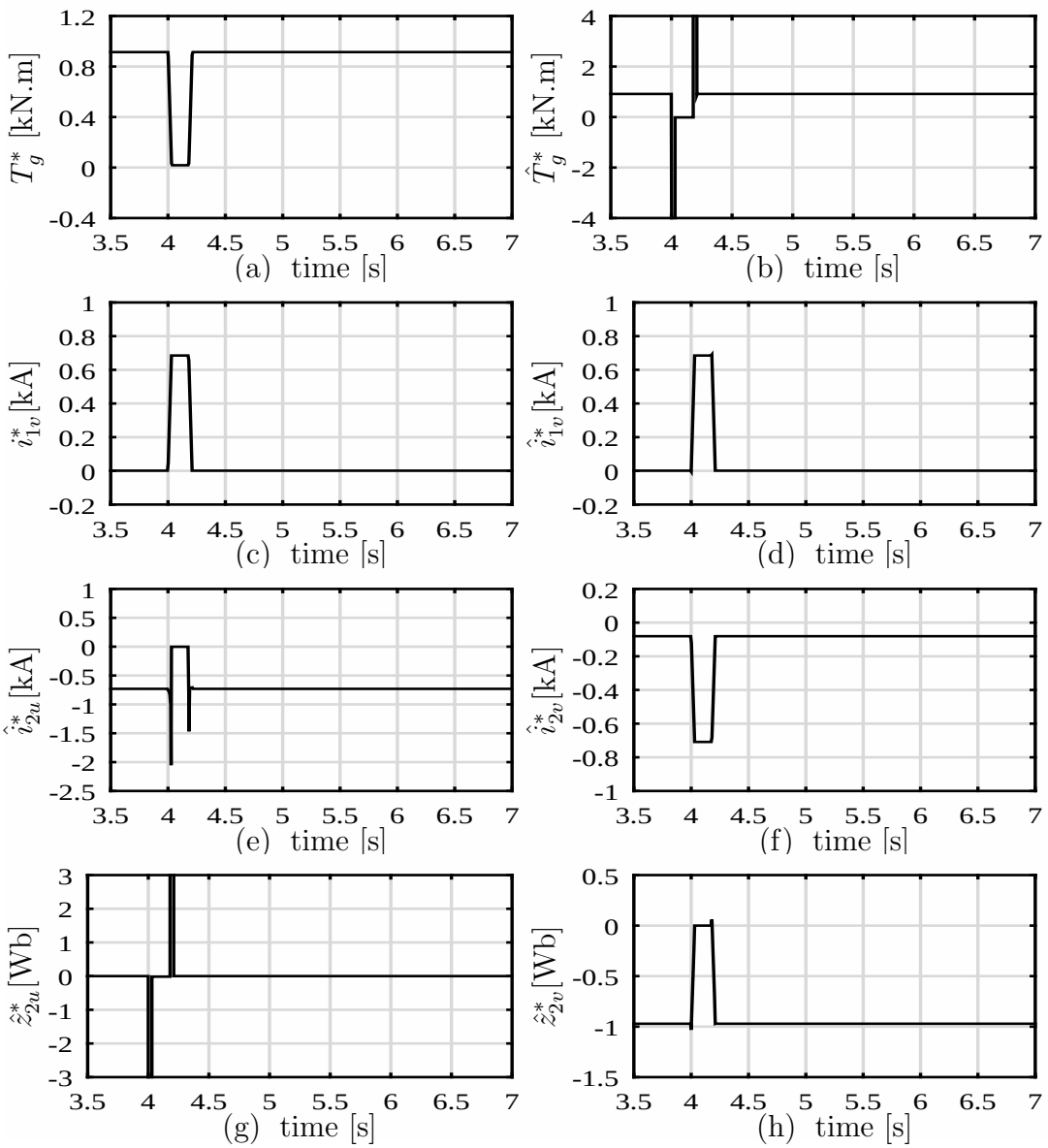

Figure 6.3: Translated references by simplified mapping solution for the system under 100% voltage dip lasting for $150ms$.

the electromagnetic torque and reactive current references is achieved thanks to the proposed mapping. The improved mapping also has positive effects in smoothing the system transient and the residual oscillations at the dip start, which are related to the fact that the actual dip shape does not perfectly fit the trapezoidal approximation adopted for calculating references in (6.5) and feedforward terms (6.6).
Fig. 6.5-(p) shows how also the mechanical part of the WT exhibit a smooth, non oscillatory behavior thanks to the adopted RSC control. Indeed, the turbine speed smoothly increases within the fault, (due to the torque reduction), then it converges back to the optimal pre-fault speed, avoiding excitation of the shaft resonance modes. Indeed, the frequency of residual generator torque oscillations is much higher than

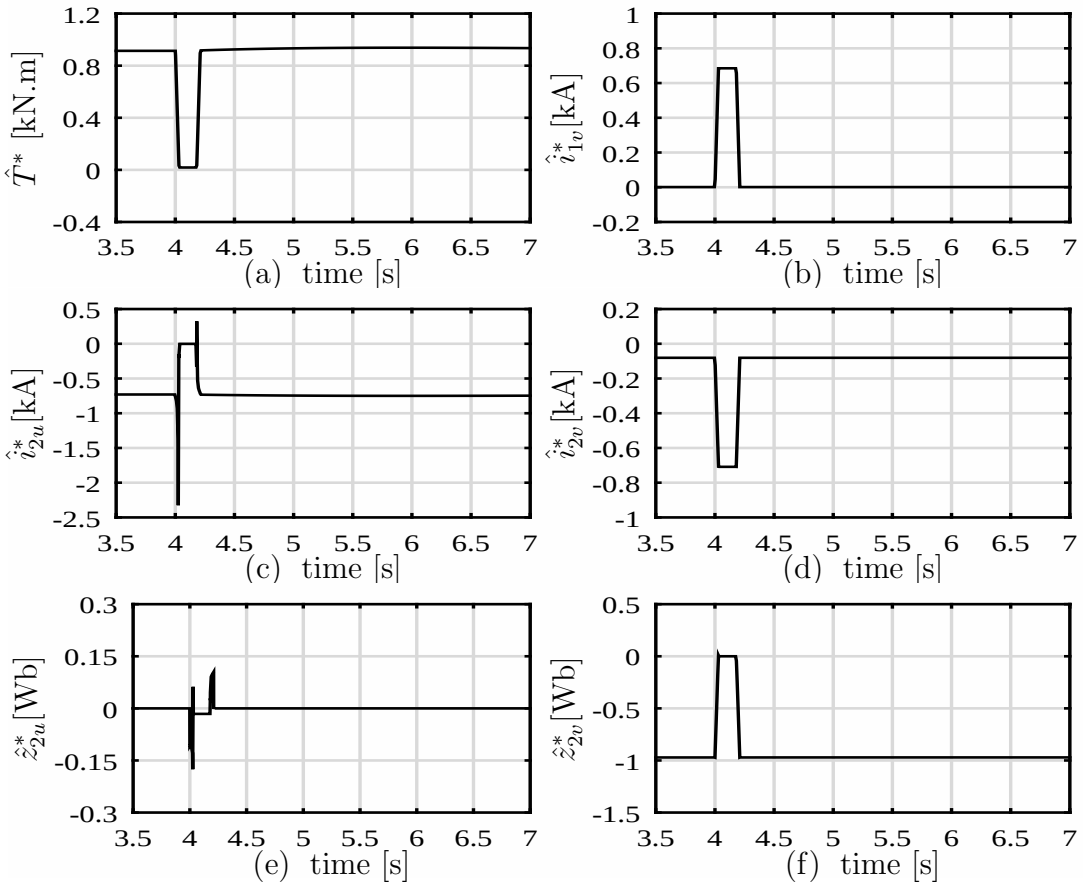

Figure 6.4: Translated references by proposed mapping solution for the system under 100% voltage dip lasting for $150ms$.

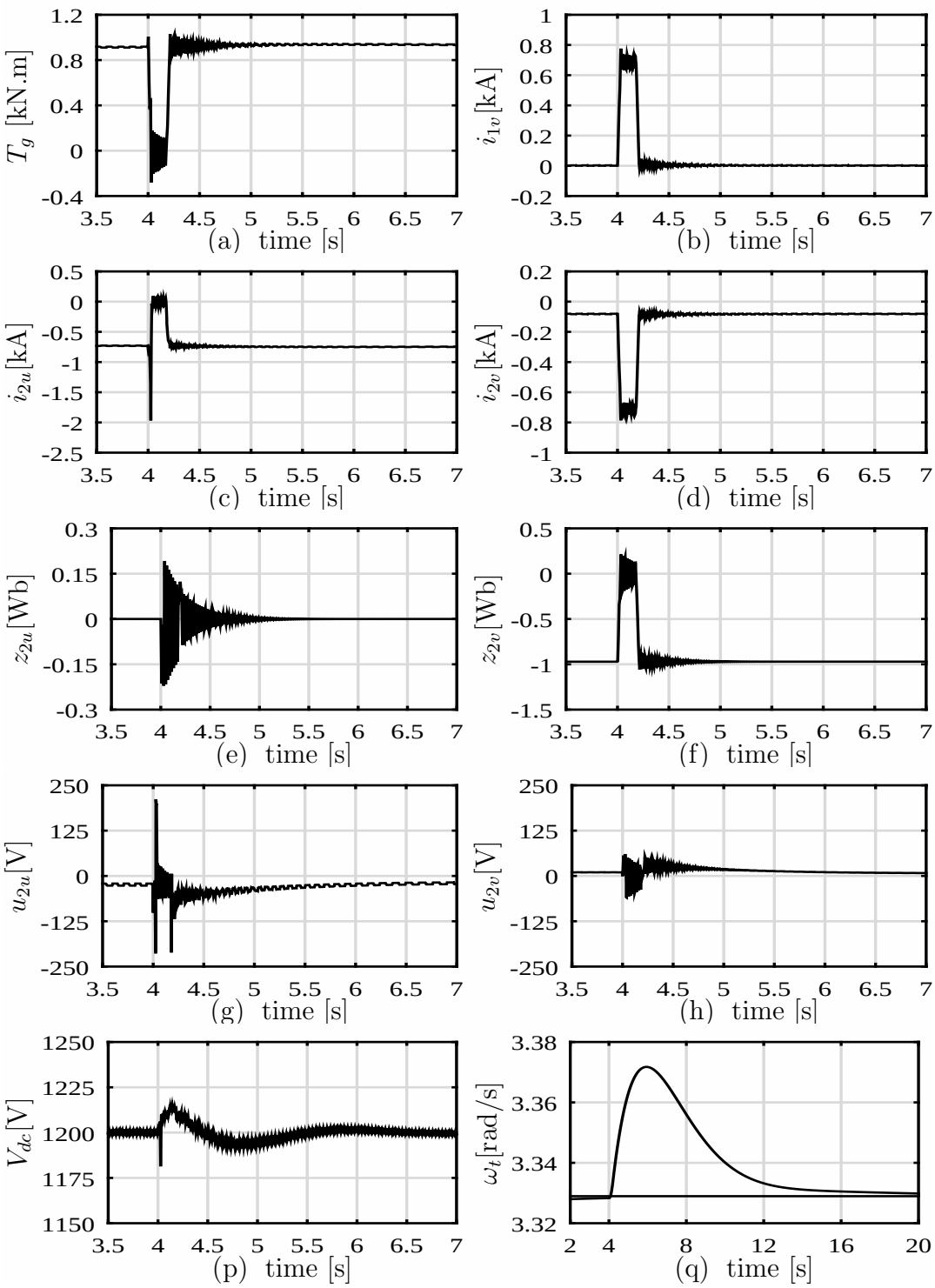

Figure 6.5: Results of the system with the proposed mapping solution and control strategy, at normal wind speed ($10m/s$) under 100% symmetrical voltage dip lasting for $150ms$.

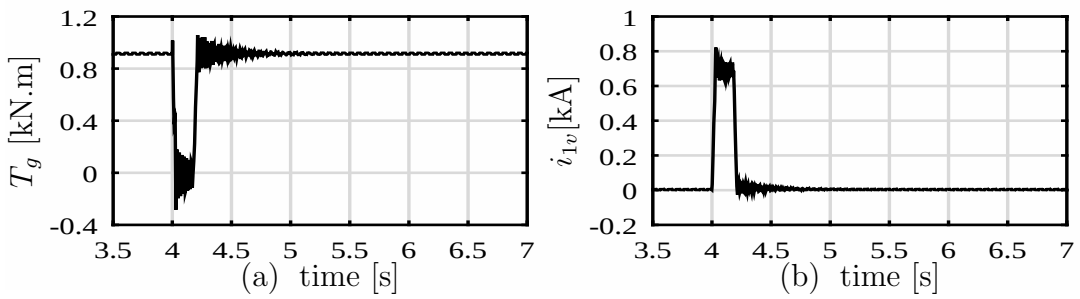

Figure 6.6: Results of the system with the proposed mapping solution and control strategy, at high wind speed ($13m/s$) under 100% symmetrical voltage dip lasting for $150ms$. (a) Generator torque. (b) Stator reactive current.

the drive-train resonant frequency. For what regards the grid side, as a result of the fast and proper response of the RSC to the dip, the standard GSC control keeps the transient oscillations of the DC-link voltage (V_{dc}) sufficiently damped, and the peak value at $1220V$ (see Fig. 6.5 (p)), inside the +15% safety margins, w.r.t. nominal operation value, typically kept when sizing the DC-bus capacitor [33, 80]. This confirms that the proposed approach can be profitably exploited for realistic applications.

Figs.6.6-6.8 depicts the results obtained under the previous test conditions, but for high wind speed ($13m/s$). Also in this case, the system response to the grid fault, ensures the LVRT capability. Similar to the previous test, the currents/fluxes oscillations are efficiently suppressed and proper torque, capacitive current tracking is achieved. At this wind speed, generator power saturation is hit, thus pitch control (a standard PI has been used) is activated (see Fig. 6.8 (d)) keeping the speed at 110% of the synchronous value[10]. During the dip, turbine speed increases as a consequence of torque reduction and the pitch actuation rate limitation, however, the generator speed is kept below the 130% synchronous speed (Fig. 6.8 (a)). Also in this scenario, after the dip clearance, the DFIG and WT speeds, turn back smoothly to the rated values (see Fig. 6.8 (a)-(b)).

6.4 Conclusion

In this chapter, LVRT with improved tracking under grid faults has been achieved for a full benchmark of a WECS including wind turbine, DFIG, and both rotor and grid side power electronic converters. The crucial methodological elements to obtain these performance are an advanced RSC control strategy, minimizing oscillations throughout the voltage dip, and a not trivial mapping relation between the

[10]For energy efficiency, to keep power bounded to generator nominal value, a little overspeed is allowed during pitching, so that the generator torque can be reduced [32].

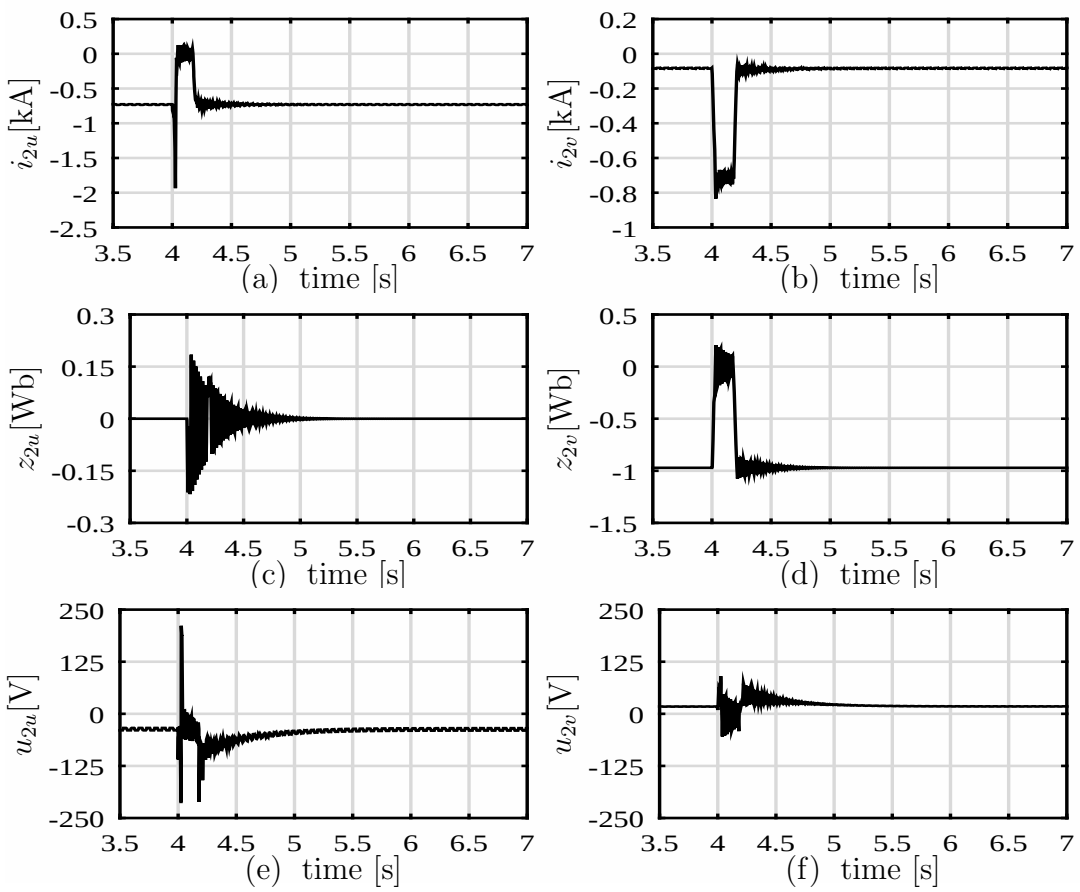

Figure 6.7: Results of the system with the proposed mapping solution and control strategy, at high wind speed ($13m/s$) under 100% symmetrical voltage dip lasting for $150ms$. (a)-(b) Rotor currents. (c)-(d) Zero dynamics (stator fluxes). (e)-(f) Rotor command voltages.

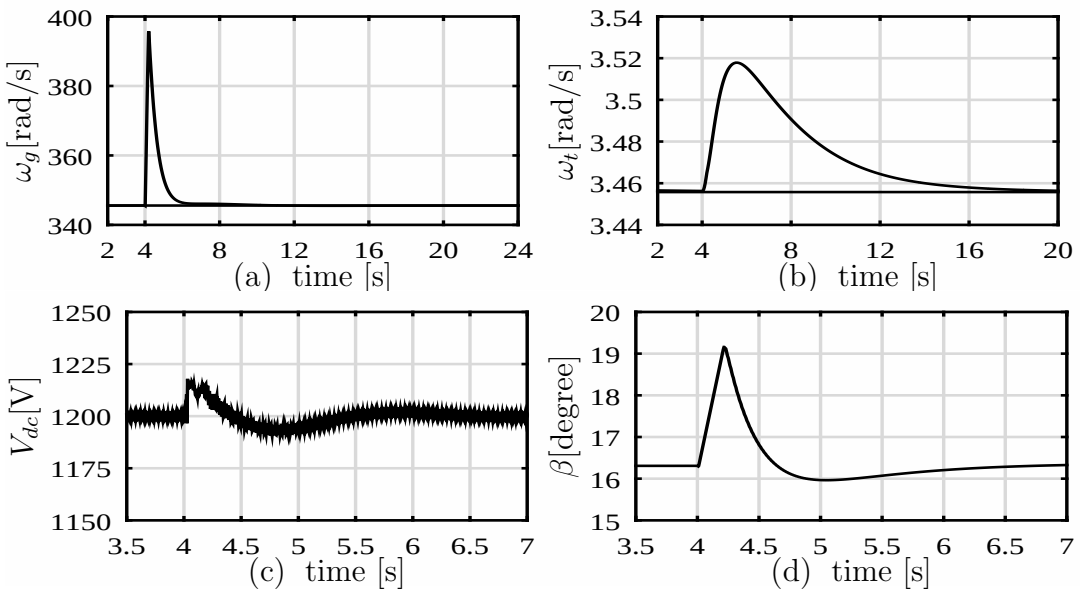

Figure 6.8: Results of the system with the proposed mapping solution and control strategy, at high wind speed ($13m/s$) under 100% symmetrical voltage dip lasting for $150ms$. (a) Generator angular speed. (b) Turbine angular speed. (c) DC-link voltage. (d) Pitch angle.

DFIG-based WT standard output variables (generator torque and capacitive stator currents during faults) and the rotor currents which are directly steered by the RSC. Validation via realistic numerical tests show promising results, confirming that the strategy can handle harsh grid faults without the intervention of additional protection hardware, thus reducing system cost and fully guaranteeing LVRT features as specified in recent Grid Codes. Despite the methodological sophistication, the overall control algorithm and mapping strategy are easy-to-implement on embedded computational platforms, as no heavy computation (e.g. optimization, iterative algorithms) is required on-line.

Chapter 7

Conclusions

This thesis focused on Low Voltage Ride Through capability of DFIG-based Wind Turbine system. In this way, a precise reliable modeling was firstly taken into account. Starting from the three-phase *abc* model of DFIG, and briefly describing it's two-axes stationary model, the synchronously-rotating Stator Voltage Oriented reference frame was finally selected for DFIG modeling elaboration, while the standard two-mass model for WT was considered. In the next pace, the most frequent power system voltage dips were introduced and classified into two main balanced/symmetric and unbalance/asymmetric sections. Then their consequent drawbacks on DFIG WT system and the classic remedy as crowbar protection was described. In the following, the necessity of adopting advanced control strategies to provide the requirements asked by modern national grid codes in order to substantiate the LVRT capability, was outlined.

After recognizing the goal, in the next chapters, control solutions suitably planned for the corresponding threats were discussed. Two conventional balanced three-phase and unbalanced single-phase to ground voltage dips were considered. Studying the DFIG's internal dynamics is a key solution for control design in this thesis. Assuming rotor currents as the output variables to be controlled, the Brunovsky form of the system dynamics was utilized, in order to clearly analyze the zero dynamics, driven by the line voltage and the rotor current references. In the light of analytical solutions for the zero dynamics ODEs based on by part integration and Sylvester equations, smart selection of initial internal states, made the way of having oscillation-free response and consequently smooth enough reference trajectory design for internal dynamics. This trajectory was the base of feedforward action plan in a closed loop control scheme whose state feedback part was designed according to saturated control techniques to further limit the unpleasant oscillations related to the poorly-damped oscillatory natural dynamics. To do this, an LMI-constrained convex optimization problem was defined to minimize the oscillations under voltage

dips.
After ensuring the graceful performance of DFIG under both severe balanced and unbalanced voltage sags proved by realistic simulation tests, the mechanical vibration of the WT was under study. It was shown that the increased generator speed due to the usual torque decline strategy under the voltage dip, needs to be smoothly returned to it's pre-fault steady-state condition by smart control strategies, otherwise leads to generator torque limit violation and undamped mechanical oscillations in the drive train. An offline optimization problem solved for different boundary conditions after the dip clearance and a low-size lookup table and interpolation were used on-line to get the smooth minimum-time trajectory corresponding to general post fault scenarios. This control strategy was also suitable enough to be easily joined as an add-on into the conventional High Pass Filter controller.
The last chapter was dedicated to install a full benchmark of the DFIG WT system including both RSC and GSC controllers, and PWM-driven back-to-back switching converters. Meanwhile, a precise mapping system converting the DFIG's conventional references of torque and stator-side reactive current into the corresponding reference rotor currents was elaborated and analytically solved. The simulation results proved the effectiveness of the mapping system in accurate reference tracking achievement.
From all above-mentioned parts, it can be briefly concluded that the main contribution of this thesis is full LVRT capability achievement for DFIG WT system relying on pure control solutions and avoid imposing any additional hardware to the system. This aspect makes our solution suitable enough for equipping the currently installed systems with LVRT capability only by adopting some add-on control parts.
In the future, connecting the DFIG WT system into the power network through compensated transmission lines will accomplish its comprehensive study. As regards the compensation level, the consequent Sub-Synchronous Control Interaction (SSSI) should be also taken into account in control design procedure. In the corresponding literature, eigenvalue analysis based on linearized system has usually been exploited in order to obtain the participation factor of each state variable for sub-synchronous unstable modes and the sensitivity of system to all the proportional and integral parameters of RSC and GSC controllers[85].

Appendix A

System Parameters

The tables below give the parameters of the studied system:

Table A.1: DFIG parameters reported to the stator-side, tested under balanced voltage dips.

DFIG rated power $[MW]$	0.5
DFIG rated torque T_g $[Nm]$	1000
DFIG rated RMS voltage [V]	380
DFIG rated RMS current [A]	760
RSC rated RMS voltage [V]	265
RSC rated RMS current [A]	780
Stator resistance R_1 [Ω]	0.0073
Stator inductance L_1 [H]	0.0126
Rotor resistance R_2 [Ω]	0.0073
Rotor inductance L_2 [H]	0.01255
Mutual inductance L_m [H]	0.01218
Number of pole pairs n_p	2
DFIG inertia $J_g = 2H_g$ $[kgm^2]$	4.5

Table A.2: DFIG parameters reported to the stator-side, tested under unbalanced voltage dips.

DFIG nominal power $[MVA]$	1.67
System frequency $[Hz]$	50
DFIG rated stator voltage [V]	690
DFIG rated stator current [A]	1105
DFIG rated rotor current [A]	476
Number of pole pairs n	2
Stator/Rotor turn ratio	1 : 3
Stator resistance R_1 $[p.u.]$	0.007
Stator inductance L_1 [p.u.]	3.071
Rotor resistance R_2 $[p.u.]$	0.009
Rotor inductance L_2 $[p.u.]$	3.056
Mutual inductance L_m $[p.u.]$	2.9
Rotational inertia constant H [s]	4.5

Table A.3: Wind turbine parameters.

Turbine rated power $[MW]$	0.5
Generator rated torque T_{gnom} $[Nm]$	1000
Turbine inertia $J_t = 2H_t$ $[kgm^2]$	2.70×10^5
Generator inertia J_g $[kgm^2]$	4.5
Shaft stiffness coefficient K_s $[Nm/rad]$	13700
Shaft damping coefficient D_s $[Nm/rad/s]$	275
Gearbox coefficient n	100
Blades radius R_w $[m]$	19
Air density ρ $[kg/m^3]$	1.225

Table A.4: Zero dynamics trajectories' coefficients.

$K_{1u} = \frac{\alpha_1^2 L_m}{M}$	$K_{2u} = \frac{\alpha_1 \omega_0 L_m}{M}$	$K_{3u} = -\frac{\omega_0}{M}$
$K_{4u} = -\frac{N \alpha_1 L_m}{M^2}$	$K_{5u} = -\frac{2\alpha_1^2 \omega_0 L_m}{M^2}$	$K_{6u} = -\frac{N}{M^2}$
$K_{1v} = -\frac{\alpha_1 \omega_0 L_m}{M}$	$K_{2v} = \frac{\alpha_1^2 L_m}{M}$	$K_{3v} = -\frac{\omega_0}{M}$
$K_{4v} = \frac{2\alpha_1^2 \omega_0 L_m}{M^2}$	$K_{5v} = -\frac{N \alpha_1 L_m}{M^2}$	$K_{6v} = \frac{2\alpha_1 \omega_0}{M^2}$
$M = \alpha_1^2 + \omega_0^2$	$N = \alpha_1^2 - \omega_0^2$	

Table A.5: Converters' parameters.

DC-link capacitor C $[F]$	0.06
DC-link rated voltage V_{dc} $[V]$	1200
Resistance of the grid side inductor R_g $[\Omega]$	0.866×10^{-3}
Inductance of the grid side inductor L_g $[H]$	0.0866
PWM switching frequency $[Hz]$	2.5×10^3

Bibliography

[1] I. R. E. A. (IRENA), "Renewable capacity statistics 2016," tech. rep., IRENA, 2016.

[2] V. Yaramasu, B. Wu, P. C. Sen, and S. Kouro, "High power wind energy conversion systems: State-of-the-art and emerging technologies," *Proceedings of IEEE*, vol. 103(5), 2015.

[3] M. Edrah, K. L. Lo, and O. Anaya-Lara, "Impacts of high penetration of dfig wind turbines on rotor angle stability of power systems," *IEEE Trans. Sustainable Energy*, vol. 6(3), pp. 759–766, 2015.

[4] A. Sureda, A. Munoz, R. Pena, and R. Cardenas, "Control of a brushless doubly-fed induction generator via a matrix converter," *IEEE Power Electronics and Applications (EPE 2011)*, 2011.

[5] R. Zhu, Z. Chen, and X. Wu, "Dynamic performance of doubly-fed induction generator stator flux during consecutive grid voltage variations," *IET Renew. Power Gener.*, vol. 9(7), pp. 720–728, 2015.

[6] W. Leonhard, *Control of electrical drives. (3rd ed.)*. Springer, Berlin, 2001.

[7] R. Pena, J. C. Clare, , and G. M. Asher, "Doubly fed induction generator using back-to-back pwm converters and its applications to variable speed wind-energy generation," *Inst. Elec. Eng. Proc. Electric Power Applications*, vol. 143(3), pp. 231–241, 1996.

[8] M. V. Kazemi, A. S. Yazdankhah, and H. Kojabadi, "Direct power control of dfig based on discrete space vector modulation," *Renewable Energy*, vol. 35, pp. 1033–1042, 2010.

[9] G. Brando, L. Cozza, and C. del Pizzo, "Optimized control of active front-ends to improve efficiency and power quality in systems with closed-loop controlled electrical drives," in *Energy efficiency in motor driven systems*, pp. 508–514, Springer-Verlag, 2003.

[10] D. W. Novotny and T. A. Lipo, *Vector control and dynamics of AC drives,*. Oxford University Press, 1996.

[11] S. Peresada, A. Tilli, and A. Tonielli, "Indirect stator flux-oriented output feedback control of a doubly fed induction machine," *IEEE Trans. Control System Tech.*, vol. 11(6), pp. 875–888, 2003.

[12] B. Hopfensperger, D. J. Atkinson, and R. A. Lakin, "Stator-flux-oriented control of a doubly-fed induction machine with and without position encoder," *Inst. Elec. Eng. Proc. Electric Power Applications*, vol. 147(4), pp. 241–250, 2000.

[13] E. Bogalecka and Z. Kzreminski, "Control system of a doubly fed induction machine supplied by current controlled voltage source inverter," *Proc. of the IEEE Conf. on Electr. Machines and Drives*, pp. 168–172, 1996.

[14] G. Rigatos, P. Siano, N. Zervos, and C. Cecati, "Control and disturbances compensation for doubly fed induction generators using the derivative-free nonlinear kalman filter," *IEEE Trans. Power Electron.*, vol. 30(10), pp. 5532–5547, 2015.

[15] G. FGW, "Certification of the electrical characteristics of power generating units and farms in the medium-, high- and highest-voltage grids," tech. rep., 2013.

[16] U. FERC, "Interconnection for wind energy," tech. rep., Docket No. RM05-4-001, Order No. 661-A, 2005.

[17] E. N. Gmbh, "Grid code, high and extra high voltages," tech. rep., Docket No. RM05-4-001, Order No. 661-A, 2006.

[18] F. TR3, "Certification of the electrical characteristics of power generating units and farms in the medium-, high- and highest-voltage grids," tech. rep., Revision 6, 2013.

[19] ENTSO-E, "Network code requirements for grid connection applicable to all generators," tech. rep., 2012.

[20] J. Lopez, E. Gubia, P. Sanchis, X. Roboam, and L. Marroyo, "Wind turbines based on doubly fed induction generator under asymmetrical voltage dips," *IEEE Ind. Trans. Energy. Convers.*, vol. 23(1), pp. 321–331, 2008.

[21] H. Geng, C. Liu, and G. Yang, "Lvrt capability of dfig-based wecs under asymmetrical grid fault condition," *IEEE Trans. Ind. Electron.*, vol. 60(6), pp. 2495–2509, 2013.

[22] P. Baiju and T. Rajeev, "Low voltage ride through in dfig based wind turbines: A review," *IEEE Inter. Conf. Ctrl. Communication and Computing India (ICCC)*, 2015.

[23] D. Xiang, L. Ran, P. J. Tavner, and S. Yang, "Control of a doubly-fed induction generator in a wind turbine during grid fault ride-through," *IEEE Trans. Energy Convers.*, vol. 21(3), pp. 652–662, 2006.

[24] S. Hu, Y. Kang, and X. Zhou, "An improved low-voltage ride-through control strategy of doubly fed induction generator during grid faults," *IEEE Trans. Pow. Electron.*, vol. 26(12), pp. 3653–3665, 2011.

[25] J. D. Costa, H. Pinheiro, T. Degner, and G. Arnold, "Robust controller for dfigs of grid-connected wind turbines," *IEEE Trans. Ind. Electron.*, vol. 58(9), pp. 4023–4038, 2011.

[26] T. D. Nguyen and G. Fujita, "Nonlinear control of dfig under symmetrical voltage dips with demagnetizing current solution," *IEEE Proc. of Power Sys. Technology Int. Conf.*, pp. 1–5, 2012.

[27] F. Lima, A. Luna, P. Rodriguez, E. Watanabe, and F. Blaabjerg, "Rotor voltage dynamics in the doubly fed induction generator during grid faults," *IEEE Trans. Power Electronics*, vol. 25(1), pp. 118–130, 2010.

[28] S. Xiao, G. Yang, H. Zhou, and H. Geng, "An lvrt control strategy based on flux linkage tracking for dfig-based wecs," *IEEE Trans. Ind. Electron.*, vol. 60(7), pp. 2820–2832, 2013.

[29] M. Rahimi and M. Parniani, "Transient performance improvement of wind turbines with doubly fed induction generators using nonlinear control strategy," *IEEE Trans. Energy Convers.*, vol. 25(2), pp. 514–525, 2010.

[30] T. K. A. Brekken and N. Mohan, "Control of a doubly fed induction wind generator under unbalanced grid voltage conditions," *IEEE Trans. Energy Convers.*, vol. 22(1), pp. 129–135, 2007.

[31] J. Liang, W. Qiao, and R. G. Harley, "Feed-forward transient current control for low-voltage ride-through enhancement of dfig wind turbines," *IEEE Trans. Energy Convers.*, vol. 25(3), pp. 836–843, 2010.

[32] L. Yang, Z. Xu, J. Østergaard, Z. Y. Dong, and K. P.Wong, "Advanced control strategy of dfig wind turbines for power system fault ride through," *IEEE Trans. Power Syst.*, vol. 27(2), pp. 713–722, 2012.

[33] D. Xie, Z. Xu, L. Yang, J. Østergaard, Y. Xue, and K. P.Wong, "A comprehensive lvrt control strategy for dfig wind turbines with enhanced reactive power support," *IEEE Trans. Power Syst.*, vol. 28(3), pp. 3302–3310, 2013.

[34] W. Guo, L. Xiao, S. Dai, Y. Li, X. Xu, W. Zhou, and L. Li, "Lvrt capability enhancement of dfig with switch-type fault current limiter," *IEEE Trans. Ind. Electron.*, vol. 62(1), pp. 332–342, 2015.

[35] Y. Shen, D. Ke, W. Qiao, Y. Sun, D. S. Kirschen, and C. Wei, "Transient reconfiguration and coordinated control for power converters to enhance the lvrt of a dfig wind turbine with an energy storage device," *IEEE Trans. Energy Convers.*, vol. 30(4), pp. 1679–1690, 2015.

[36] Q. Huang, X. Zou, D. Zhu, and Y. Kang, "Scaled current tracking control for doubly fed induction generator to ride-through serious grid faults," *IEEE Trans. Power Elect.*, vol. 31(3), pp. 2150–2166, 2016.

[37] A. Wang, W. Xi, and Y. Alsmadi, "Performance comparison of lvrt techniques for dfig wind turbine under asymmetrical voltage sags," *IEEE proc. of PEDS*, pp. 254–258, 2015.

[38] M. Rahimi and M. Parniani, "Low voltage ride-through capability improvement of dfig-based wind turbines under unbalanced voltage dips," *Electrical Power and Energy Systems*, vol. 60, pp. 82–95, 2014.

[39] P. Flanery and G. Venkataramanan, "Unbalanced voltage sag ride-through of a doubly fed induction generator wind turbine with series grid side converter," *IEEE Trans. Ind. Appl.*, vol. 45, pp. 1879–1887, 2009.

[40] A. Isidori, *Nonlinear control systems*. Springer, Hiedelberg, 1999.

[41] S. Peresada, A. Tilli, and A. Tonielli, "Power control of a doubly fed induction machine via output feedback," *Elsevier Trans. Control Engineering Practice*, vol. 12, pp. 41–57, 2004.

[42] S. Muyeen, M. Ali, R. Takahashi, T. Murata, J. Tamura, Y. Tomaki, A. Sakahara, and E. Sasano, "Comparative study on transient stability analysis of wind turbine generator system using different drive train models," *IET Renew. Power Gener.*, vol. 1(2), pp. 131–141, 2007.

[43] F. Bianchi, R. Mantz, and C. Christiansen, "Gain scheduling control of variable-speed wind energy conversion systems using quasi-lpv models," *Control Engineering Practice*, vol. 13(2), pp. 247–255, 2005.

[44] B. Boukhezzar and H. Siguerdidjane, "Nonlinear control of a variable-speed wind turbine using a two-mass model," *IEEE Trans. Energy Convers.*, vol. 26(1), pp. 149–162, 2011.

[45] A. Tilli, "Controllo non lineare di macchine ad induzione," *Ph.D. Thesis (in Italian), DEIS, University of Bologna*, December 1999.

[46] P. Novak, T. Ekelund, I. Jovik, and B. Schmidtbauer, "Modeling and control of variable-speed wind-turbine drive-system dynamics," *IEEE Contr. Syst.*, vol. 15(4), pp. 28–38, 1995.

[47] F. D. Bianchi, H. D. Battista, and R. J. Mantz, *Wind turbine control systems: principles, modelling and gain scheduling design.* Springer Science & Business Media, 2006.

[48] T. Ackermann, *Wind power in power systems.* Wiley & Sons, 2005.

[49] C. Conficoni, A. Hashemi, and A. Tilli, "Zero dynamics trajectory planning in output control of doubly fed induction machines," *IEEE 42nd Annual Conference of Industrial Electronics (IECON 2016)*, 2016.

[50] A. Tilli, C. Conficoni, and A. Hashemi, "State reference design and saturated control of doubly-fed induction generators under voltage dips," *International Journal of Control*, vol. 90(4), pp. 834–854, 2017.

[51] Q. Hu and D. Cheng, "The polynomial solution to the sylvester matrix equation," *Applied Math. Letters*, vol. 19, pp. 859–864, 2006.

[52] A. Tilli and C. Conficoni, "Adaptive observer for three phase line voltage under unbalanced conditions," *Proc. of NOLCOS*, pp. 1981–1986, 2010.

[53] P. Vas, *Sensorless Vector and Direct Torque Control.* Oxford, New York (USA), 1998.

[54] Z. Lin and T. Hu, *Control Systems with Actuator Saturation.* Birkhauser, Boston, MA, 2001.

[55] H. K. Khalil, *Nonlinear Systems 2nd Ed.* Prentice-Hall Inc., Upper Saddle River, NJ, USA, 1996.

[56] T. Hu, A. Teel, and L. Zaccarian, "Stability and performance for saturated systems via quadratic and nonquadratic lyapunov functions," *IEEE Trans. on Automatic Contr.*, vol. 51(11), pp. 1170–1786, 2006.

[57] T. Thibodeau, W. Tong, and T. Hu, "Set invariance and performance analysis of linear systems via truncated ellipsoids," *Automatica*, vol. 45(9), pp. 2046–2051, 2009.

[58] S. Boyd, L. E. Ghaoui, E. Feron, and V. Balakrishnan, *Linear Matrix Inequalities in System and Control Theory*. SIAM Studies in Applied Mathematics, Philadelphia, 1994.

[59] A. Tilli, C. Conficoni, and A. Hashemi, "Advanced feedforward-feedback control of doubly-fed induction generator under unbalanced voltage dip," *submitted to Elsevier Trans. Control Engineering Practice*, 2017.

[60] J. Hossain and A. Mahmud, *Renewable Energy Integration: Challenges and Solutions*. Springer Science and Business Media, 2014.

[61] ABB, "Distribution automation handbook, mv feeder earth-fault protection," , Section 8.6, 2010.

[62] M. H. J. Bollen, *Understanding Power Quality Problems: Voltage Sags and Interruptions*. IEEE Press, New York (USA), 1991.

[63] e. a. H. Nian, "Improved direct power control of a wind turbine driven doubly fed induction generator during transient grid voltage unbalance," *IEEE Trans. Energy Convers.*, vol. 26(3), pp. 976–986, 2011.

[64] C. Sankaran, "Effects of harmonics on power systems, electrical construction and maintenance," *Electrical Construction and Maintenance, http://ecmweb.com/power-quality/effects-harmonics-power-systems*, 1999.

[65] A. Tilli and C. Conficoni, "Adaptive observer for three phase voltage source under unbalanced conditions," *Proc. of IFAC Symposium on Nonlin. Ctrl. Sys.*, pp. 1981–1986, 2010.

[66] J. Svensson, M. Bongiorno, and A. Sannino, "Practical implementation of delayed signal cancellation method for phase-sequence separation," *IEEE Trans. Power del.*, vol. 22(1), pp. 18–26, 2007.

[67] GWEC, "Global wind statistics 2015," tech. rep., GWEC, 2016.

[68] B. Singh and S. Singh, "Wind power interconnection into the power system: A review of grid code requirements," *The Electricity Journal*, vol. 22(5), pp. 54–63, 2009.

[69] J. Fuentes, M. Canas, E. Gomez, A. Molina, and F. JimÃ©nez, "International review of grid connection requirements related with voltage dips for wind farms," *Proc. of Int. Conf. Renewable Energies and Power Quality*, pp. 1–6, 2007.

[70] R. Rocha, L. S. M. Filho, and M. V. Bortolus, "Optimal multivariable control for wind energy conversion system a comparison between h2 and h controllers," *Proc. of IEEE conf. on decision and control*, pp. 7906–7911, 2005.

[71] C. Sloth, T. Esbensen, M. Niss, J. Storustrup, and P. Odgaard, "A youla-koucera approach to gain-scheduling with application to wind turbine control," *Proc. of IEEE Multi-conference on systems and control*, pp. 1489–1494, 2009.

[72] C. L. Bottasso, A. Croce, and B. Savini, "Performance comparison of control schemes for variable-speed wind turbines," *Journal of physics: Conference series 75*, pp. 1–10, 2007.

[73] S. M. Muyeen, R. Takahashi, T. Murata, and J. Tamura, "A variable speed wind turbine control strategy to meet wind farm grid code requirements," *IEEE Trans. Power Syst.*, vol. 25(1), pp. 331–340, 2010.

[74] J. B. Rawlings and D. Q. Mayne, *Model Predictive Control: Theory and Design*. Nob Hill Publishing, 2013.

[75] A. Bemporad, F. Borrelli, and M. Morari, "Model predictive control based on linear programming:the explicit solution," *IEEE Trans. Autom. Control*, vol. 47(12), pp. 1974–1985, 2002.

[76] C. Conficoni, A. Hashemi, and A. Tilli, "Recovery of the voltage-dip speed increase in wind turbine by offline trajectory planning," *IEEE 42nd Annual Conference of Industrial Electronics (IECON 2016)*, 2016.

[77] S. M. Muyeen, R. Takahashi, M. Ali, T. Murata, and J. Tamura, "Transient stability augmentation of power system including wind farms by using ecs," *IEEE Trans. Power Syst.*, vol. 23(3), pp. 1179–1187, 2008.

[78] R. Zanasi, C. G. L. Bianco, and A. Tonielli, "Nonlinear filters for the generation of smooth trajectories," *Automatica*, vol. 36, pp. 439–448, 2000.

[79] K. Okedu, S. Muyeen, R. Takahashi, and J. Tamura, "Wind farms fault ride through using dfig with new protection scheme," *IEEE Trans. Sustainable Energy*, vol. 3(3), pp. 242–254, 2012.

[80] Z. Zou, X. Xiao, Y. Liu, Y. Zhang, and Y. Wang, "Integrated protection of dfig-based wind turbine with a resistive-type sfcl under symmetrical and asymmetrical faults," *IEEE Trans. Appl. Super.*, vol. 26(7), 2016.

[81] A. Hashemi, C. Conficoni, and A. Tilli, "A novel control solution for improved trajectory tracking and lvrt performance in dfig-based wind turbines," *submitted to IEEE Trans. Sustainable Energy*, 2017.

[82] B. Shen, B. Mwinyiwiwa, Y. Zhang, and B. T. Ooi, "Sensorless maximum power point tracking of wind by dfig using rotor position phase lock loop (pll)," *IEEE Trans. Power Elect.*, vol. 24(4), pp. 942–951, 2009.

[83] A. Tilli and C. Conficoni, "Speed control for medium power wind turbines: An integrated approach oriented to mppt," *Proc. of IFAC World Congress.*, pp. 1981–1986, 2011.

[84] J. Ruan, Z. Lu, Y. Qiao, and Y. Min, "Analysis on applicability problems of the aggregation-based representation of wind farms considering dfigs' lvrt behaviors," *IEEE Trans. Power Systems*, vol. 31(6), pp. 4953–4965, 2016.

[85] L. Fan, C. Zhu, Z. Miao, and M. Hu, "Modal analysis of a dfig-based wind farm interfaced with a series compensated network," *IEEE Trans. Energy Conv.*, vol. 26(4), pp. 1010–1020, 2011.